2

WRDC-TR-90-4058

Thermodynamic and Diffusivity Measurements in Potential Ultra High Temperature Composite Materials

J. D. Cawley, G. R. St. Pierre, J. D. Kalen, J. C. Amante,
K. Gourishankar, and K. S. Goto

The Ohio State University
Research Foundation
Department of Materials Science and Engineering
1314 Kinnear Road
Columbus OH 43212

August 1990

Final Report for Period October 1987 - January 1990

MATERIALS LABORATORY
WRIGHT RESEARCH AND DEVELOPMENT CENTER
AIR FORCE SYSTEMS COMMAND
WRIGHT-PATTERSON AIR FORCE BASE, OHIO 45433-6533

262360

NOTICE

This technical report has been reviewed and is approved for publication.

Allan P Katz

ALLAN P. KATZ
Project Engineer

FOR THE COMMANDER

WALTER H. REIMANN, Chief
Materials Development Branch
Metals and Ceramics Division

REPORT DOCUMENTATION PAGE

Form Approved
OMB No. 0704-0188

1. AGENCY USE ONLY *(Leave blank)*

2. REPORT DATE
August 1990

3. REPORT TYPE AND DATES COVERED
Final, 10/1/87 - 1/31/90

4. TITLE AND SUBTITLE
Thermodynamic and Diffusivity Measurements in Potential Ultra High Temperature Composite Materials

5. FUNDING NUMBERS
PE - 62102F
PR - 2420
TA - 01
WU - AF

6. AUTHOR(S)
J.D. Cawley, G.R. St. Pierre, J.D. Kalen, J.C. Amante, K. Gourishankar, and K.S. Goto

7. PERFORMING ORGANIZATION NAME(S) AND ADDRESS(ES)
The Ohio State University Research Foundation
1314 Kinnear Road
Columbus, Ohio 43212

8. PERFORMING ORGANIZATION REPORT NUMBER
RF Project 766346/720042

9. SPONSORING/MONITORING AGENCY NAME(S) AND ADDRESS(ES)
Allan P. Katz (513) 255-9824
Materials Directorate (WL/MLLM)
Wright Laboratory
Wright Patterson Air Force Base, OH 45433-6533

10. SPONSORING/MONITORING AGENCY REPORT NUMBER
WRDC-TR-90-4058

11. SUPPLEMENTARY NOTES

12a. DISTRIBUTION/AVAILABILITY STATEMENT
Approved for public release; distribution is unlimited.

12b. DISTRIBUTION CODE

13. ABSTRACT *(Maximum 200 words)*

The study of the vaporization kinetics of CaZr03 and BaZr03 have been carried out in the temperature range 1600-2000 C using a vacuum microbalance technique. Oxygen tracer diffusion coefficients in CaZr03, BaZr03 and SrZr03 have also been measured using the gas exchange technique. Tracer concentration profiles were determined using nuclear reaction analysis. Both CaZr03 and BaZr03 have a relatively high rate of evaporation at high temperatures. However, dry-pressed CaZr03 shows a smaller rate of evaporation than hot-pressed but impure BaZr03. Results of the diffusion experiments indicate that CaZr03 exhibits the largest penetration with BaZr03 showing the smallest. Apparent oxygen tracer diffusion coeficients were measured for CaZr03 and SrZr03 at 1000C. Over the temperature range of 900-1100C, the apparent oxygen tracer diffusion coefficient in BaZr03 is described by D=5.0 x 10-3 cm2/sec exp (-247 KJ/mole/RT).

14. SUBJECT TERMS
Calcium Zirconate, Barium Zirconate, Strontium Zirconate

15. NUMBER OF PAGES
105

16. PRICE CODE

17. SECURITY CLASSIFICATION OF REPORT
UNCLASSIFIED

18. SECURITY CLASSIFICATION OF THIS PAGE
UNCLASSIFIED

19. SECURITY CLASSIFICATION OF ABSTRACT
UNCLASSIFIED

20. LIMITATION OF ABSTRACT
UNLIMITED

CONTENTS

Chapter Page

ILLUSTRATIONS

LIST OF ILLUSTRATIONS (CONT)

LIST OF ILLUSTRATIONS (CONT)

LIST OF ILLUSTRATIONS (CONT)

TABLES

1. BACKGROUND

Calcium zirconate, barium zirconate and strontium zirconate have been identified as potential ultra-high temperature composite materials. These materials are proposed as candidate materials for use in advanced aeropropulsion systems where the engines operate in severe operating conditions of 1650°C to 2200°C. The advantage of such high operating temperatures includes the reduction of specific fuel consumption and thus operating costs.

In order to achieve such an objective, quite a few new materials have been proposed. But many of these new materials have been proposed only on the basis of their high melting points and their good mechanical strength. Very often the chemical stability of these materials at the ultra-high operating temperatures of 1650°C to 2200°C are neglected.

There is a paucity of thermodynamic and kinetic data in the temperature range 1650-2200°C for many of the potential materials. This is especially true in the case of mixed oxides, although the vapor pressures of pure oxides [1] as well as the relative rate of evaporation for solid solutions in systems like $CaO-ZrO_2$ [2] have been measured.

Hence the purpose of this research is to provide fundamental thermodynamic and kinetic data in the temperature range 1650-2200°C for calcium, barium and strontium zirconates. The evaluation of the kinetics of vaporization of these materials addresses such issues as the weight loss per unit area per hour ($mg/cm^2/hr$) anticipated for zirconates if they are used as the wall of the combustion compartment of jet engines operating at about 2000°C. In this manner the potential of the material to serve as a matrix or coating for high temperature composites can be evaluated.

One also has to consider the corrosive oxygen- containing environments in which these materials are expected to operate. If these materials are to act as oxygen barriers to prevent oxidation of metallic on non-oxide ceramic components, knowledge of oxygen diffusivity is important. Therefore another objective of this project is to study oxygen diffusion in the alkaline-earth zirconates.

The literature was searched for diffusion data on these zirconates but no data was found. Available data in the literature include oxygen diffusivity in alkaline-earth stabilized zirconia and in some related mixed oxides with the perovskite structure. Kingery et. al. [3] measured oxygen diffusivity in calcia-doped zirconia having a defective fluorite structure, over the temperature range of 700°C to 1100°C. Because of the high concentration of oxygen vacancies in this defective fluorite structure, diffusion in stabilized zirconia is expected to be significantly higher than in zirconates which have the perovskite structure.

The available data on oxygen diffusion in perovskites were measured over the temperature range of 800°C to 1100°C for $BaTiO_3$ [4,5] and from 1000°C to 1300°C for $SrTiO_3$ [6]. If diffusion coefficient measurements are extrapolated over the temperature range of 1650°C to 2200°C, calculated results show that oxygen diffusivity in $BaTiO_3$ $SrTiO_3$ are two and three orders of magnitude lower than in stabilized zirconia respectively. Diffusion coefficients may be determined through the introduction into the system of a tracer which is frequently an isotope with a low natural abundance. For oxygen, the isotope ^{18}O is commonly used. In a gas exchange experiment, an atmosphere of O_2 enriched with ^{18}O is brought into contact with the sample at a given temperature and annealing time. After this anneal the tracer profile in the solid is determined and compared to an expected profile based on a solution to the diffusion equation.

Nuclear Reaction Analysis (NRA) is a proven technique for determining the ^{18}O tracer concentration versus depth. This technique is composed of two methods, 1) the proton induced *non-resonant* nuclear reaction using the $^{18}O(p,\alpha)^{15}N$ reaction [7], and 2) the nuclear resonance technique employing the 1169 keV resonance of the $^{18}O(p,\gamma)^{19}F$ nuclear reaction. Both nuclear reactions are described by the compound nuclear model where an incoming projectile strikes the target nucleus, creates an excited nucleus which then decays via an alpha (gamma-ray) for the non-resonant (resonant) nuclear reaction. Both techniques have their advantages and disadvantages which will be discussed fully in their respective experimental sections.

2. EXPERIMENTAL PROCEDURE

2.1 Sample Preparation

$CaZrO_3$ powder was obtained from Alfa Products, $BaZrO_3$ from TAM and $SrZrO_3$ from Universal Energy Systems. The chemical analyses of the zirconates are shown in Table 1. X-ray diffraction analyses of the starting powders showed that $CaZrO_3$ was a single phase material containing the low temperature orthorhombic phase. $BaZrO_3$ and $SrZrO_3$ were also single-phase materials of the cubic and orthorhombic forms, respectively.

The as-received powders were hot pressed using a Vacuum Industries vacuum hot press sintering furnace. $CaZrO_3$ samples were hot pressed at three different temperatures and pressures to determine the effect of temperature and pressure on its sintering behavior. The temperature and pressure chosen for hot pressing $CaZrO_3$ was 1400°C and 20.7 MPa. These conditions were also used in hot pressing $BaZrO_3$ and $SrZrO_3$.

Hot-pressed samples of the three zirconates were characterized by density measurements and by scanning electron microscopy. In addition, further observation of the $CaZrO_3$ and $BaZrO_3$ microstructures was performed using transmission electron microscopy (TEM). Quantitative analysis of the grains and grain boundaries were done using energy dispersive spectroscopy (EDS).

Because of the significant amounts of impurities in the commercial powders

Table 1. Chemical Analyses of the Alkaline-Earth Zirconates.

Material	Supplier	Major Impurities (ppm)*
$CaZrO_3$	Alfa Products	Fe(200), Al(3000), Si(700), Ti(1000), Mg(50), Ba(10000), Hf(10000), Mn(5), K(2)
$BaZrO_3$	TAM	Fe(1000),Al(1000),Si(30000), Ti(2000), Mg(100), Ca(1000), Na(100), Sr(300), K(10)
$SrZrO_3$	Universal Energy Systems	Fe(200), Al(200), Si(500), Ti(50), Mg(3000), Ba(100), Mn(3000), Ga(1000), Na(300)

* Coors Analytical Laboratory, Golden Col., CO

(Table 1), zirconates were also prepared by solid state reaction using alkaline-earth carbonates and zirconia as starting powders. Samples prepared by this method were used in vaporization studies; however fully dense samples could not be achieved within the time frame of this project and so no diffusion anneals were performed on these materials. The powder preparation procedure for the diffusion samples is described in Appendix A.

For the vaporization experiments, calcium zirconate samples were synthesized starting from powders of $CaCO_3$ and ZrO_2 following a procedure developed by Okubo et al. for calcium, barium and strontium zirconates [8]. $CaCO_3$ grain size was large to start with (about 20 μ) and hence it was ball milled separately in acetone for 8 hours. Then equimolar proportions of $CaCO_3$ and ZrO_2 were mixed and ball milled in acetone for 17 hours. Tablets of calcium zirconate were then prepared by dry pressing the mixture at a pressure of 1 MPa and then calcining at 1400°C for 1 hour. X-ray diffraction revealed a single phase $CaZrO_3$ structure.

Dry-pressed tablets of calcium zirconate, about 9 mm in diameter and 1 mm in height were used. A couple of experiments using the hot-pressed samples of $CaZrO_3$ were also performed. The hot-pressed samples were parallelopiped in shape with one of the dimension being small compared to the other two.

A similar procedure was followed for synthesizing barium zirconate and preparing dry-pressed samples. However, these samples were very difficult to handle and additional sintering at 1450°C for three hours did not significantly improve the mechanical strength. So hot-pressed samples were used for all tests with $BaZrO_3$. The samples were heated in air at 1000°C for 24 hours in order to reoxidize samples which were hot pressed in the carbon saturated reducing environment.

Diffusion specimens were prepared from the hot-pressed samples of the three commercial powders. The hot-pressed disks which were 1.7 inch in diameter vere cut into half-inch square specimens using a diamond wafering blade. The hot-pressed samples were greyish in color due to the reducing atmosphere of the hot press. Cut specimens were oxidized in air at 1000°C for 12 hours. After oxidizing in air, the specimens were polished to a mirror finish using 6, 3, 1 and 1/4 micron diamond pastes.

2.2 Vaporization Studies

2.2.1 Experimental Set-Up

The experimental investigation of calcium and barium zirconates were carried out in a vacuum microbalance apparatus. This apparatus is illustrated schematically in Figure 1. The salient features include a vacuum system, a Cahn 2000 electrobalance and an induction coil.

The vacuum system consists of an oil diffusion pump backed by a mechanical pump and a liquid nitrogen trap and is capable of achieving a level of vacuum of about 10^{-6} torr at low temperatures. The microbalance is capable of measuring weight changes as small as 0.1 micrograms. The heating of the sample is achieved by using a Lepel high frequency induction unit.

Figure 2 shows the reaction chamber in slightly greater detail. The sample is suspended by a molybdenum wire in the center of a graphite susceptor. The sample is heated indirectly by radiation from the graphite susceptor which couples to the RF coil directly. The graphite susceptor is machined in such a way so as to enable the temperature measurements to be carried out from the bottom through a black body hole. The lower portion of the susceptor consists of a hole, 4 mm in diameter and extending 20 mm deep to a point very close to the bottom of the susceptor. The temperature measurement is carried out using a disappearing filament type optical pyrometer.

The suspension system consists of two segments of quartz wires and a final segment of molybdenum wire which is attached to the sample by making small grooves on the sample. The insulating system consists of a layer of zirconia felt, 0.1 inch thick, surrounded by an outer alumina tube, 0.125 inch thick. The whole assembly is housed

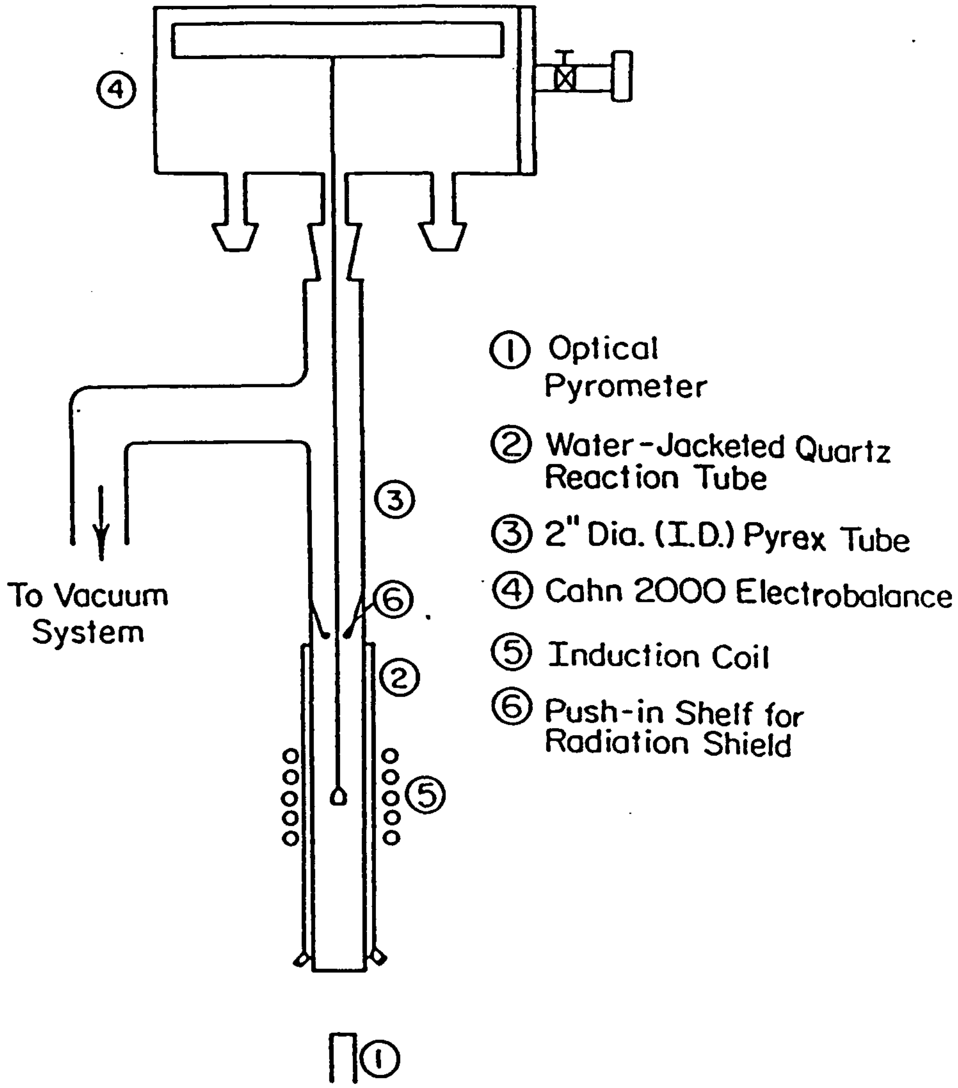

Figure 1. The microbalance experimental set-up used for the vaporization studies.

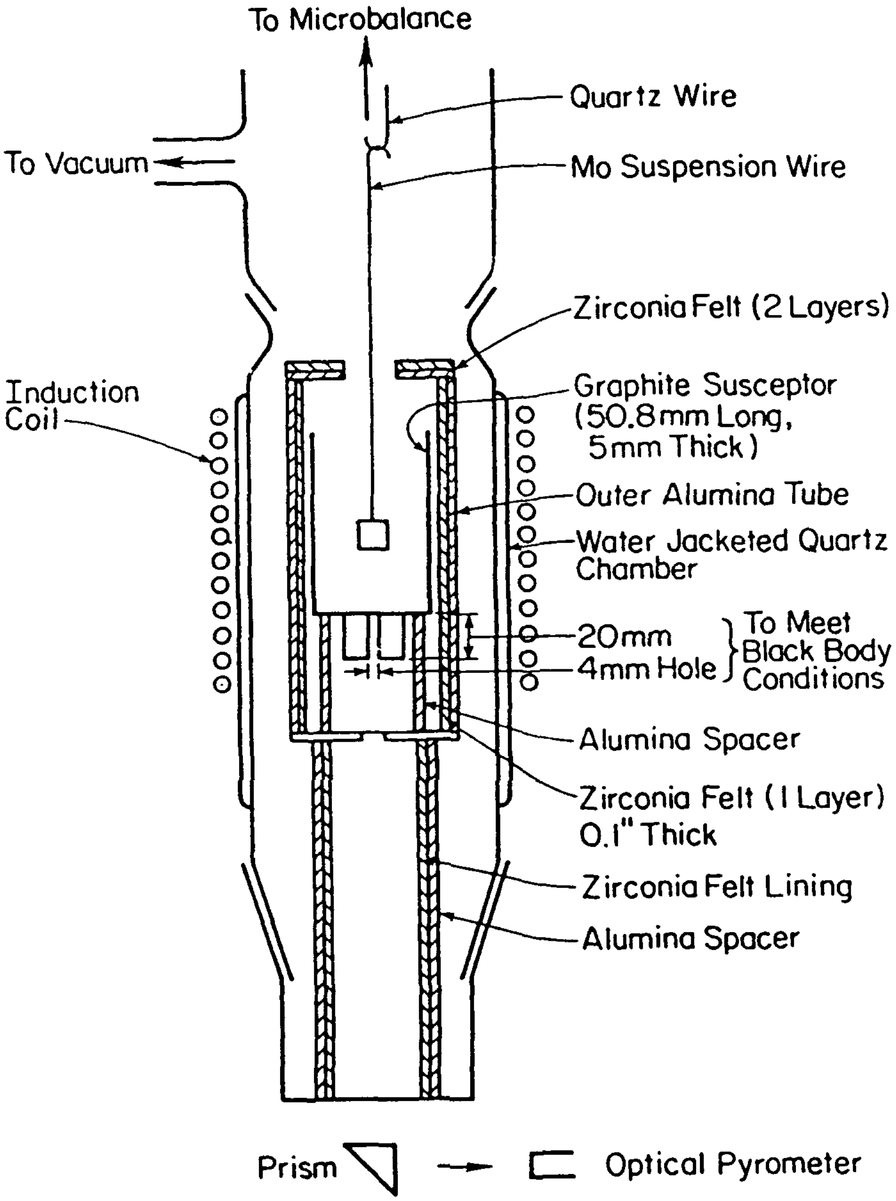

Figure 2. A schematic showing the details of the reaction chamber in the experimental set-up.

in a water jacketed quartz chamber, cooled by circulating water. The top of the hot zone is insulated by two layers of zirconia felt, each 0.1 inch thick, with a central opening for inserting the sample into the hot zone. The zirconia felt lining has proved to be an excellent heat insulator and an added advantage in that it does not couple to the RF induction coil in the kilocycle range used in these experiments.

2.2.2 Temperature Calibration

Temperature calibration has been carried out in order to obtain meaningful temperature readings. For the purposes of temperature calibration, the experimental set-up was slightly modified. The microbalance was removed and a glass stopper with an optical window was inserted to allow direct observation of samples. The melting point of elemental standards was correlated with the optical pyrometer temperature readings taken through the blackbody hole at the bottom.

Two pure elements (purity>99.0%), Fe and Ni, were used. The samples were suspended from the glass stopper into the center of the graphite susceptor. The melting point was noted by observing the metal from the top through a prism and noting the temperature reading of the pyrometer as soon as the metal melted and dropped off into the shallow graphite crucible at the bottom of the susceptor. The experiment proved to be repeatable and the results are shown in Figure 3. The graphite susceptor completely surrounds the metal sample and hence there is no direct RF coupling between the induction coil and the metal sample.

Calibration of the optical pyrometer was made in accordance with Wien's law concerning the spectral distribution of energy in the emission spectrum which yields a relationship between the true temperature and the apparent temperature [9] as follows:

$$1/T_{true} - 1/T_{app} = (\lambda/C_2)\ln(\alpha\varepsilon_\lambda)$$

where λ = wavelength of radiation, 0.653×10^{-4}cm for the optical pyrometer

C_2 = constant = 1.438 cm-deg

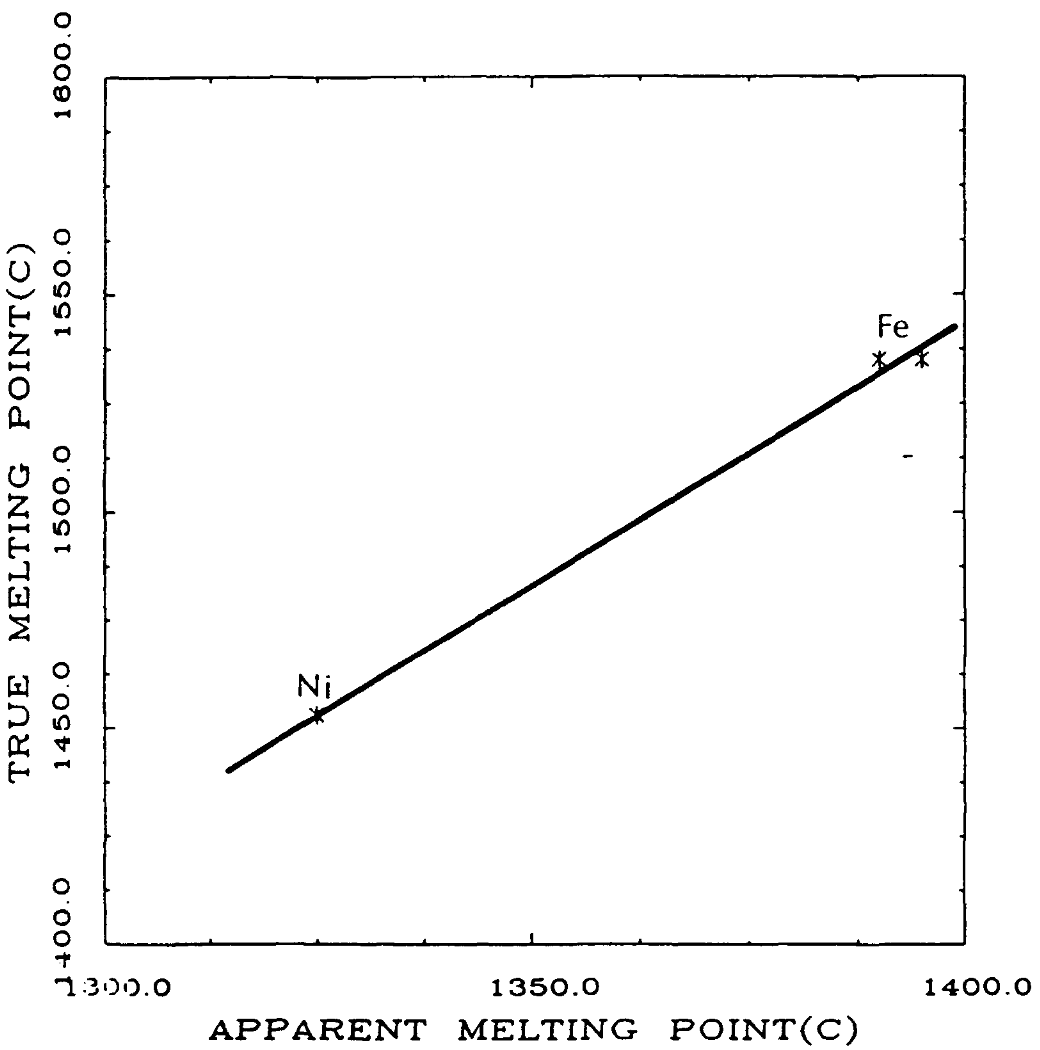

Figure 3. A plot of the true melting point vs. the apparent melting point, obtained from an optical pyrometer, for Fe and Ni.

ε_λ = emissivity of body at wavelength

α = absorption coefficient to take into account the absorption effect due to the optical path

T_{true} = true temperature in °K and

T_{app} = apparent temperature in °K.

The right hand side of the above equation is nearly constant with a value of about -4.6×10^{-5}/°K from independent measurements with Fe and Ni. Both Fe and Ni have melting points lying in the medium range of the optical pyrometer reading. But independent experiments have shown that the low range of the pyrometer (775-1225°C) always reads 25°C lower than the medium range (1075-1750°C) in the region of overlap between the two ranges while the high range of the pyrometer (1500-2850°C) always reads 50°C higher than the medium range in the region of overlap between the two ranges. The complete temperature calibration for all the three ranges of the optical pyrometer is shown in Figure 4.

2.2.3 Procedure

The samples were suspended from the microbalance and heated in vacuum. The heating rates used were rapid, as is typical of induction heating. Usually a temperature of 1800°C was achieved in about half an hours time. The weight loss experienced by the materials at a given temperature was recorded continuously by a chart recorder connected to the Cahn electrobalance. The measurements were usually carried out for about 2 hours. The measurements were carried out in the most appropriate recorder range depending on the rate at which the material was losing weight at that given temperature. The vacuum was usually maintained below 10^{-3} torr.

Calcium zirconate and barium zirconate were each tested at three different temperatures. Two experiments were carried out at each temperature to check the reproducibility of the measurements. After the vaporization experiments, the samples

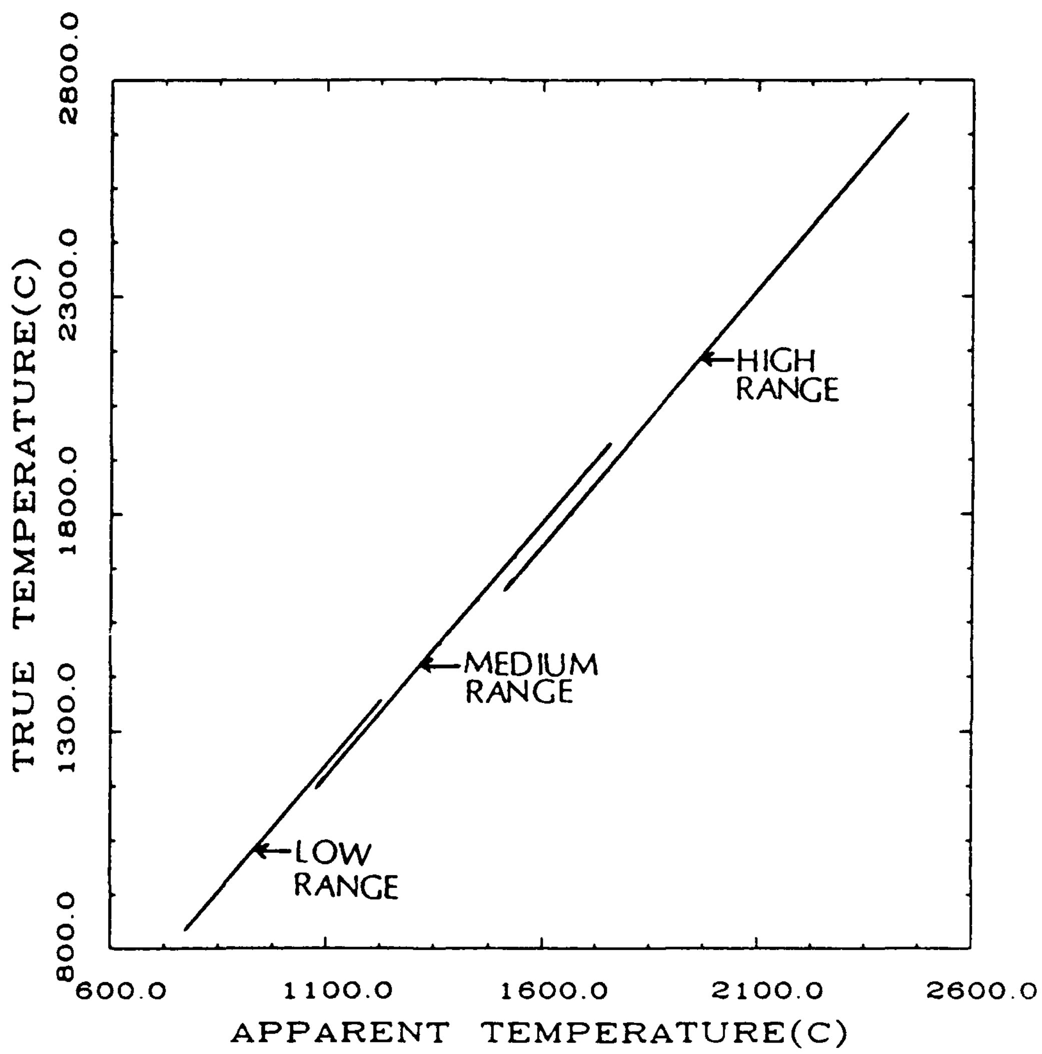

Figure 4. A temperature calibration plot for the three ranges of the optical pyrometer.

were characterized by XRD, SEM and EDS to obtain information regarding the microstructural and chemical transformations accompanying the vaporization process.

2.3 Diffusion Studies

2.3.1 Gas-Exchange Diffusion Apparatus

A schematic diagram of the gas-exchange diffusion apparatus is shown in Figure 5. The apparatus is a closed system consisting of an alumina tube which has one closed end and the other connected to pyrex glass tubing using a vacuum quick disconnect. At the end of the glass tubing is a mechanical pump which was used as a backup equipment for evacuating the system of air.

The alumina tube was placed inside a Lindberg single-zone, global-type tube furnace with a maximum temperature of 1500°C. A Lindberg controller was used to maintain the temperature within ±5°C. A platinum/platinum-10% rhodium thermocouple placed inside the alumina tube was used to measure the temperature of the samples.

Between the furnace and the mechanical pump are two Varian Vacsorb pumps one of which was used to store the ^{16}O:^{18}O gas mixture and the other to evacuate the system of air. The Varian Vacsorb pump is a sorption pump capable of pumping ultrahigh vacuum systems from atmospheric pressure to 1 x 10^{-2} Torr using synthetic zeolite [10]. This sorption pump provides clean vacuum without the oil contamination usually present when mechanical pumps are used. The gas pressure in the system was monitored using a standard barometric pressure/vacuum gauge and a thermocouple vacuum gauge.

2.3.2 Procedure

Before a diffusion anneal experiment samples were preannealed in air, using a vented tube, for 24 hours at the diffusion temperature for quilibration. The vents were then closed and the air evacuated by submerging one of the sorption pumps in liquid

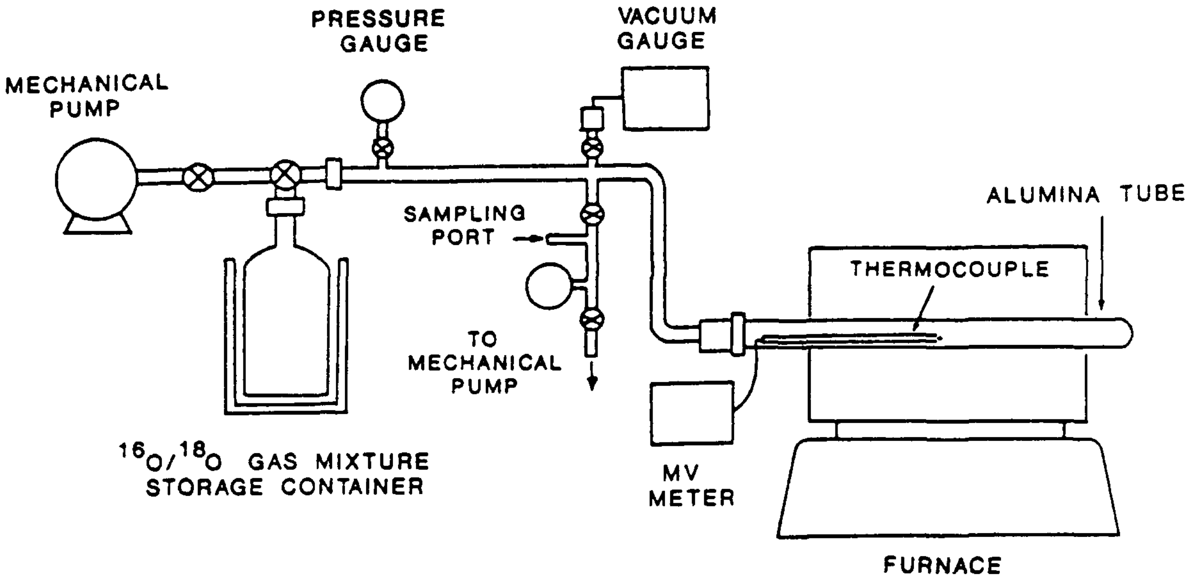

Figure 5. The gas-exchange apparatus used in diffusion experiments.

nitrogen. After pressure was reduced to 60-80 microns, this sorption pump was closed and the 70:30 ^{16}O:^{18}O mixture was introduced into the system by opening the other. After the desired diffusion anneal time elapsed, the oxygen gas mixture was then collected back by submerging the sorption pump in liquid nitrogen. Samples were taken out of the alumina tube and coated with gold prior to analysis of the oxygen tracer penetration using the nuclear reaction technique.

2.4 Nuclear Reaction Analysis (NRA)

In the nuclear reaction analysis experiments it proved useful to employ vitreous silica "standards". These samples of v-SiO_2, General Electric type 124 vitreous silica, were given diffusion anneals in a furnace [11] similar to the one described in Section 2.3.1. The v-SiO_2 samples were 0.4032 cm^2, 0.3175 cm thick, and both faces were polished to a mirror finish.

2.4.1 Non-resonant Nuclear Reaction: $^{18}O(p,\alpha)^{15}N$

The non-resonant $^{18}O(p,\alpha)^{15}N$ (Q=3.97 MeV) nuclear reaction employs a beam of protons in the energy range of 750-800 keV directed on the sample surface. Protons striking an ^{18}O nucleus create an excited ^{15}N nucleus which have a certain probability of decaying via an alpha particle of E_α=3.4 MeV. Our experiments were performed on the 45°S beam line, Figure 6, at the Ohio State University Van de Graaff Laboratory. Details of the experimental beam line are described in J. Cummings' thesis [11]. The experiment is performed in an ORTEC scattering chamber. Figure 7 shows the geometry of the experimental set up. Emitted alpha particles are detected at the lab angle θ=150° in a ORTEC Surface Barrier (500 μm thick) detector with detector characteristics of 16.7 keV Full Width at Half Maximum (FWHM) at E_α=5.486 MeV and a noise width of 10 keV FWHM. A collimator defines a 1.1012 msr solid angle and the ^{58}Ni (2.54 μm thick;

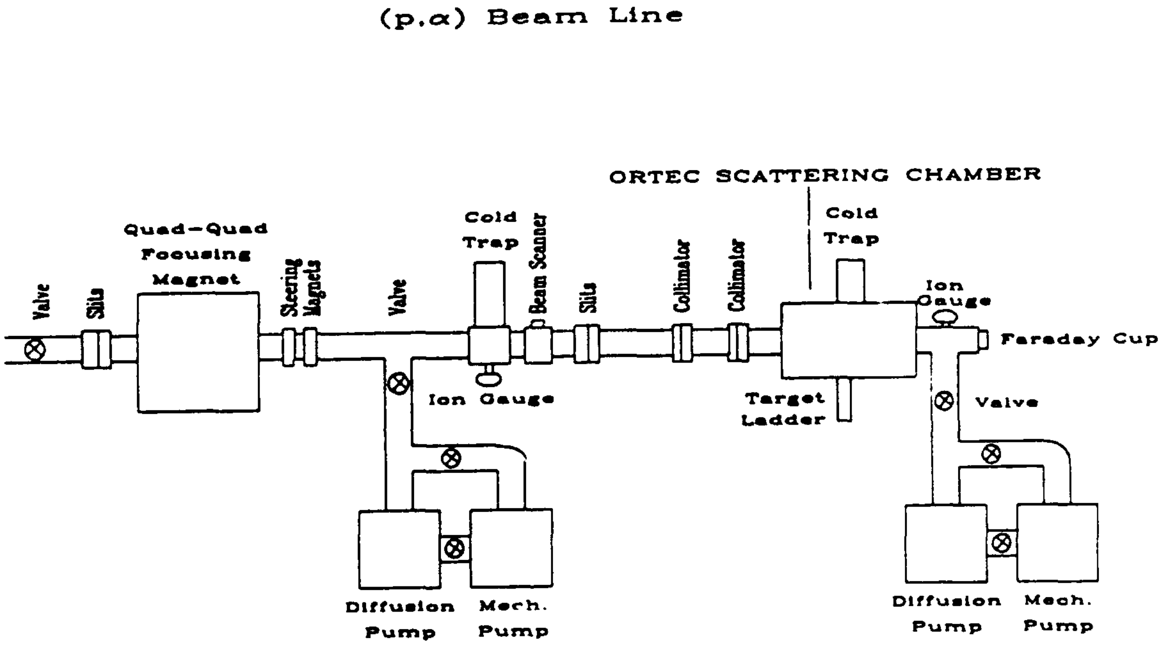

Figure 6. The 45°S beam line used for the non-resonant nuclear reaction analysis.

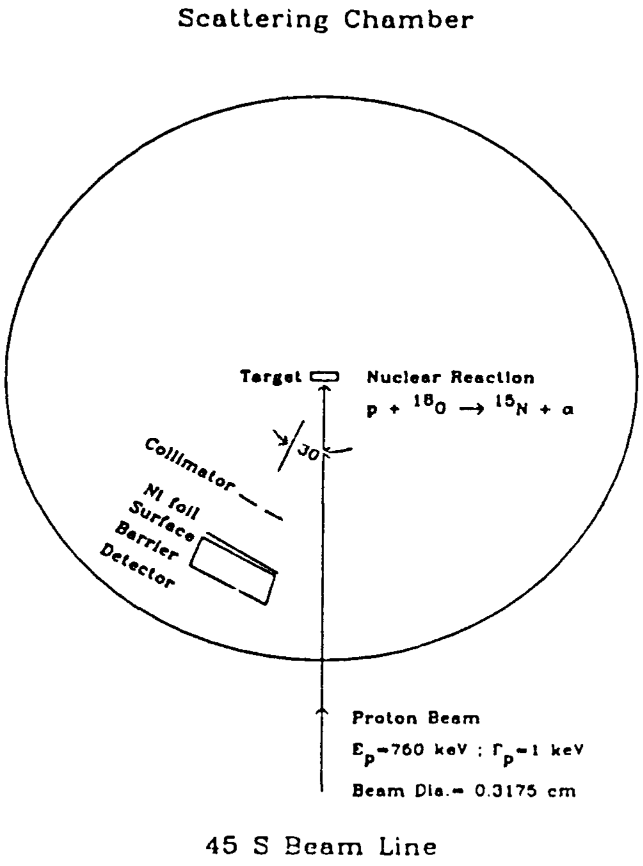

Figure 7. Geometrical set-up of the non-resonant experiment.

0.0022 g/cm^2) foils in front of the detector reduces the scattered proton flux from the low energy (p,p) reaction and also reduces the computer data acquisition dead-time.

The OSU accelerator is a 6.0 MV CN type Van de Graaff (VdG). At the low proton energy of 750 keV this accelerator performs poorly producing unsteady beam characteristics (energy and current). To overcome these difficulties a Hydrogen (H_2) beam is used at an energy of 1.50 MeV ($2E_p$) producing a steady 0.75 MeV energy proton beam with an average 300 nA beam current. The proton beam energy width (FWHM) is measured using the known 0.992 MeV resonance of the ^{27}Al(p,γ)^{28}Si nuclear reaction and was determined to be close to 1 keV.

A schematic of the electronics used for data processing of the signals from the detector is shown in Figure 8. The alpha energy electronic pulse is amplified and split into unipolar and bipolar signals. Unipolar linear energy signals are then processed by the LRS 3511 Analog to Digital Converter (ADC) which is a peak (voltage) sensing ADC of 8 k gain with a 5 μs conversion time. ADC signal linearity is better than $\pm 0.0375\%$ over 99% of its range. Bipolar signals are sent to the EG&G 455 Single Channel Analyzer (SCA, discriminator) and then to the gate and delay generator which creates the gate for the ADC. A Faraday cup at the end of the beam line is not used because the target is thick and completely stops the proton beam. Charge integration of the beam is therefore measured on the target and its signal is sent to the scaler via a TTL/NIM logic level converter. Typical total proton beam flux at the target in these experiments was approximately 3×10^{15} protons. A 10 Hz clock pulse is used to determine total beam time of typically 2 hour duration due to the high cross-section of this non-resonant (p,α) reaction.

Data acquisition is performed on a CAMAC based system that utilizes the LeCroy 3500 system and the Digital Equipment Corporation microVax II minicomputer which runs under Virtual Memory System (VMS). Acquisition Code for Research on Nuclei (ACORN) [13] is a CAMAC based data acquisition program written at the VdG lab.

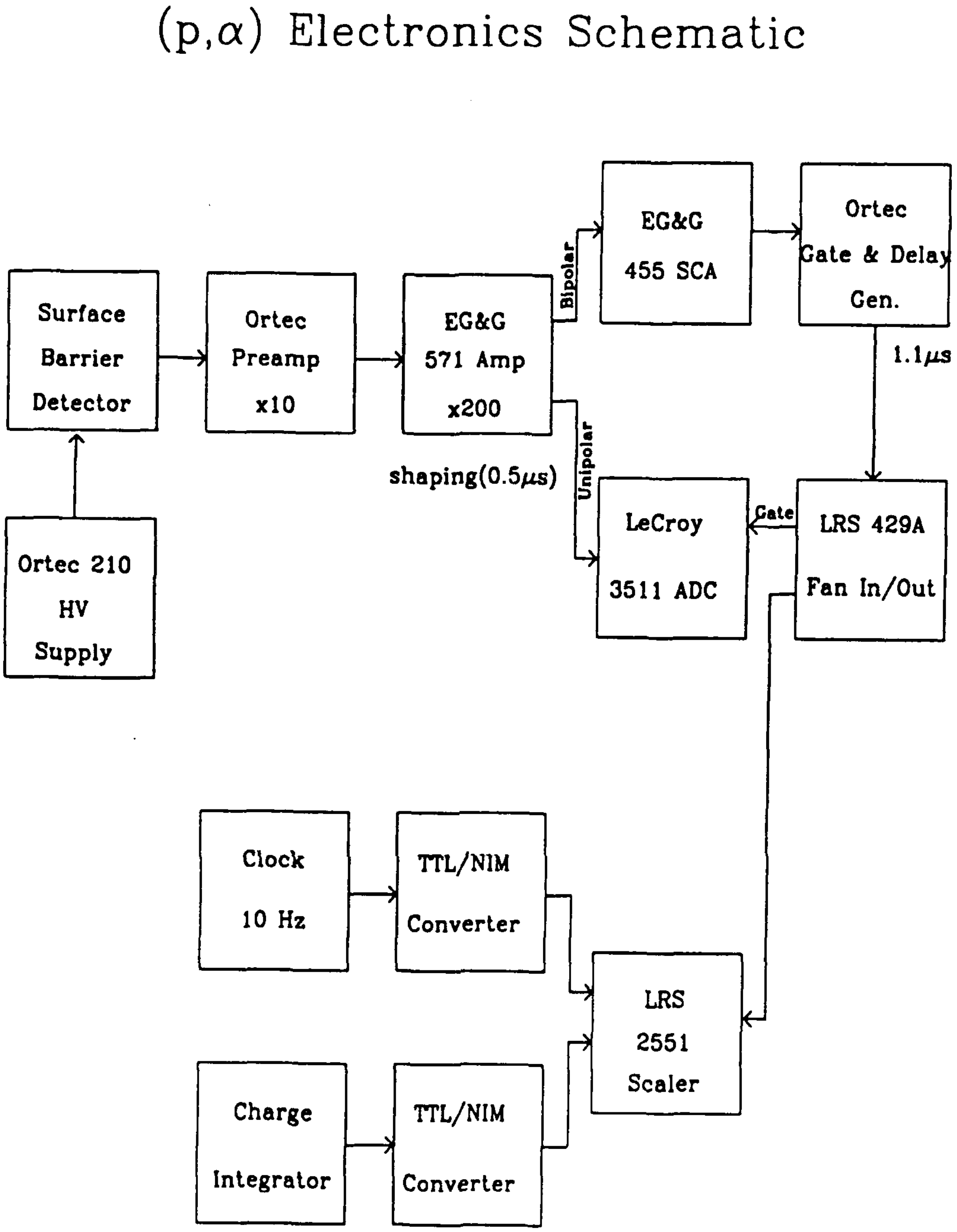

(p,α) Electronics Schematic

Figure 8. A schematic diagram of the electronics used for data processing of signals produced via the non-resonant nuclear reaction.

ACORN acquires events in real time from user-defined CAMAC module configurations, and sorts the events into histograms, based on conditions defined by the user. Another option is to generate event files of the data onto the System Industries 689 Mbyte disks for eventual play back and resorting.

A $^{18}O(p,\alpha)^{15}N$ nuclear reaction cross-section [14] versus energy at the detected alpha angle of 150° is shown in Figure 9a and a typical alpha energy spectrum from a v-SiO_2 "standard" target annealed in ^{18}O for 24 hrs. at 1100°C is displayed in Figure 9b. These "standard" targets were used to develop the NRA technique and data analysis routines. Both histograms are plotted with the x-axis in the $500 \leq E_p \leq 1000$ keV energy region. Characteristic features of the alpha energy spectrum, Figure 9b, are the location of the sample surface at 750 keV and the position of the 629 keV resonance from the $^{18}O(p,\alpha)^{15}N$ reaction.

Incoming proton's and outgoing alpha's lose energy primarily through two processes, 1) electronic energy losses (where energy is lost through ionization and excitation of the target atoms, and 2) elastic energy losses to the screened nuclei (nuclear stopping). A typical energy loss diagram (dE/dx (keV/μm)) for an oxide ceramic is shown in Figure 10 calculated from proton and alpha stopping power tabulations [15,16,17]. The program dE/dX [18], a chi-squared minimization fitting routine presented in Appendix B, is used to fit the stopping powers for alpha's ($2000 \leq E_p \leq 3500$ keV) and proton's ($200 \leq E_p \leq 750$ keV) in the energy regions of interest. A linear fit for the alpha and proton stopping powers in the energy region of interest,

$$S = \frac{dE}{dx} = - M_{\alpha(p)} E_{\alpha(p)} + B_{\alpha(p)},$$

is demonstrated in Figure 11. In fitting NRA spectra constant stopping powers, the average over the energy range of interest, were assumed.

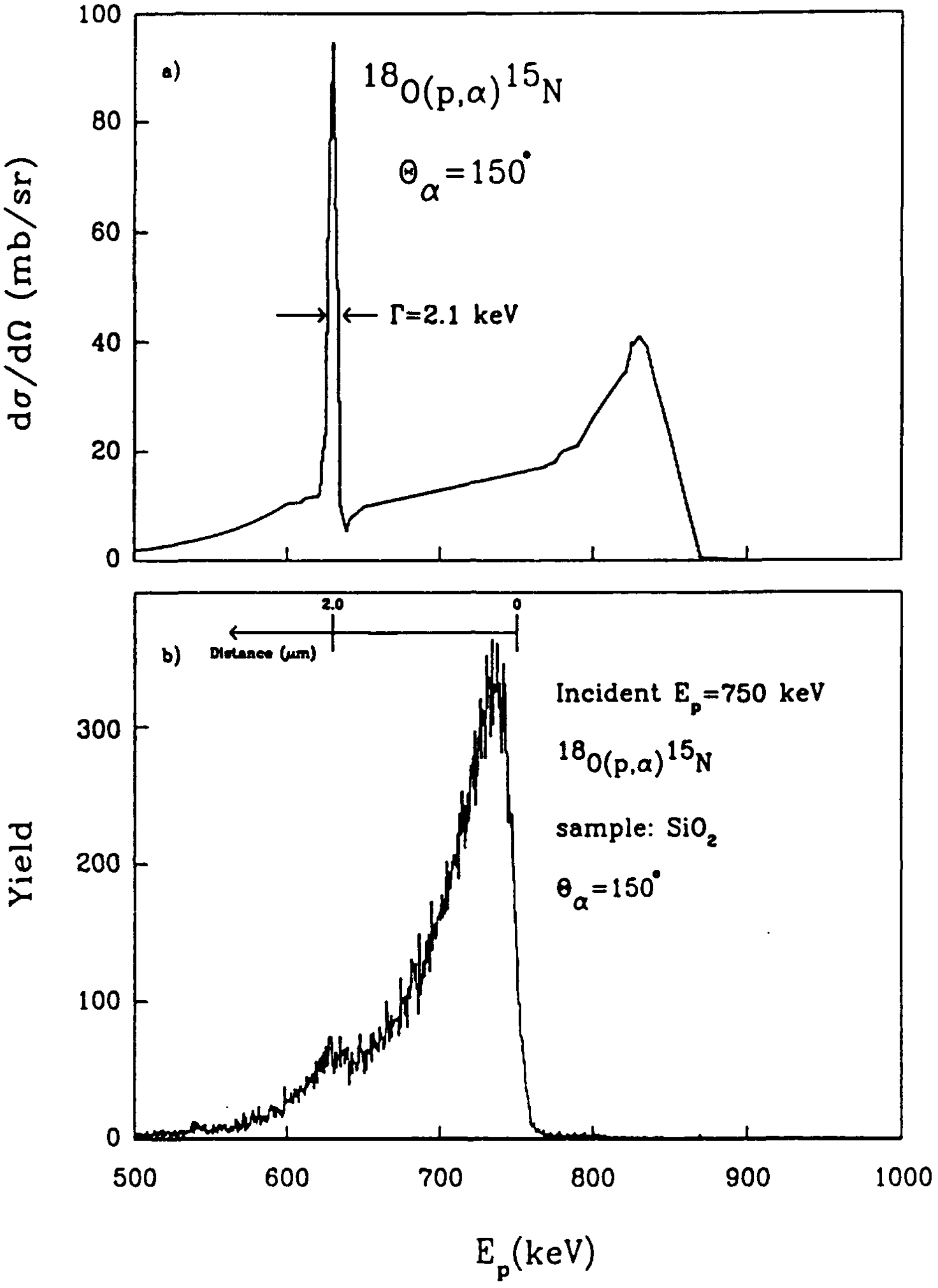

Figure 9a. Experimental cross-section obtained from G. Amsel et.al., Anal. Chem. 39, 1689 (1967).

Figure 9b. Experimental spectrum and its relation to cros-section data.

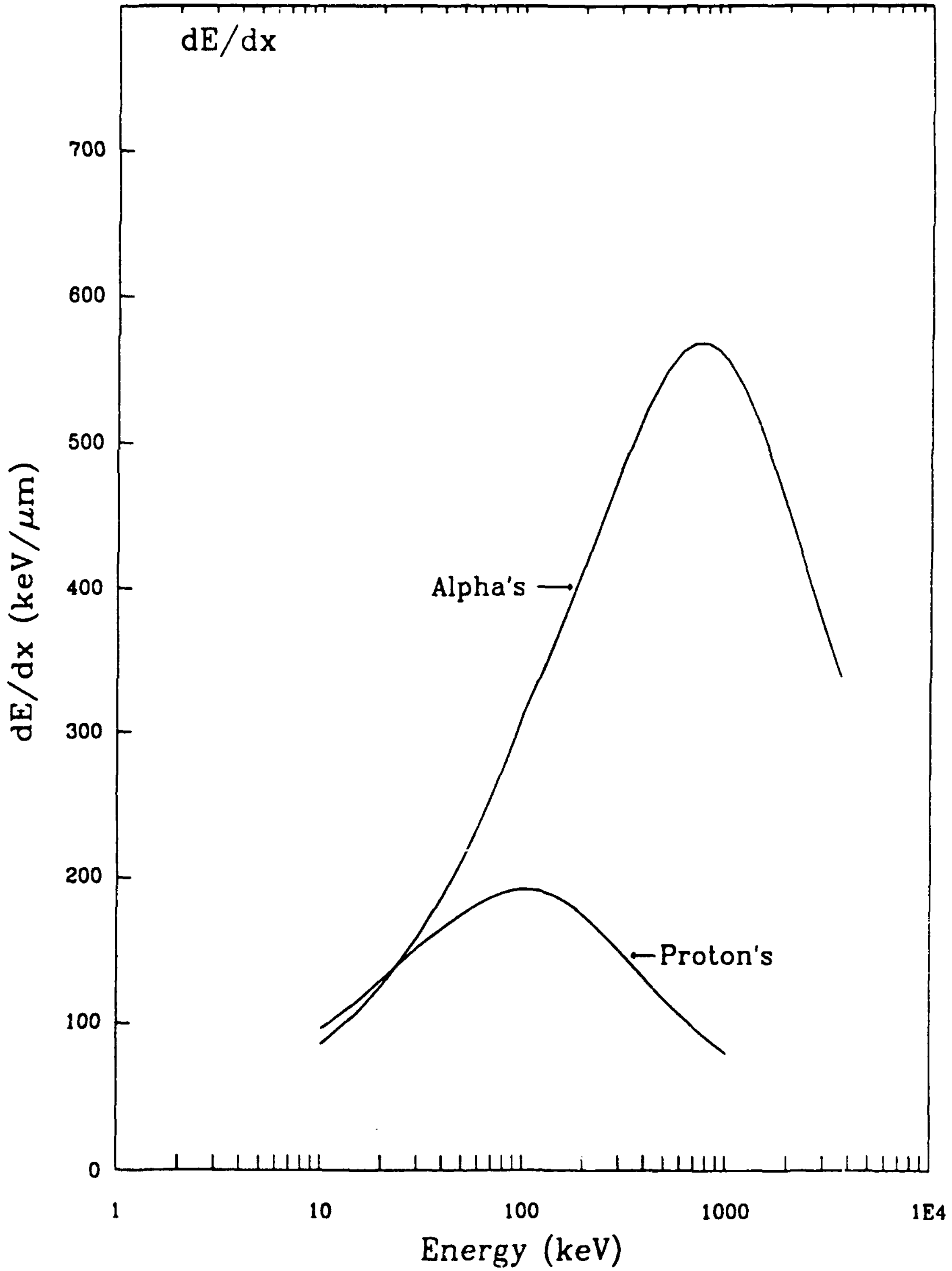

Figure 10. Energy loss diagram for an oxide ceramic

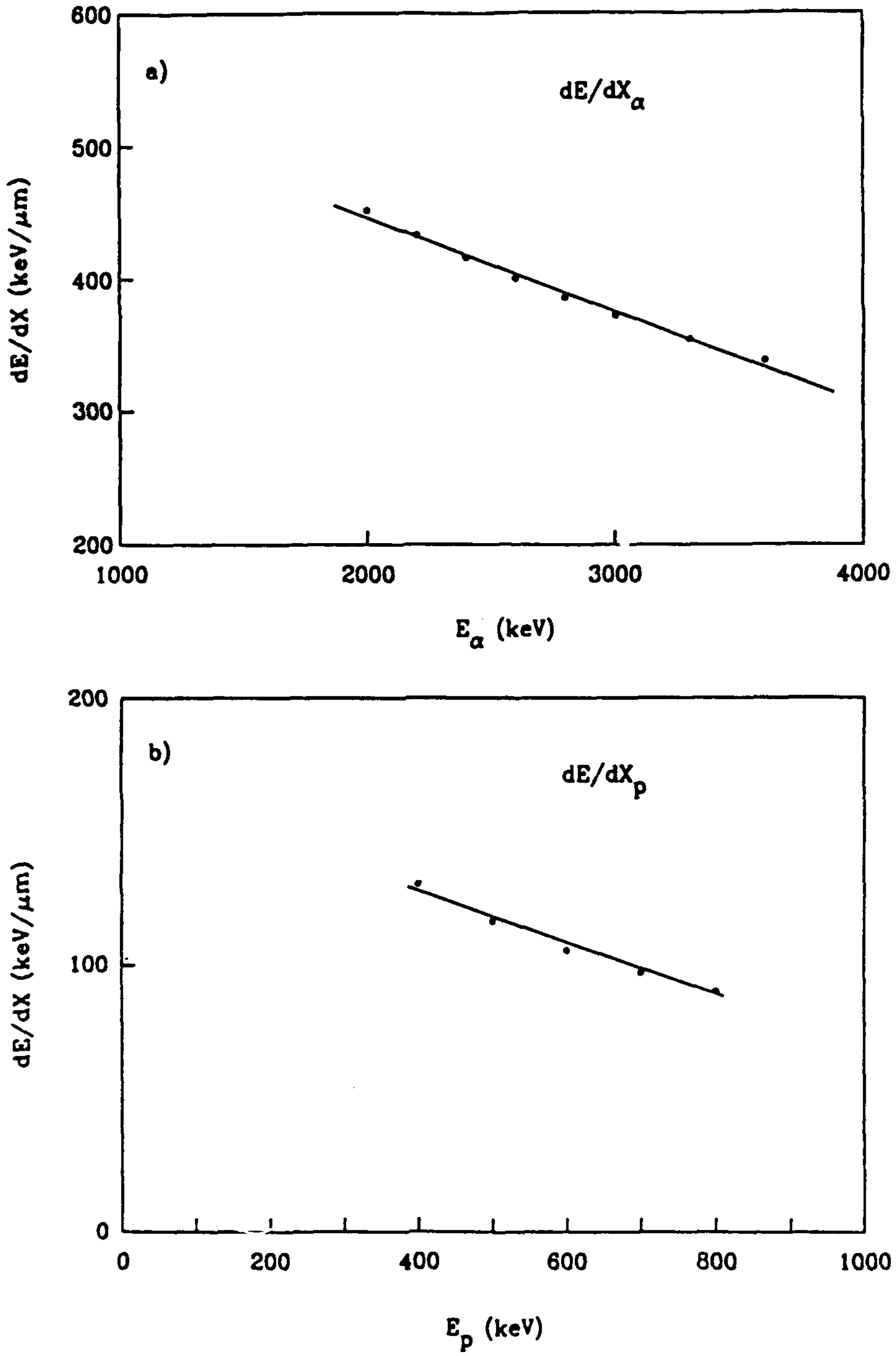

Figure 11. Energy loss calibration for alpha's (top) and proton's (bottom).

Including the nuclear kinematics of the $^{18}O(p,\alpha)^{15}N$ reaction, i.e., the linear relationship of the proton and alpha energies at the angle of interest,

$$E_\alpha = M_{nr}E_p + B_{nr},$$

and combining this with the solutions to the differential equations produces a unique function of the detected alpha particle energy, initial incoming proton energy, and the depth of the reaction,

$$E_{\alpha(d)} = E_{p(x)}[M_{nr} - S_\alpha/(S_p\cos\theta)]+E_{p(x=0)}S_\alpha/(S_p\cos\theta) + B_{nr}$$

where

x = depth of reaction (µm),

$E_{p(x)}$ = proton particle energy at x (keV)

$E_{\alpha(d)}$ = detected alpha particle energy (keV),

S_α, S_p = stopping powers

B_{nr}, M_{nr} = constants of the fitted proton and alpha energies,

$E_{p(x=0)}$ = 750 keV; initial proton energy,

and $\theta = 150°$; detected angle of the alpha particle.

Determination of the ^{18}O tracer concentration also requires knowledge of the energy calibration and linearity of the ADC (2.8 keV/Channel) as depicted in Figure 12b, along with the spreading of the electronic noise shown in Figures 12a and 12c. Figure 12c, the electronic noise width, depicts a constant FWHM/Channel ratio of 0.00742 over the region of interest.

Spreading of the proton and alpha particle energy within the sample was also included in data analysis. Varying the energy of the proton beam, the position of the 629 keV resonance of the $^{18}O(p,\alpha)^{15}N$ nuclear reaction, Figure 13, interacts at various depths, since energy loss is dependent upon the initial beam energy and the material. This energy straggling is linearly proportional to the depth in the energy region of interest [19]. The program ERRFIT [19], a gaussian fitting routine, determines the FWHM, Γ_s, of the resonance for the various depths of interaction. The solid line in Figure 13 is drawn to

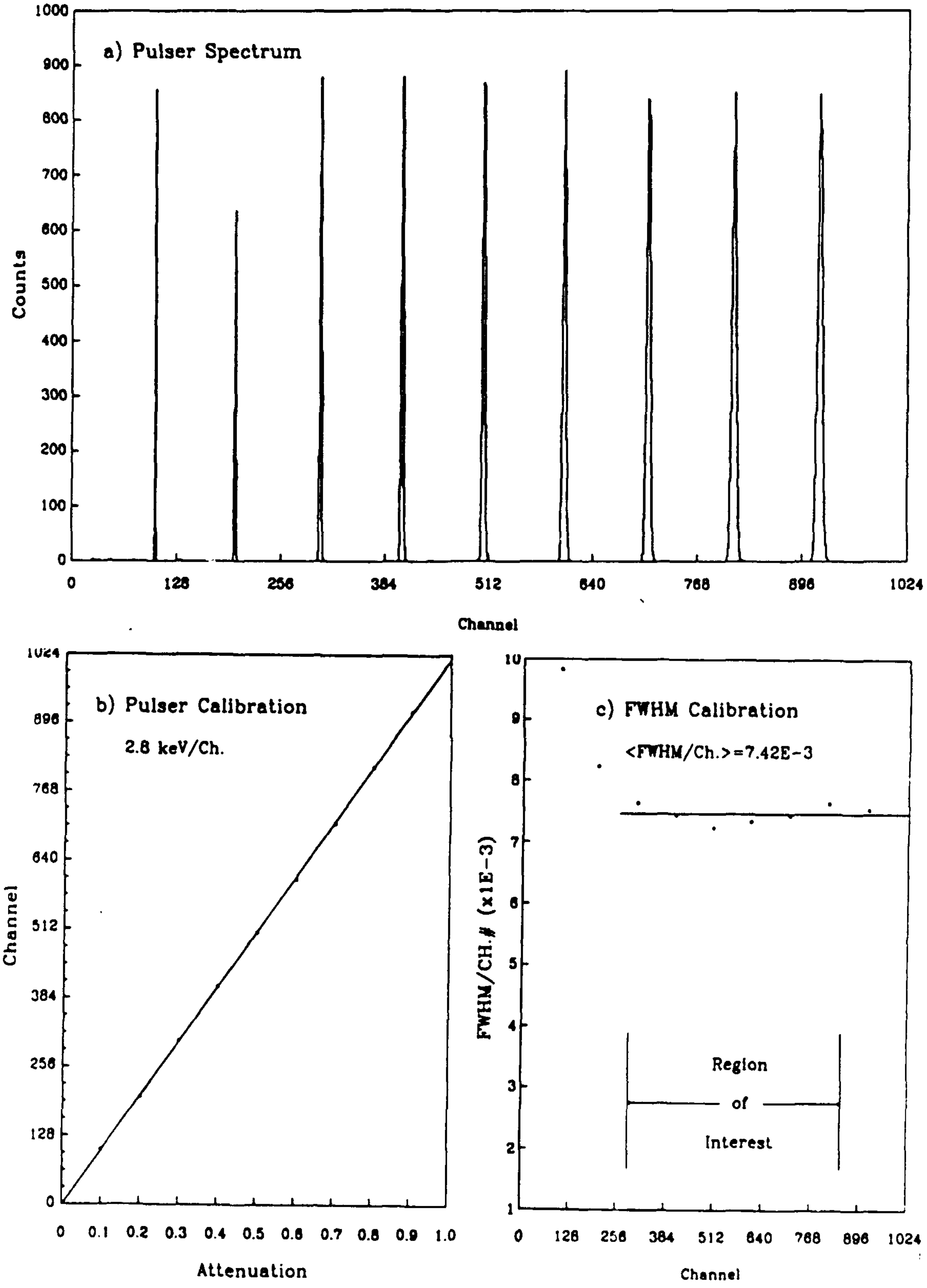

Figure 12. Pulser spectrum (top), linearity calibration (b), and FWHM calibration (c) for the ADC.

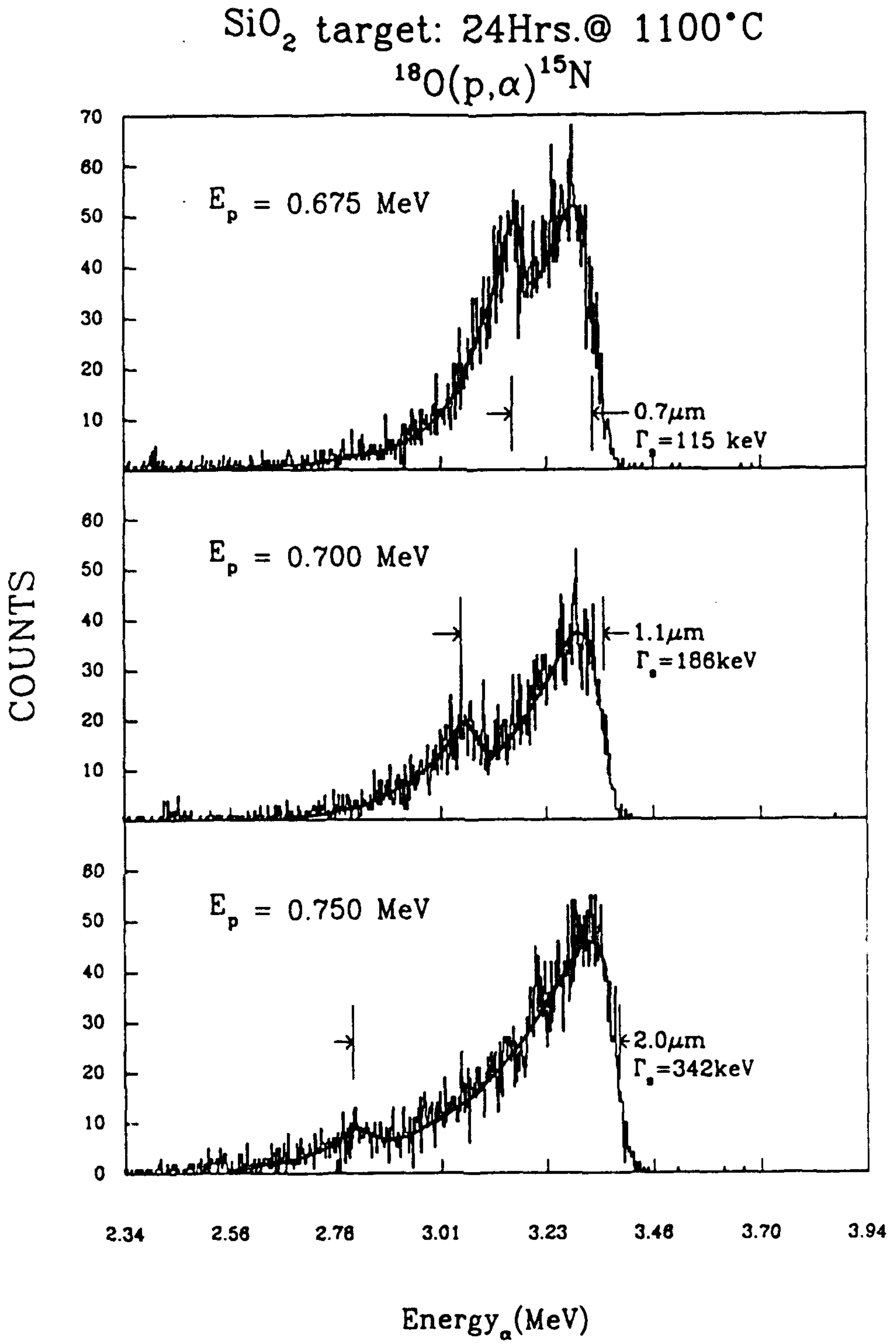

Figure 13. Effect of varying the proton beam energy on the 629 Kev resonance position and spreading.

guide the eye and does not represent a fit using an assumed concentration profile.

Lastly, carbon build-up on the target must also be included in the analysis. Carbon build-up is produced from carbon molecules in the diffusion pump oil located along the beam line, Figure 6, which are attracted to the target due to charging of the target by the proton beam. Reduction of the carbon level in the target chamber is performed by the use of LN_2 cold traps located at various positions along the beam line. Since carbon on the sample surface degrades the beam resolution (FWHM), it is monitored by performing a Rutherford Backscattering (RBS) experiment before and after the nuclear (p,α) experimental run. Figure 14 shows a typical RBS spectrum for v-SiO_2 with a thin ^{197}Au coating. This thin ^{197}Au coating prevents a build-up of charge on the target which would yield a reduced measurement of the proton flux. Comparing the FWHM of the $^{197}Au(p,p)$ peak before and after the nuclear (p,α) experiment provides an assessment of the increase of the proton energy width (FWHM) due to carbon build-up on the sample surface. Build-up of carbon was determined not to be a problem due to the relatively short, 2 hour, experimental runs.

Calculation of the diffusion coefficient involves a trial and error convolution process where an ideal spectrum is obtained from knowledge of the energy loss (dE/dx) together with the known solution to the diffusion equation. The ideal number of counts in each energy sector, N_i, is related to the concentration by

$$N_i = C(x_i)\,\Delta x_i\ \sigma(x_i)\ \rho_{OX}\,L\,\Delta\Omega$$

where

$C(x_i)$ = average fractional concentration of the tracer in the interval x_i

$\sigma(x_i)$ = nuclear reaction cross section for energies over x_i

ρ_{OX} = number density of oxygen in the material

L = number of incident protons

and $\Delta\Omega$ = detector solid angle of observation.

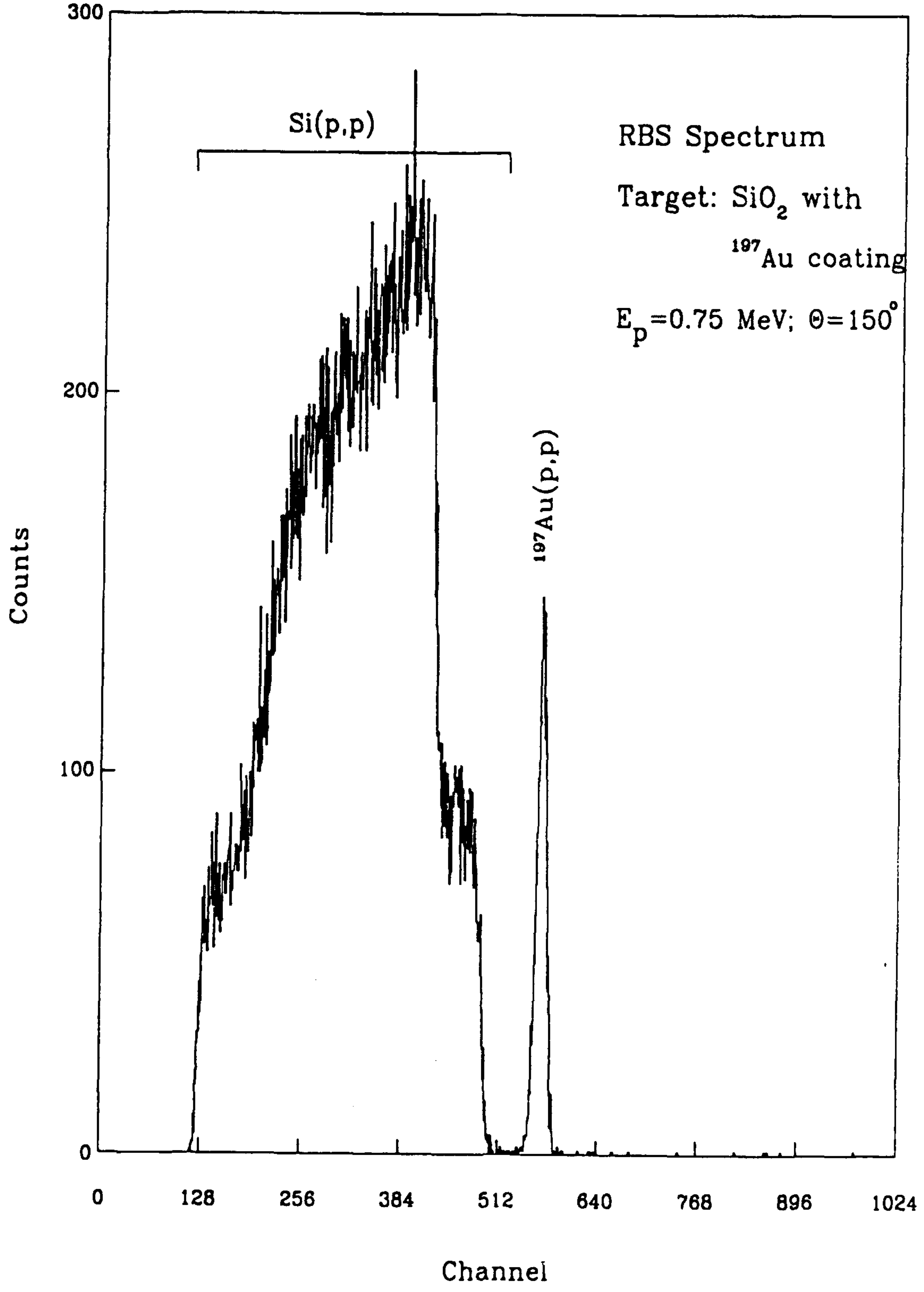

Figure 14. RBS spectrum of silicon oxide coated with a thin layer of gold.

The ideal spectrum obtained using the above equation is then convoluted with the various experimentally determined spreading functions as shown in Figure 15 and then compared with the experimental spectrum. The assumed diffusion coefficient which gives the best fit to the experimental depth profile is taken as the experimental value of the apparent oxygen tracer diffusion coefficient.

2.4.2 Resonant Nuclear Reaction: $^{18}O(p,\gamma)^{19}F$

The main advantage of the resonant versus non-resonant techniques is that gamma-rays (γ-rays) do not lose energy but are only affected by absorbtion in the material via three processes, 1) photoelectric effect, 2) Compton effect, and 3) pair production. This allows a tracer concentration to be probed deeper within the sample, i.e., 10's of microns versus a few microns for the non-resonant (p,α) technique. Depth profiling is accomplished by detecting the γ-ray yield ($E = 6.321$ MeV @ $\theta = 60°$) from the $E_p = 1169$ keV resonance of the $^{18}O(p,\gamma)^{19}F$ nuclear reaction at various depths within the target sample [21].

The resonance energy resolution, $\Gamma_r = 0.6$ keV FWHM, with a proton beam energy resolution, $\Gamma_p = 1$ keV, provides a 0.03 μm depth resolution for SiO_2. The cross-section at energies of off resonance is negligible in comparison to that of on resonance. The energy of the proton beam enters the target at an energy above resonance, the proton loses energy as the particle traverses the material until at a depth (x) the resonance energy is attained. At this thin particular depth the reaction of interest creates the γ-ray of interest which is detected. At a greater depth the proton energy is less than the resonance where again the cross-section is negligible.

The $^{18}O(p,\gamma)^{19}F$ cross-section at a lab angle $\theta=60°$ is 44.5 μb/sr for the decay of the $9101 \longrightarrow 2780$ keV state of ^{19}F [22]. Acquiring acceptable statistics requires approximately 8 hours of beam time. Due to the long beam time experimental runs, carbon build-up was observed to be a problem. Although initially promising, the low

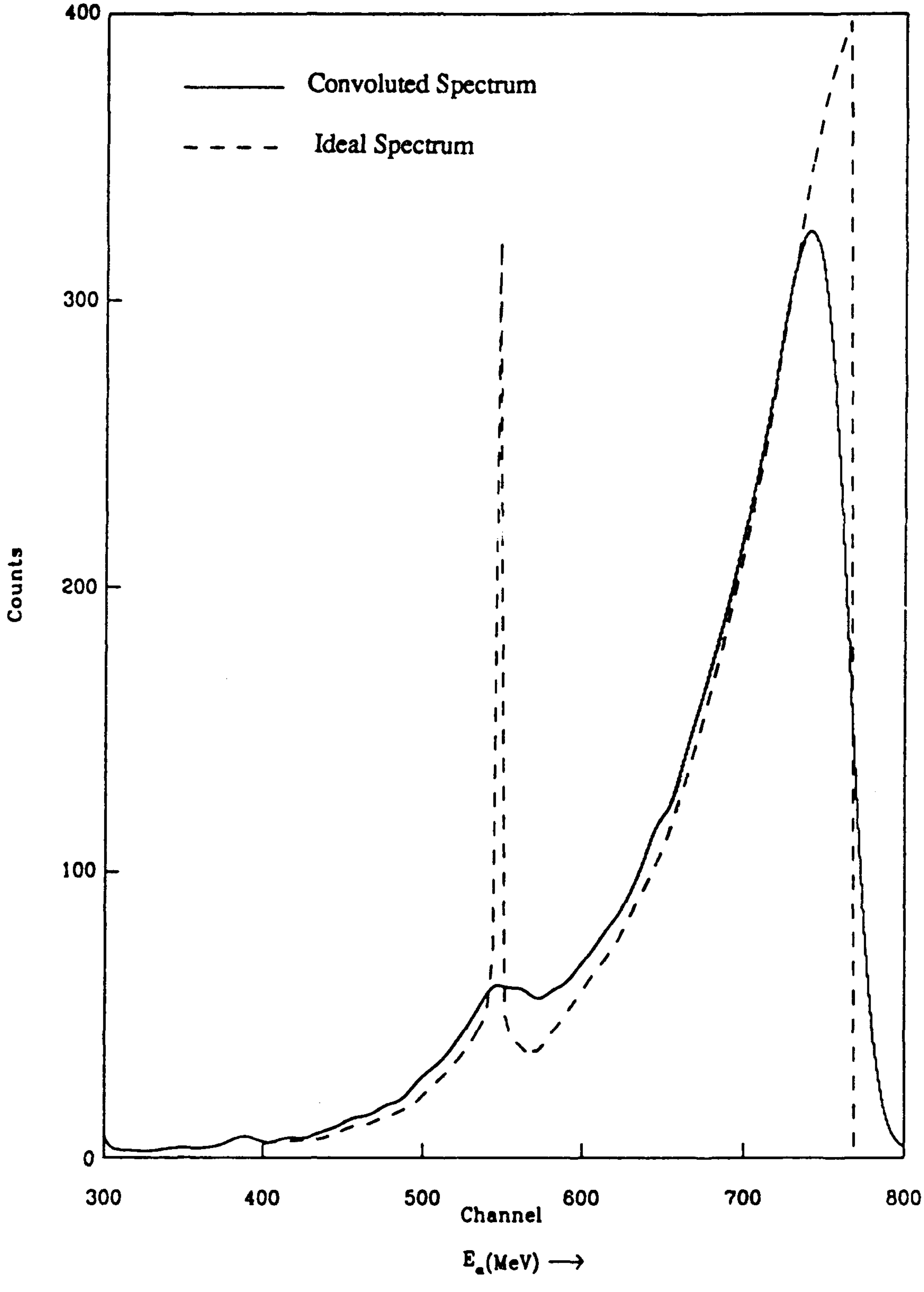

Figure 15. Theoretical (without energy spreading; dash) and experimental spectrum (with energy spreading; solid).

counting rate coupled with the contamination limited the usefulness of this technique.

3. RESULTS AND DISCUSSION

3.1 Microstructural Characterization

3.1.1 Calcium Zirconate

A scanning electron micrograph of a sample cut from the interior of the $CaZrO_3$ disk hot-pressed at 1400°C and 20.7 MPa using the powder from Alfa Products is shown in Figure 16. The density, measured using a Micromeritics multivolume pycnometer, was found to be 97.6% of the theoretical density, 4.97 g/cm^3. Using a Zeiss Videoplan, the average grain size was measured as 12.13 microns based on 100 grains.

Some of the hot-pressed $CaZrO_3$ samples which were thermally etched had microstructures which clearly showed small particulates in the grain boundaries and in the grains. Figure 17 shows scanning electron micrographs of these particulates within the grain boundaries. Using a 200 Kv JEOL 200cx Transmission Electron Microscope, these particulates were observed using two samples cut from the hot-pressed disk at 1400°C and 20.7 MPa. The surface was studied using a sample which was ion-milled from one side only. To study the inner surface, a second sample was ion-milled from both sides.

Based on the TEM micrographs, diffraction patterns and EDS spectra, precipitates found on the grain boundaries very near the free surface of the sample during annealing (Figure 18) were identified as cubic zirconia (ZrO_2). Formation of zirconia is presumably due to calcium depletion of the exposed surface [23]. The grain boundary region contained a glassy phase with isolated crystalline particulates. Figure 19 shows a selected area diffraction pattern confirming the glassy nature of the grain boundary phase. This glassy phase was initially presumed to have been formed as a result of the impurities

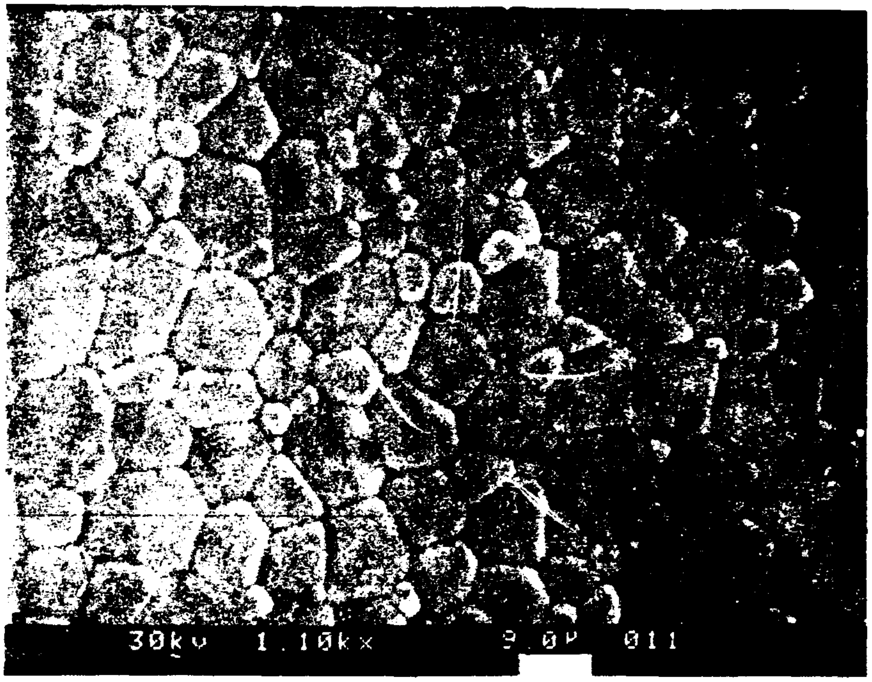

Figure 16. A SEM image, using secondary electrons, of $CaZrO_3$ hot pressed at 1400°C and 20.7 MPa taken at 30 KV and 1100x magnification.

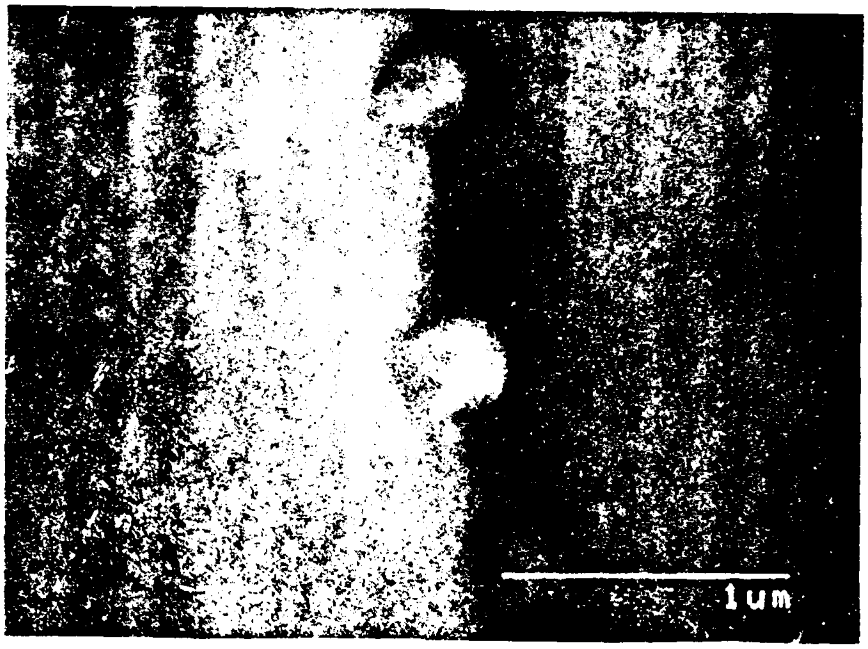

Figure 17. A TEM micrograph of particulates observed in the $CaZrO_3$ grain boundary taken at 200 KV and 31.6 KX magnification.

Figure 18. A TEM micrograph of a cubic zirconia grain in the $CaZrO_3$ grain boundary taken at 200 KV and 5 KX magnification.

Figure 19. A TEM micrograph of a selected area diffraction pattern of the glassy phase in the $CaZrO_3$ grain boundary.

present in the sample which segregated at the grain boundaries. However, energy dispersive X-ray analysis of the grain boundaries and the precipitates showed a significant amount of molybdenum and silicon which suggests contamination of the sample surface by the molydisilicide heating elements. Because of this observation, subsequent samples were loosely wrapped in platinum foil to prevent contamination.

Grain boundaries in the sample interior (greater than 100 microns away from the sample surface during annealing) showed no glassy grain boundary phase but did reveal a crystalline phase. EDS analysis of this crystalline phase did not show any molybdenum but showed calcium, aluminum and silicon. This phase was determined to be gehlenite ($2CaO \cdot Al_2O_3 \cdot SiO_2$) based on electron diffraction results.

3.1.2 Barium Zirconate

A TEM micrograph of $BaZrO_3$ hot pressed at 1400°C and 20.7 MPa using the powder from TAM is shown in Figure 20. The density of $BaZrO_3$ was measured to be 95.8% of the theoretical density. The average grain size is about 0.6 micron. X-ray diffraction analysis of the hot-pressed sample showed a single phase $BaZrO_3$. This is corroborated by TEM observations which revealed neither second phases nor glassy phases in the grains or in the grain boundaries as shown in Figure 21. EDS analyses within the grains as shown in Figures 22a and b indicate that impurities such as silicon and aluminum are in solid solution with $BaZrO_3$. Similar results are obtained across a grain boundary as shown in Figure 22c. Small precipitate-like grains shown in Figure 23 were also analyzed by EDS (Figures 24a and b) indicating the same result of impurities forming a solid solution with $BaZrO_3$.

3.1.3 Strontium Zirconate

When the as-received $SrZrO_3$ powder from Universal Energy Systems was hot pressed at 1400°C and 20.7 MPa, a relatively low density of 91.8% of theoretical was

Figure 20. A TEM micrograph of $BaZrO_3$ hot pressed at 1400°C and 20.7 MPa taken at 200 KV and 37 KX magnification.

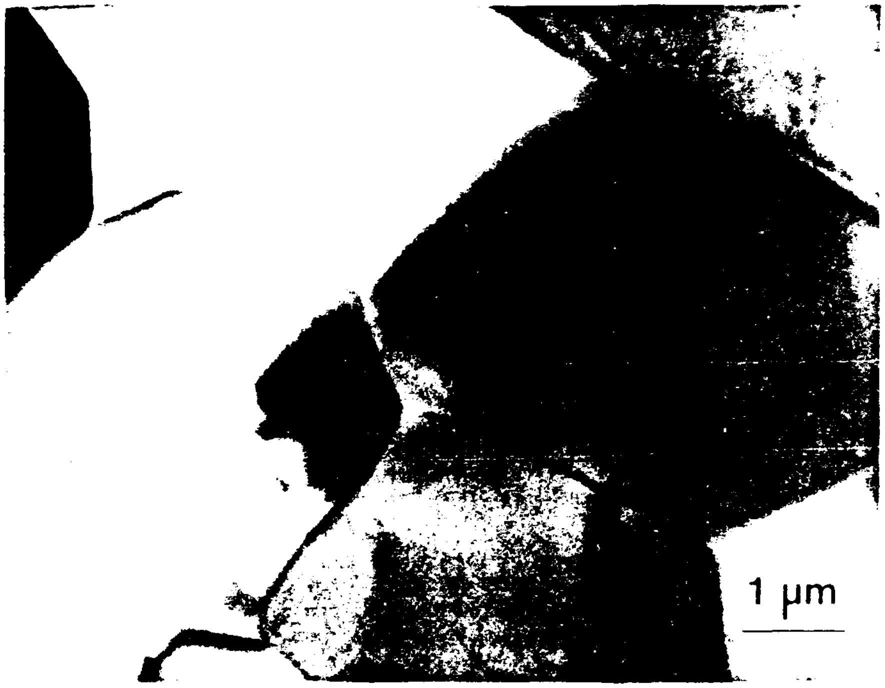

Figure 21. A TEM micrograph of $BaZrO_3$ showing the absence of second phases or glassy phases in the grains or in the grain boundaries (200 KV, 50 KX).

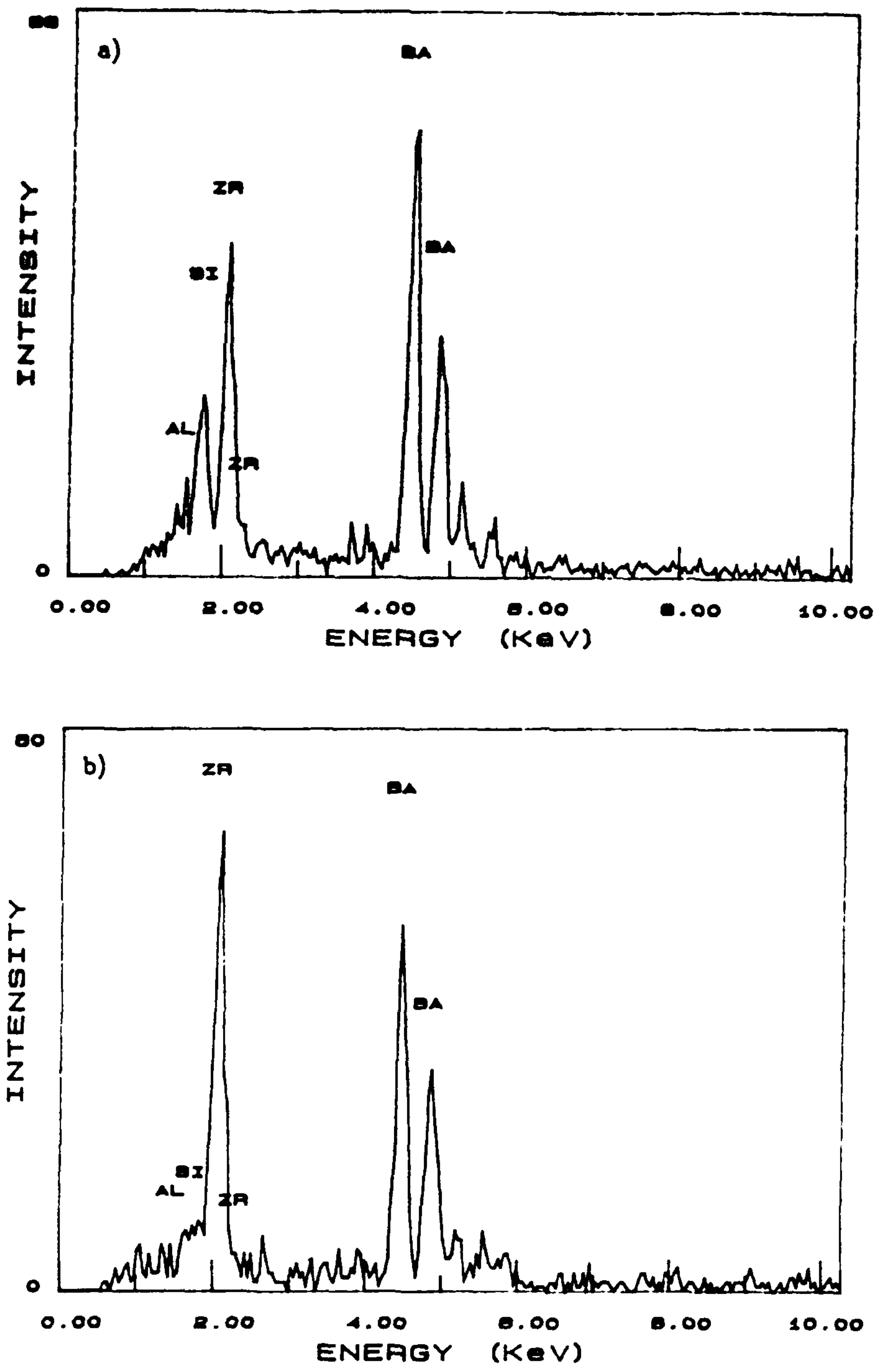

Figure 22. EDS spectra (a and b) taken from two different $BaZrO_3$ grains.

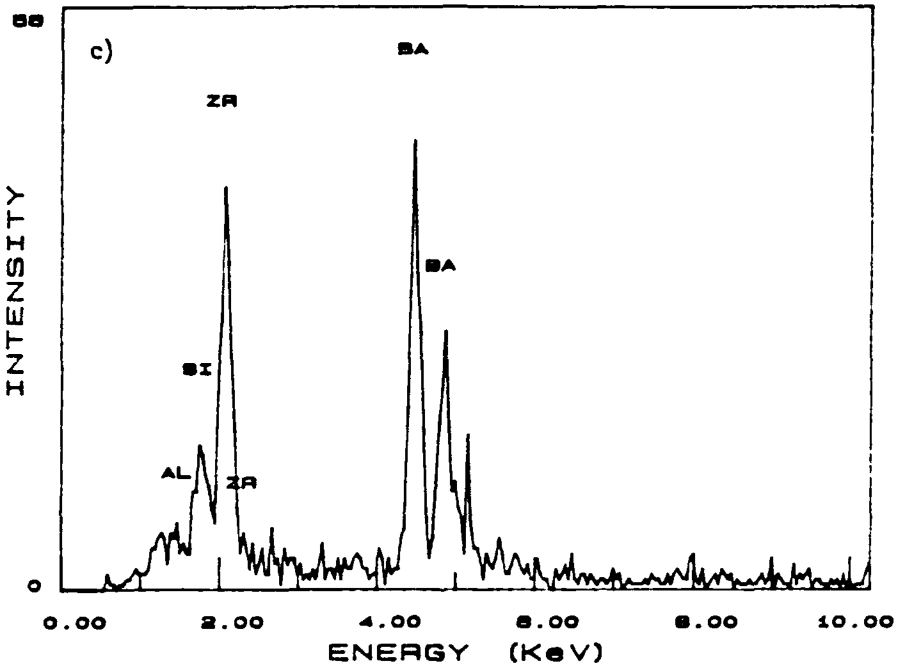

Figure 22c. EDS spectra taken across a $BaZrO_3$ grain boundary.

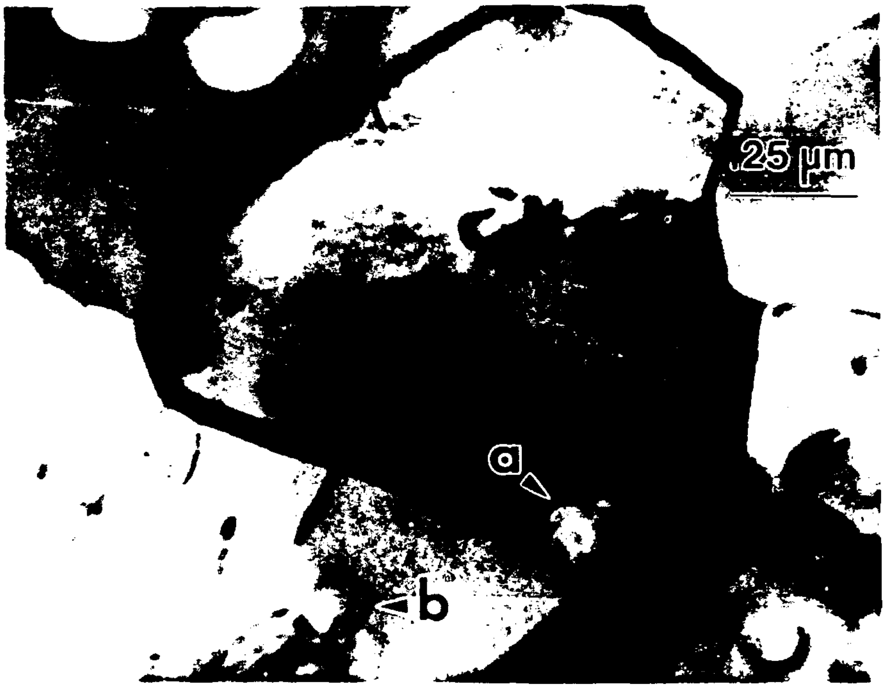

Figure 23. A TEM micrograph of $BaZrO_3$ showing small precipitate-like grains in the grain boundary and within a grain (200 KV, 50 KX).

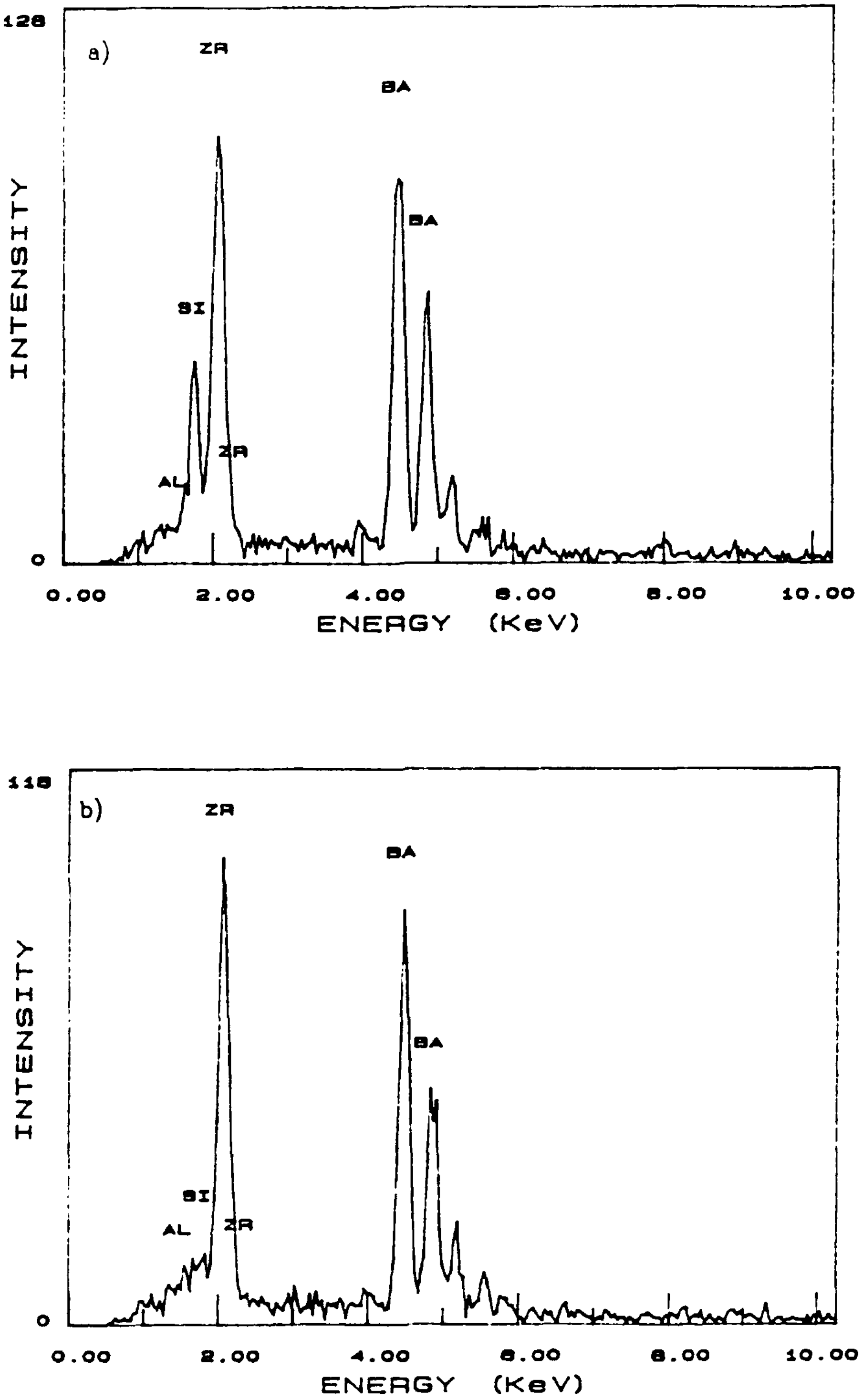

Figure 24. EDS spectra taken from small precipitate-like grains in $BaZrO_3$ as shown in Figure 23.

obtained. Observation of the microstructure of the sintered sample as shown in Figure 25 showed large grains with a significant amount of porosity. The initial grain size of the powder was measured and found to be on the order of 200 microns. The grains are believed to be hard agglomerates produced during calcination of the sol-gel derived powders. Thus the as-received powders were ball milled in isopropyl alcohol for 40 hours using zirconia grinding media prior to hot pressing to reduce the grain size and improve sintering. A micrograph of the hot-pressed sample is shown in Figure 26. An average grain size of 5 microns and a density of 97.6% of theoretical were determined for this sample.

3.2 Vaporization Studies

The weight loss curves were plotted as the weight lost per unit apparent projected surface area versus time at a given temperature. Figure 27 shows the weight loss for dry-pressed $CaZrO_3$ at a temperature of 1750°C, Figure 28 shows the weight loss curve for dry- pressed $CaZrO_3$ at a temperature of 1850°C and Figure 29 shows the same for dry-pressed $CaZrO_3$ at a temperature of 1970°C. These three figures are condensed into a single master plot in Figure 30 for comparison on a common scale.

Evaporation rate is usually analyzed using the Langmuir equation which expresses the flux of material, J, away from the sample as:

$$J = (\alpha P)/(2\pi mKT)^{1/2} \qquad (1)$$

where α = Langmuir sublimation coefficient

p = vapor pressure

m = molecular weight

K = Boltzmann's constant and

T = temperature.

When there is a significant activation energy barrier to evaporation, α is much less than 1. This is typical of many pure oxide materials. In pure metals, however, α is

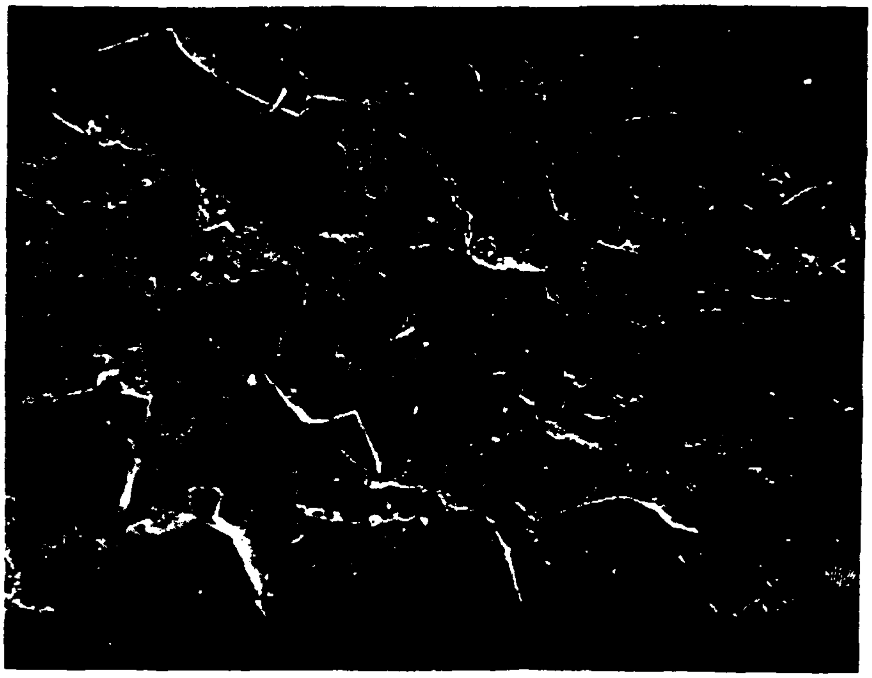

Figure 25. A SEM image, using secondary electrons, of as-received $SrZrO_3$ powder hot pressed at 1400°C and 20.7 MPa taken at 25 KV and 141x magnification.

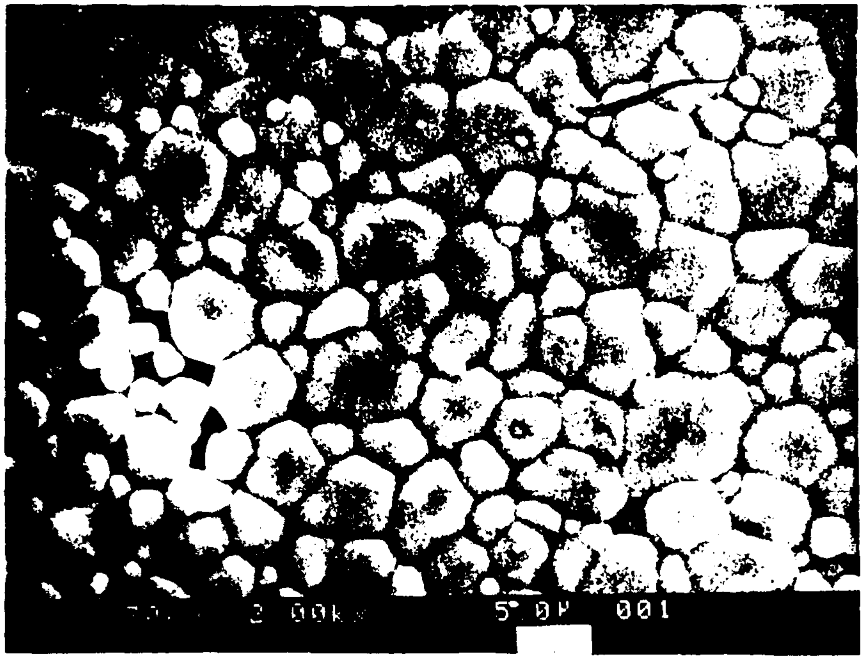

Figure 26. A SEM image, using secondary electrons, of ball-milled $SrZrO_3$ powder hot pressed at 1400°C and 20.7 MPa taken at 30 KV and 2000x magnification.

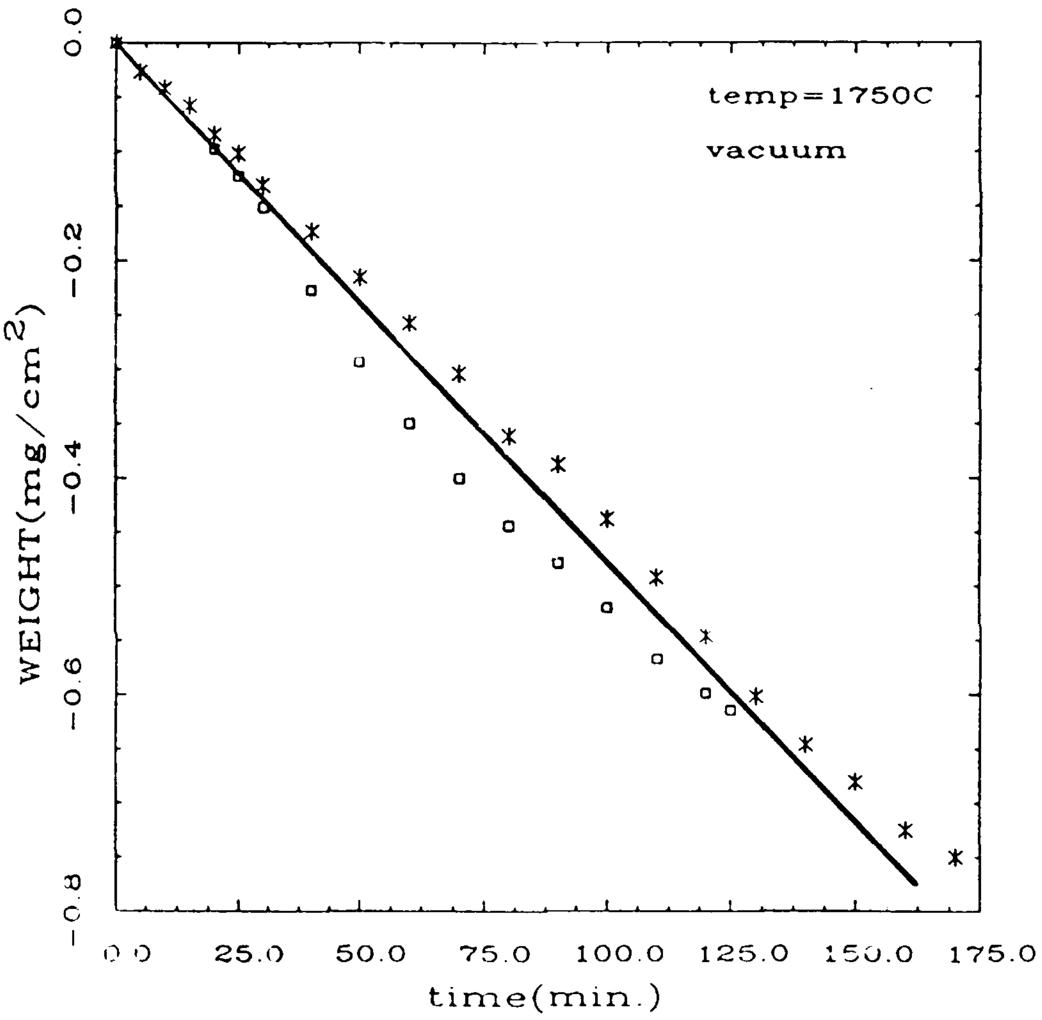

Figure 27. A plot of the measured weight loss per unit apparent projected surface area vs. time for dry-pressed $CaZrO_3$ held at 1750°C for about 150 minutes in vacuum.

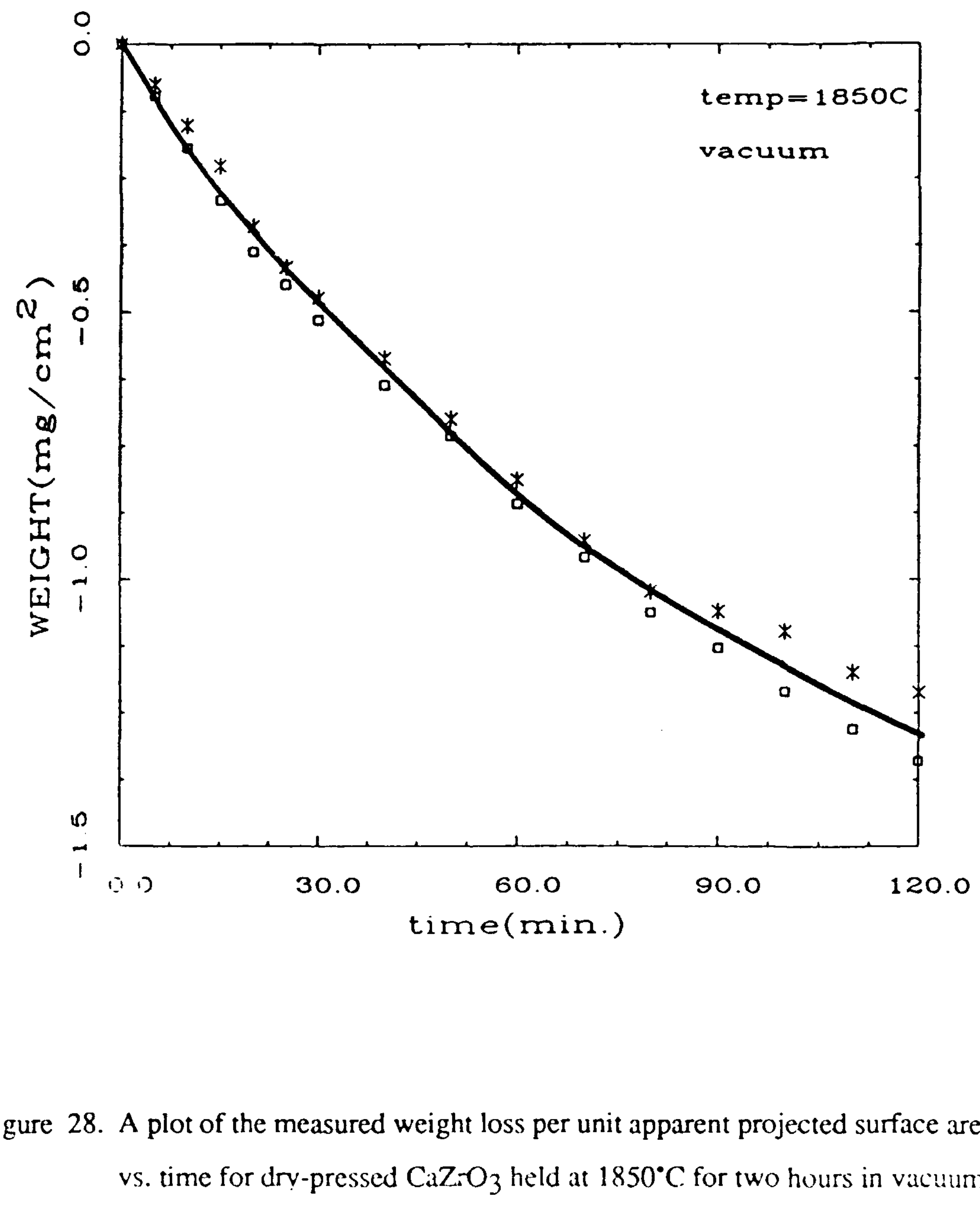

Figure 28. A plot of the measured weight loss per unit apparent projected surface area vs. time for dry-pressed $CaZrO_3$ held at 1850°C for two hours in vacuum.

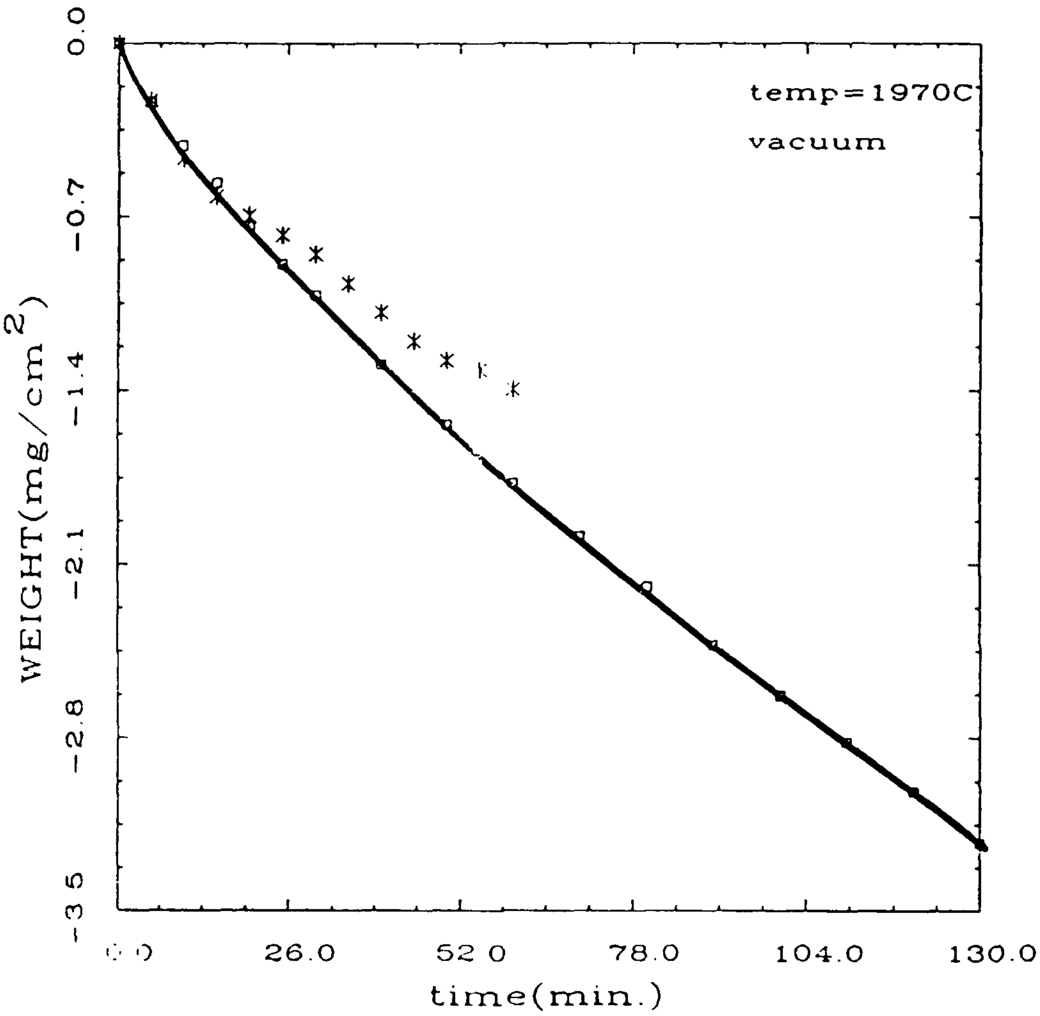

Figure 29. A plot of the measured weight loss per unit apparent projected surface area vs. time for dry-pressed $CaZrO_3$ held at 1970°C for 130 minutes in vacuum.

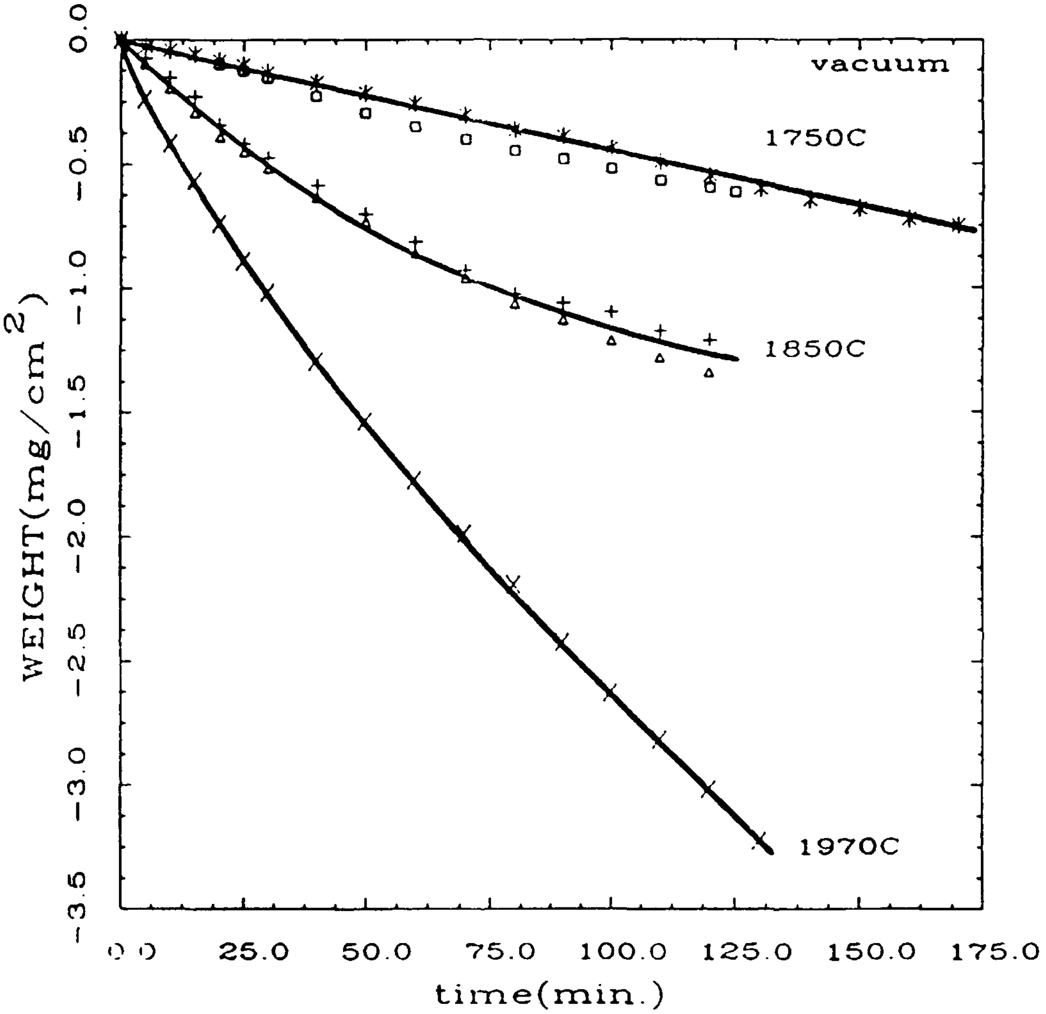

Figure 30. A plot of the measured weight loss per unit apparent projected surface area vs. time for dry-pressed $CaZrO_3$ at three different temperatures.

usually very close to unity and the evaporation rate is given by the relation:

$$J = P/(2\pi mKT)^{1/2}$$

In incongruently evaporating systems, like some mixed oxides, a concentration gradient is developed in the material as evaporation takes place and the Langmuir analysis cannot be directly applied. This concentration gradient often leads to condensed phase diffusion controlled kinetics. A higher degree of complexity is introduced when a phase change accompanies the compositional change leads to a concommitant volume change. Stresses arising as a result of this volume change may cause microcracking to be initiated. Microcracking will be initiated only in the volume which is sufficiently depleted. After an initial transient, the effective diffusion distance might become a constant due to the recurrent initiation of microcracking immediately behind the depleted zone.

Considering diffusion controlled kinetics alone, the rate would be given by:

$$dw/dt = AD(dc/dx) \tag{2}$$

where dw/dt = rate of loss of weight

A = area

D = diffusion coefficient

dc/dx = concentration gradient

and integration yields standard parabolic kinetics. However when the total effective diffusion distance remains a constant, the rate of material loss can be significantly altered from following a parabolic trend.

The microstructures of the fracture surface of the dry-pressed $CaZrO_3$ before vaporization, after vaporization at 1850°C and after vaporization at 1970°C are shown in Figures 31a, 31b and 31c, respectively. From these pictures before and after vaporization, it is not possible to unambiguously determine whether the number of pores have increased or decreased after vaporization.

From Figure 30, in the case of dry-pressed $CaZrO_3$, there is sometimes a curvature observed although the kinetics appear to be fairly linear especially for the highest and the

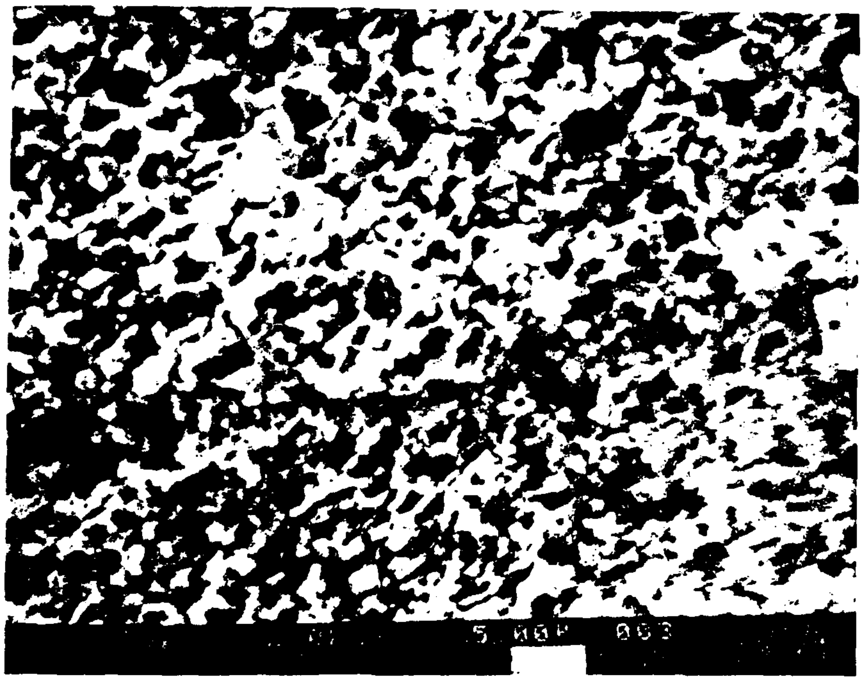

Figure 31a. A SEM image, using secondary electrons, of the fracture surface of dry-pressed CaZrO3 before vaporization at a magnification of 2000x.

Figure 31b. A SEM image, using secondary electrons, of the fracture surface of dry-pressed $CaZrO_3$ after vaporization at 1850°C for 2 hours, at a magnification of 2000x.

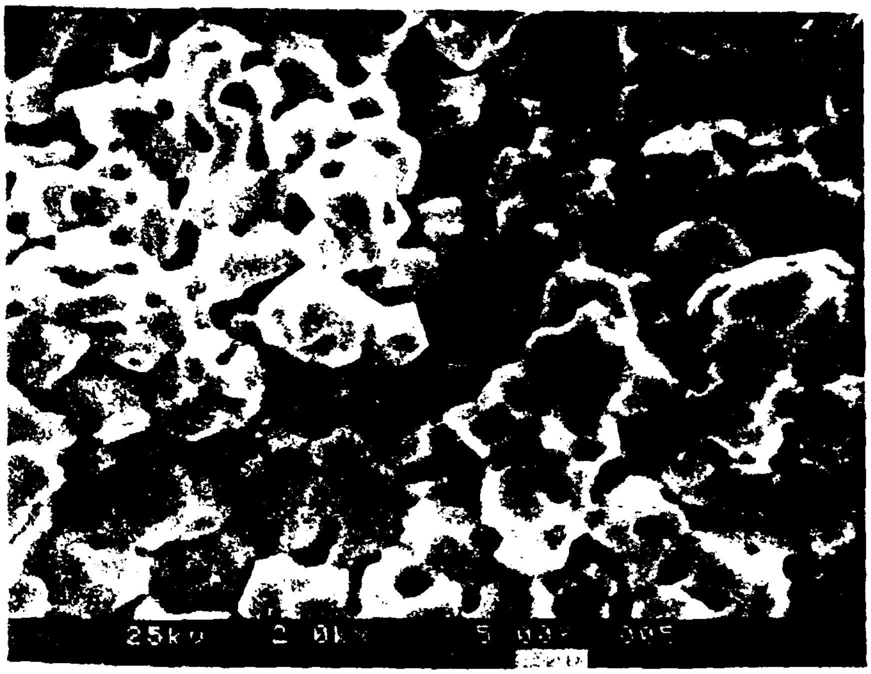

Figure 31c. A SEM image, using secondary electrons, of the fracture surface of dry-pressed $CaZrO_3$ after vaporization at 1970°C for about 130 minutes, at a magnification of 2000x.

lowest temperatures.

If there is no microcrack formation, it is reasonable to expect parabolic kinetics in $CaZrO_3$ because CaO vaporizes preferentially from $CaZrO_3$. However, microcracks cannot be avoided considering the fact that there is a volume reduction of about 44% involved in the $CaZrO_3$ to cubic solid solution phase transformation.

Figure 32 shows the vapor pressures of pure oxides, CaO, SrO, BaO and ZrO_2 over their respective condensed phases plotted as a function of temperature from data in the literature [1]. It clearly demonstrates the much higher vapor pressures of the alkaline-earth oxides compared to ZrO_2. Knowing the free energy of formation of $CaZrO_3$ from CaO and ZrO_2 [24], the vapor pressure of CaO over $CaZrO_3$ (solid) can be computed assuming unit activity of ZrO_2 and $CaZrO_3$. Computing $P_{CaO}(CaZrO_3)$ in this manner, $P_{CaO}(CaZrO_3)$ together with $P_{CaO}(CaO)$ and $P_{ZrO_2}(ZrO_2)$ are plotted for comparison in Figure 33. It is clear CaO will be the predominant vapor species over condensed $CaZrO_3$ below about 2200°C.

There is further evidence of preferential evaporation of CaO from microstructural analysis. Dot mapping of Ca and Zr by EDS on the surface of dry-pressed $CaZrO_3$ samples held at 1850°C for 2 hours, shown in Figures 34a and 34b illustrate this point. Table 2 summarizes the EDS spot analyses carried out on the surface of dry-pressed and hot-pressed $CaZrO_3$ samples after evaporation and confirms the dot maps.

X-ray analysis of dry-pressed $CaZrO_3$ samples are shown in Figures 35 and 36. Figure 35a shows the XRD pattern obtained for dry-pressed $CaZrO_3$ before vaporization while Figure 35b shows the same for dry-pressed $CaZrO_3$ held at 1970°C for about an hour. Figure 35b is consistent with a single phase cubic solid solution of ZrO_2. Figures 36a and 36b show the XRD patterns obtained from the outer and fracture surfaces respectively of dry-pressed $CaZrO_3$ held at 1850°C for 2 hours. The outer surface is completely covered by a single phase of cubic CaO-ZrO_2 solid solution. The fracture surface reveals both the cubic CaO-ZrO_2 solid solution and the orthorhombic

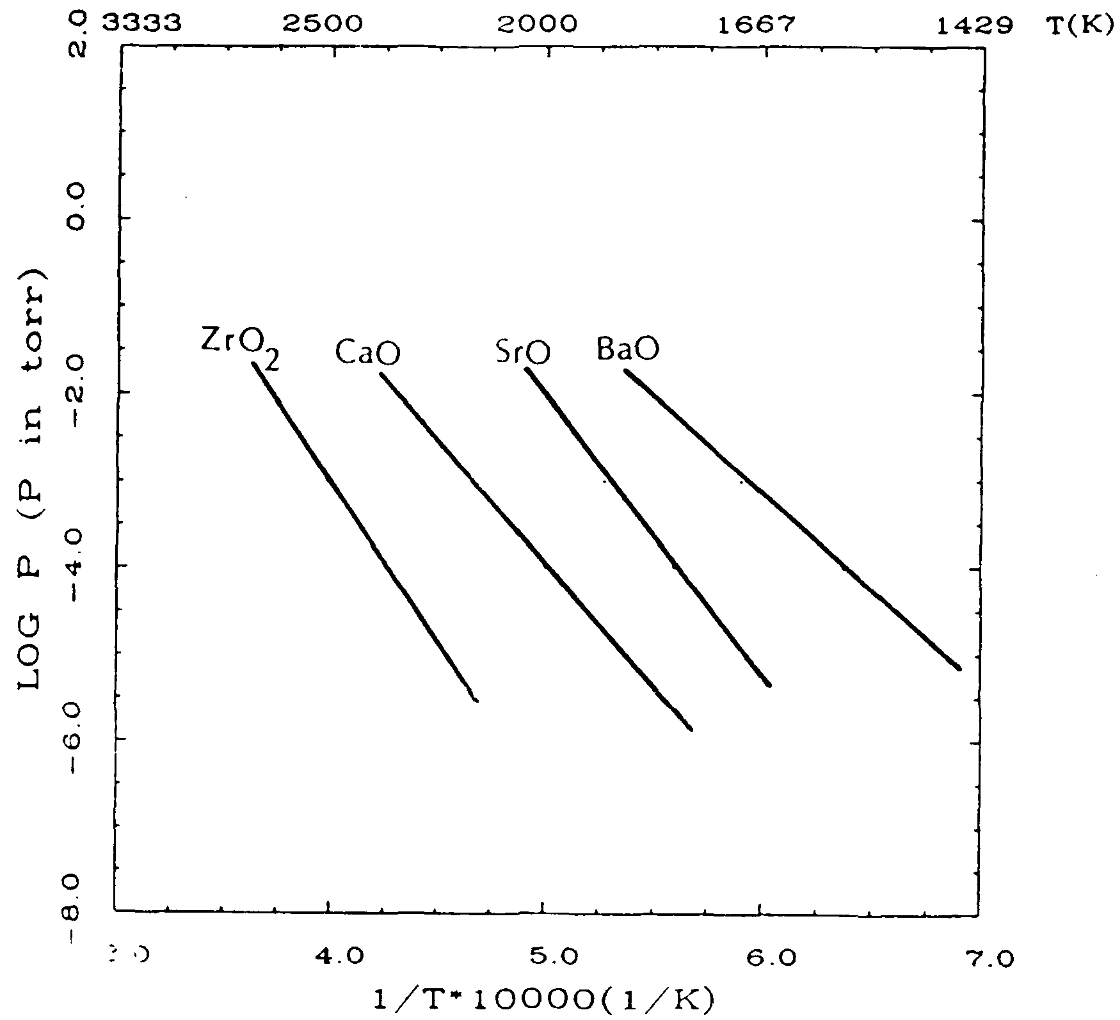

Figure 32. A plot showing the relative values of the vapor pressures of the pure oxides, BaO, SrO, Cao and ZrO_2, over their respective condensed phases, as a funtion of temperature.

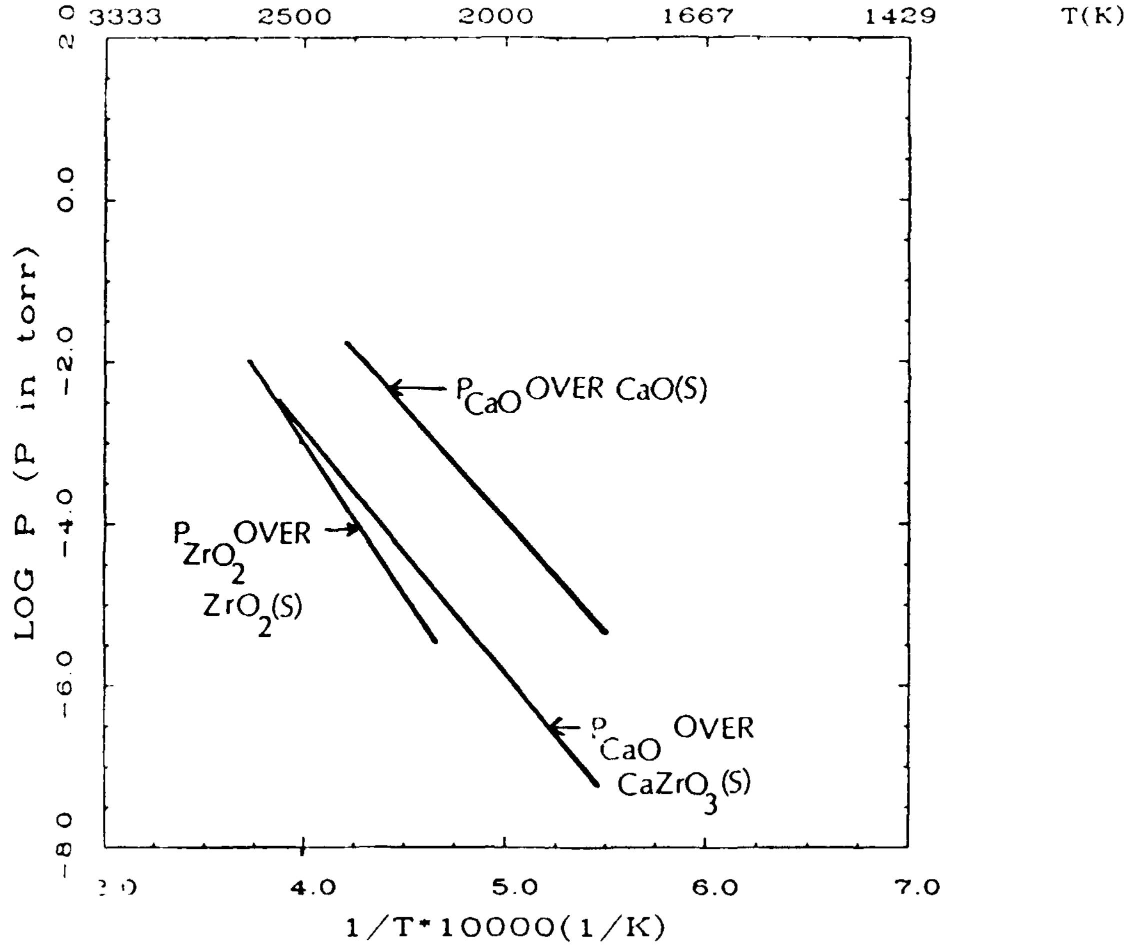

Figure 33. A plot showing the vapor pressure of CaO over $CaZrO_3$(solid) and CaO(solid) and the vapor pressure of ZrO_2 over ZrO_2(solid), as a function of temperature.

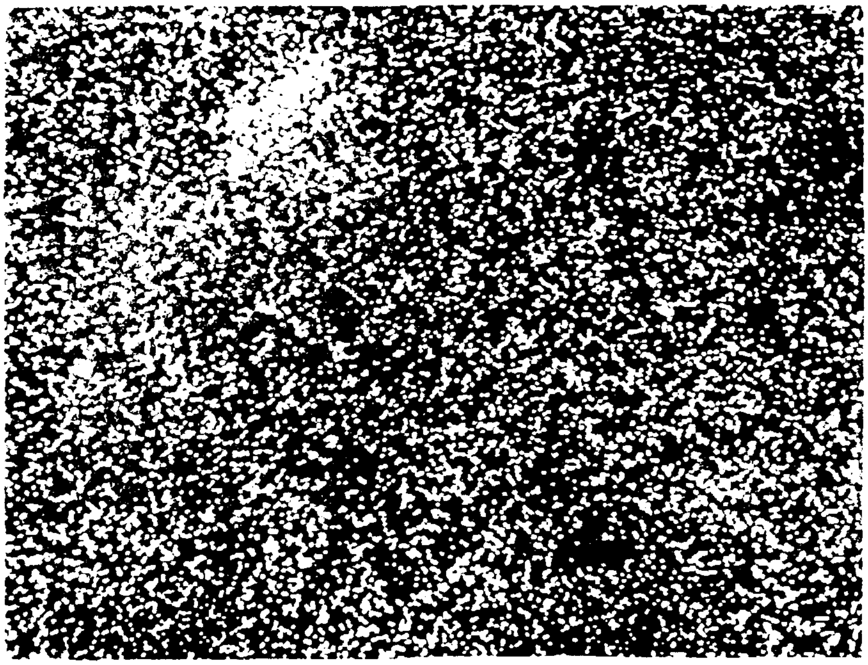

Figure 34a. Calcium dot map of the outer surface of dry-pressed $CaZrO_3$ after vaporization at 1850°C for 2 hours.

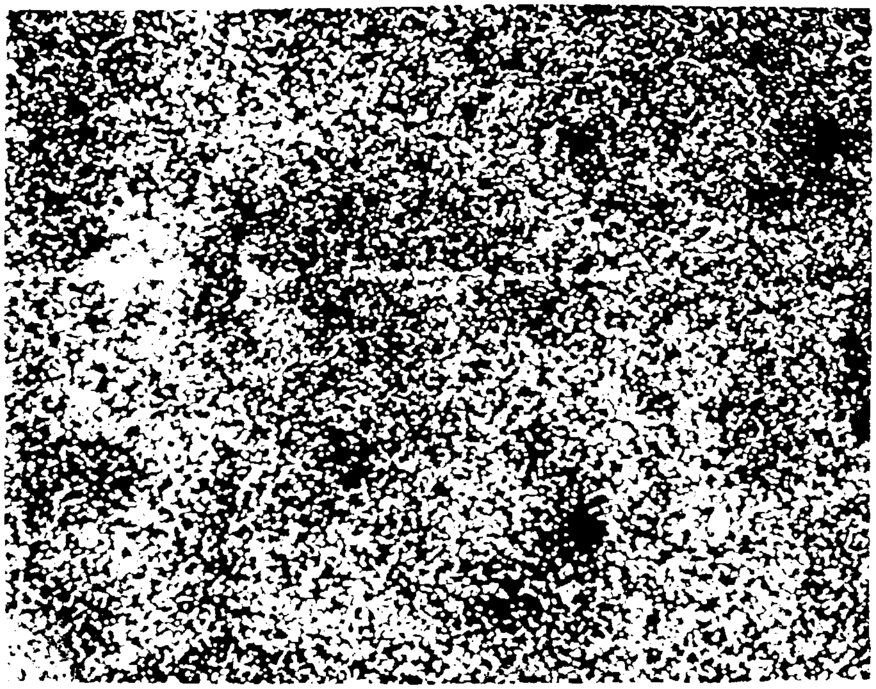

Figure 34b. Zirconium dot map of the outer surface of dry pressed $CaZrO_3$ after vaporization at 1850°C for 2 hours.

Table 2. Results of the EDS analysis carried out on the outer surface of dry-pressed and hot-pressed $CaZrO_3$, after vaporization.

Temperature(°C)	Atomic % Zr	Atomic % Ca
Dry pressed $CaZrO_3$		
1750	86.46	13.54
1750	85.18	14.82
1850	93.77	6.23
1850	92.45	7.55
1850	93.43	6.57
1970	98.36	1.64
1970	98.12	1.88
Hot pressed $CaZrO_3$		
1850	84.07	15.93
1850	85.28	14.72

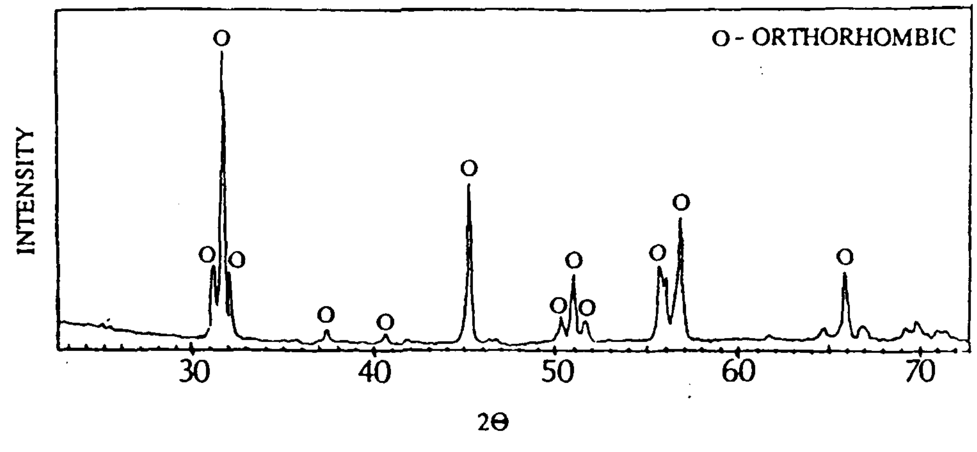

Figure 35a. X-ray diffraction pattern for dry-pressed $CaZrO_3$ before vaporization showing an orthorhombic crystal stucture.

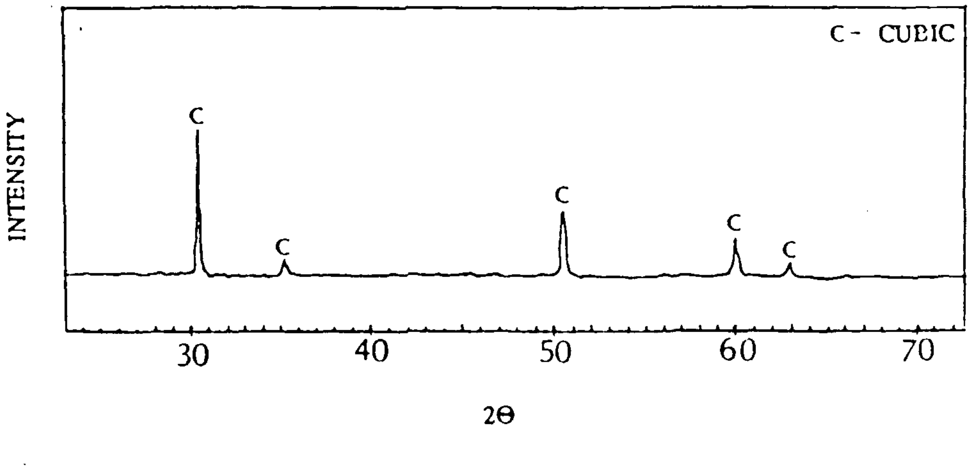

Figure 35b. X-ray diffraction pattern for the outer surface of dry-pressed $CaZrO_3$ after evaporation at 1970°C showing the zirconia solid solution cubic phase.

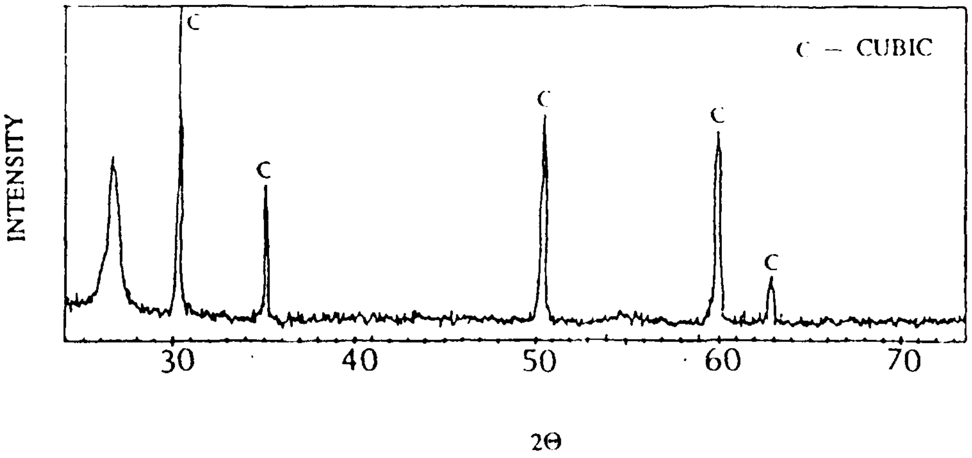

Figure 36a. X-ray diffraction pattern for the outer surface of dry-pressed $CaZrO_3$ after evaporation at 1850°C showing the zirconia solid solution cubic phase.

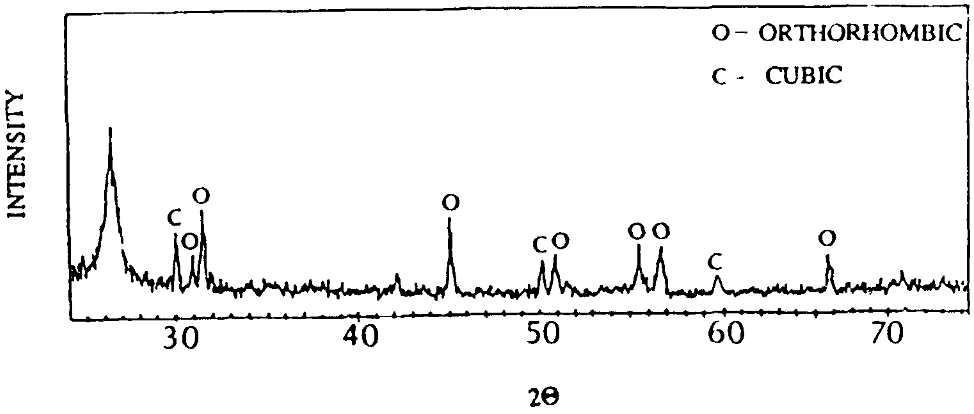

Figure 36b. X-ray diffraction pattern for the fracture surface of dry-pressed $CaZrO_3$ after evaporation at 1850°C showing peaks corresponding to both the zirconia solid solution cubic phase and the $CaZrO_3$ orthorhombic phase.

$CaZrO_3$ phases. Considering the thin cross section of the specimen, the fracture surface exposed a complete cross section to the X-rays. Some cubic solid solution component of the signal is therefore due to its presence at the surface.

A couple of experiments were also performed with hot- pressed samples of the Alfa products $CaZrO_3$. The weight loss curves for the hot-pressed sample at a temperature of 1850°C are shown in Figure 37. A comparison with the weight loss curve of dry-pressed $CaZrO_3$ at 1850°C is made in Figure 38. The hot-pressed sample is much denser than the dry-pressed sample. Normally, the weight loss per unit apparent area must be greater for the more porous dry-pressed sample. This is the reverse of our observation in Figure 38, where the weight loss for the hot-pressed sample is greater than that for the dry-pressed sample by about a factor of two. However, the impurity associated with the hot-pressed sample might be responsible for the observed discrepancy. This could be another pointer to the fact that the kinetics here are controlled by diffusion in the condensed phase. The change in diffusion coefficient, D, due to the presence of impurities in the condensed phase could lead to the anomalous weight loss behaviour exhibited by the hot-pressed sample.

The weight loss curves for hot-pressed $BaZrO_3$ at 1680, 1730 and 1780°C are shown in Figures 39, 40 and 41 respectively. There is a fairly large scatter in the data and this may be due to either the complexity of the phenomenon of microcrack formation or the possibility that the commercial powder (obtained from TAM) from which these samples were prepared contained a heterogeneous impurity distribution. In fact the EDS analysis carried out on the surface of $BaZrO_3$ samples tested at 1730°C show a considerable amount of aluminum as documented in Table 3. The EDS analysis of the outer surface of $BaZrO_3$ samples tested at 1780°C showed extremely tiny amounts of barium or aluminum indicating that both Ba and Al are subject to preferential evaporation. Figure 42 shows the master plot containing the weight loss curves of hot-pressed $BaZrO_3$ at the three different temperatures at which the experiments were performed.

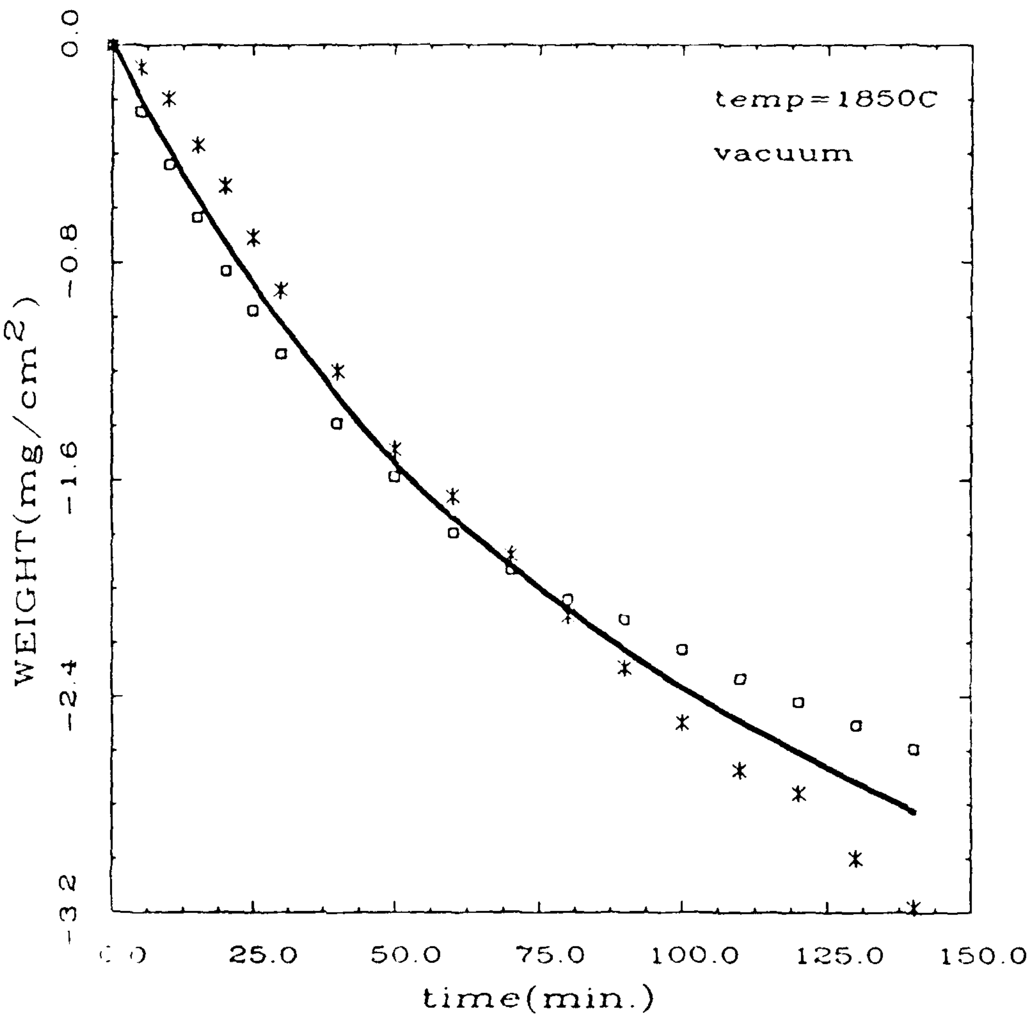

Figure 37. A plot of the measured weight loss per unit apparent projected surface area vs. time for hot-pressed $CaZrO_3$ held at 1850°C for about 2 hours in vacuum.

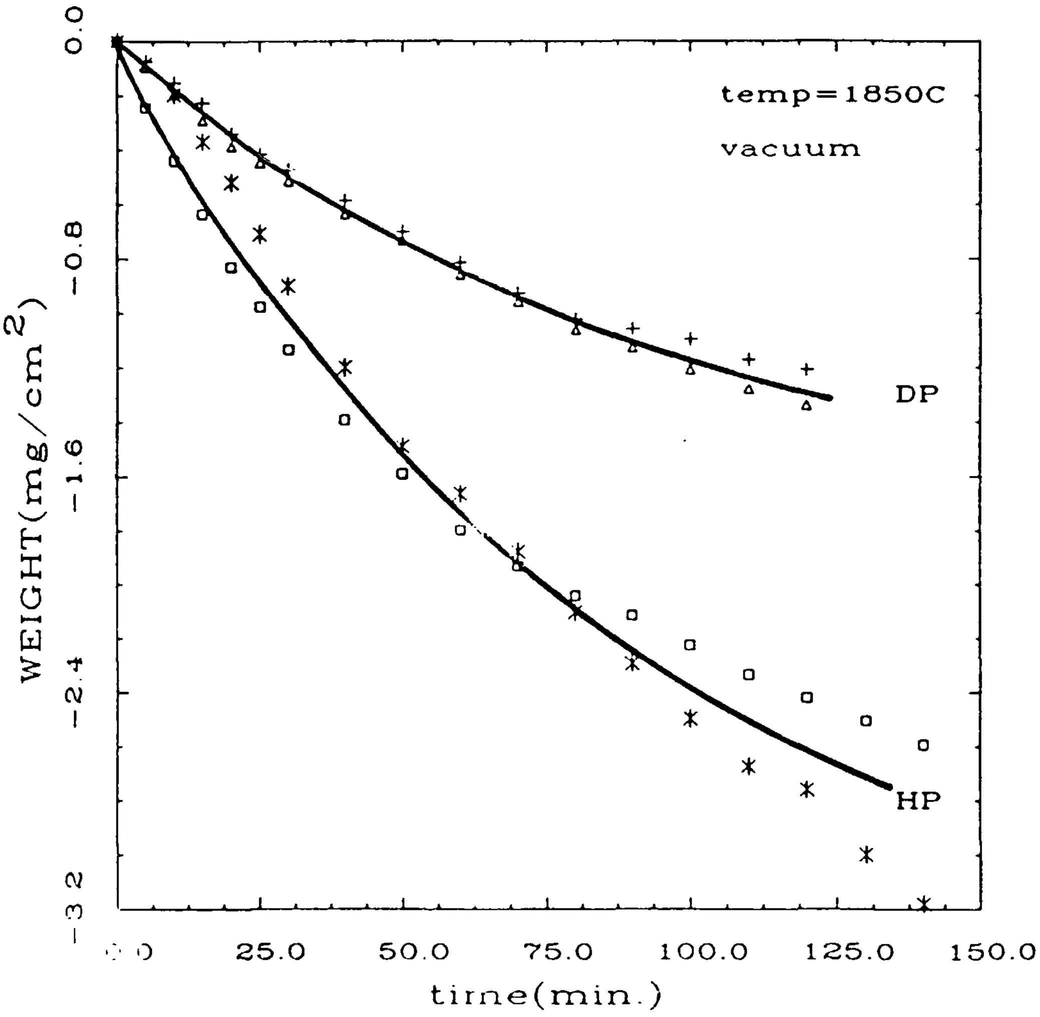

Figure 38. A plot showing the measured weight loss per unit apparent projected surface area vs. time for dry-pressed and hot-pressed $CaZrO_3$ held at 1850°C for about 2 hours in vacuum.

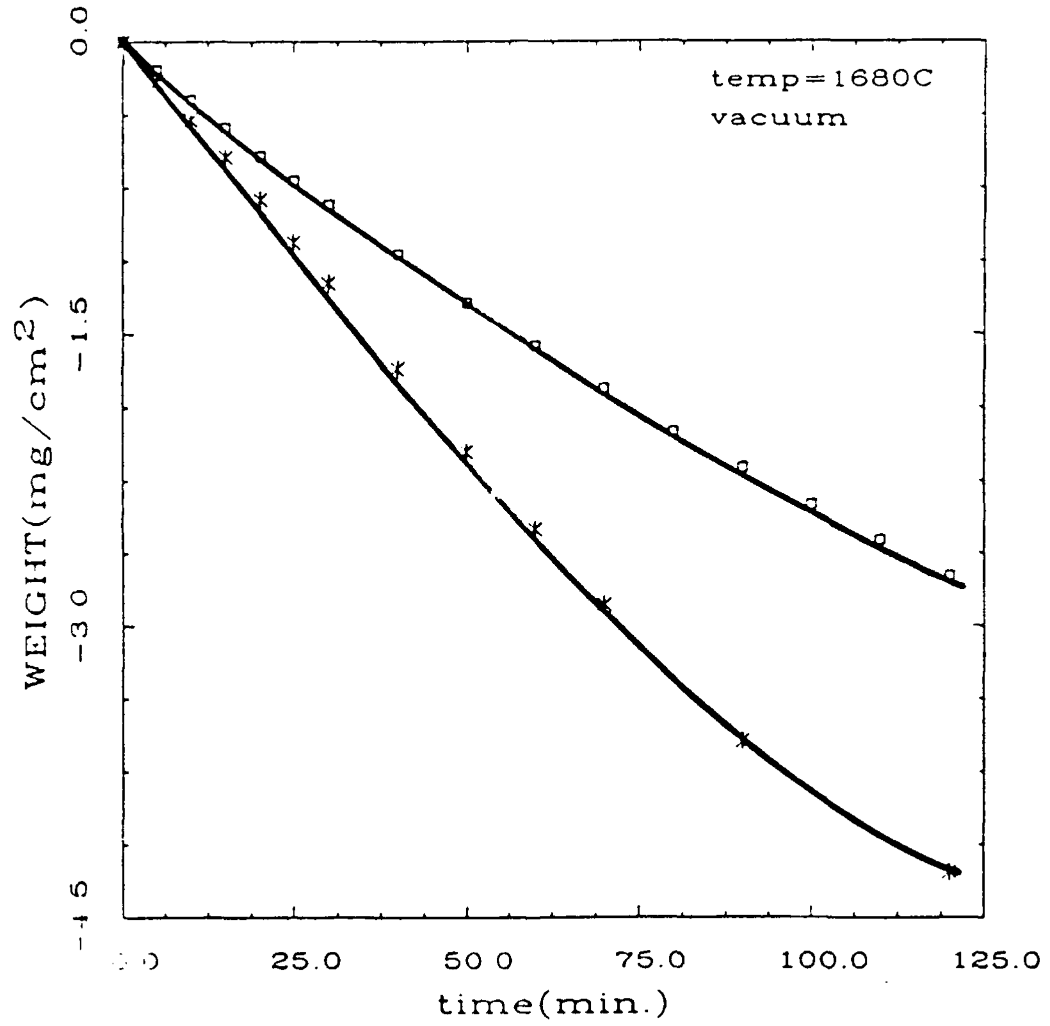

Figure 39. A plot showing the measured weight loss per unit apparent projected surface area vs. time for hot-pressed $BaZrO_3$ held at 1680°C for about 2 hours in vacuum.

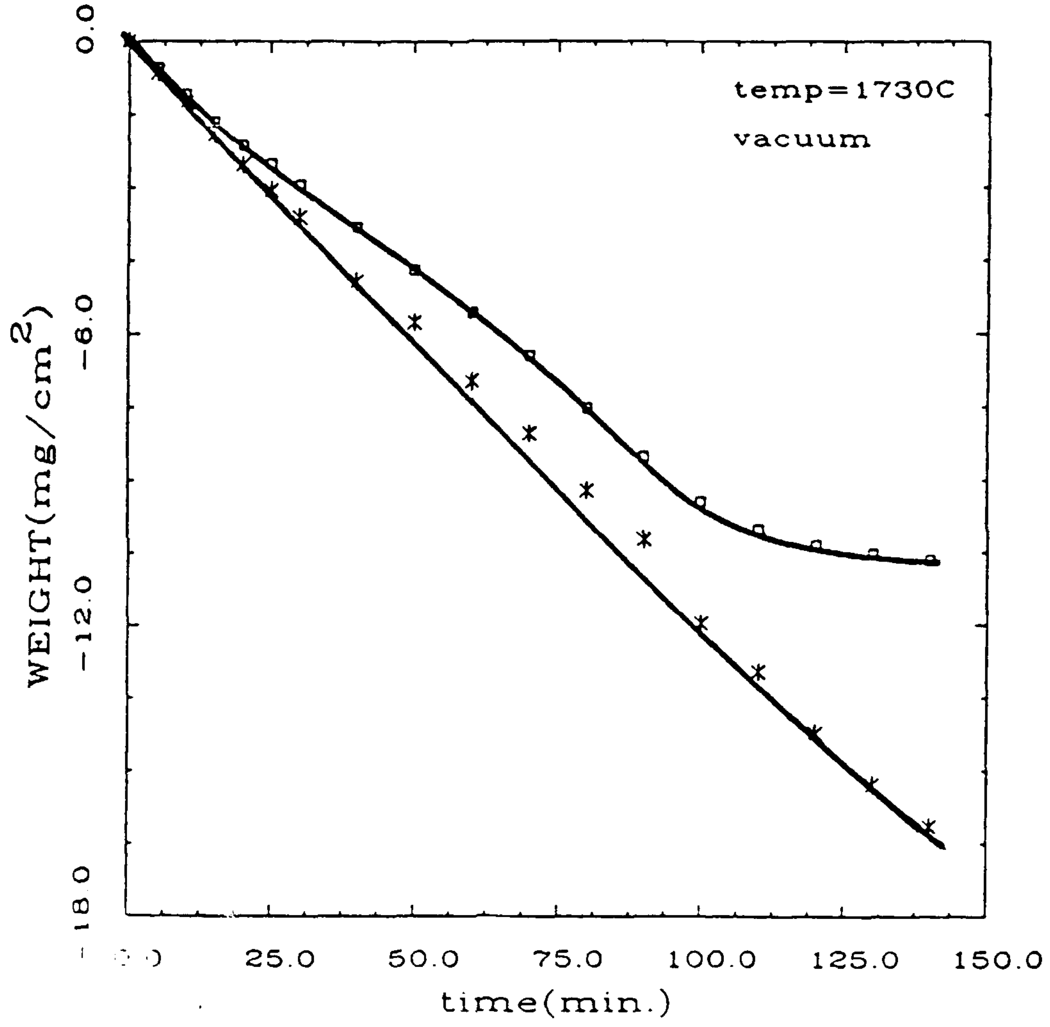

Figure 40. A plot showing the measured weight loss per unit apparent projected surface area vs. time for hot-pressed $BaZrO_3$ held at 1730°C for about 140 minutes in vacuum.

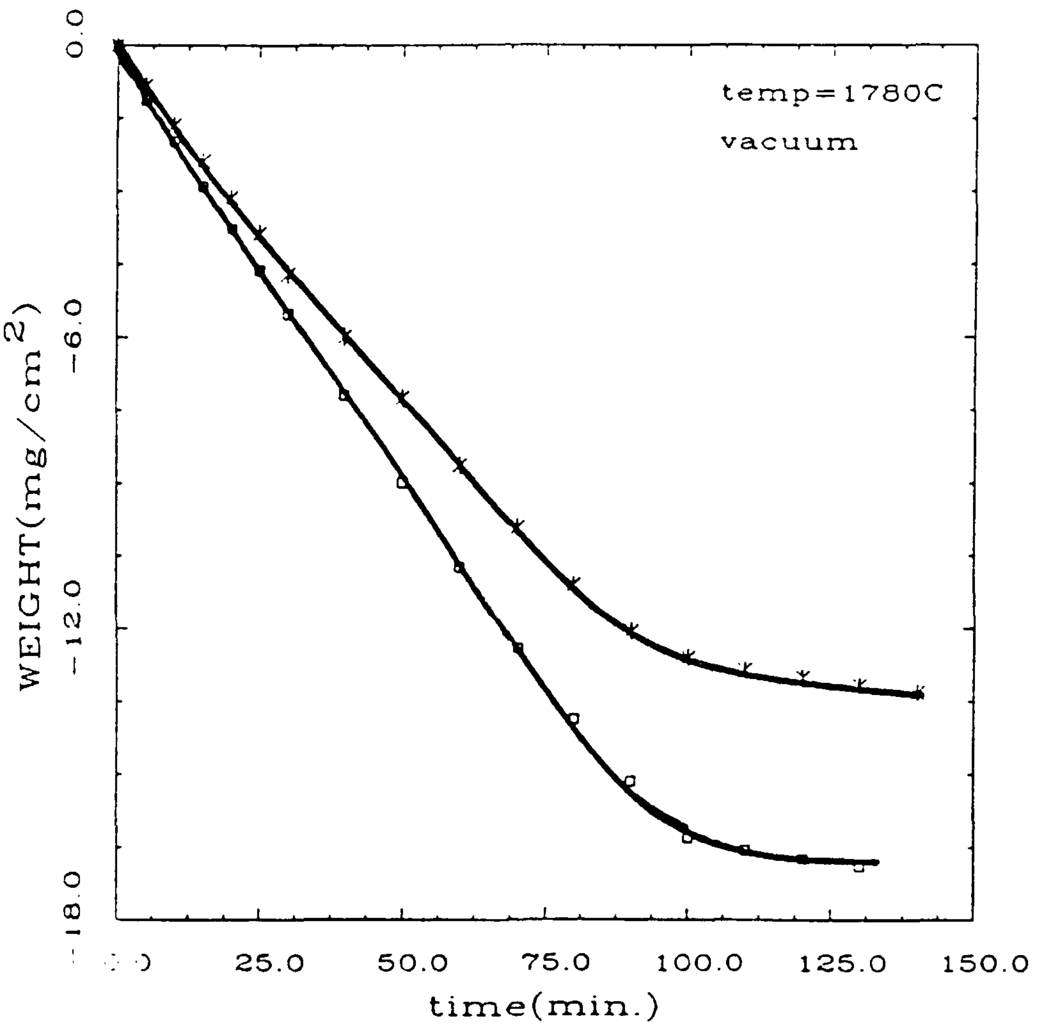

Figure 41. A plot showing the measured weight loss per unit apparent projected surface area vs. time for hot-pressed $BaZrO_3$ held at 1780°C for about 130 minutes in vacuum.

Table 3. Results of the EDS analysis carried out on the outer surface of hot-pressed $BaZrO_3$ after vaporization at 1730°C for about 140 minutes.

Atomic % Zr	Atomic % Ba	Atomic % Al
47.09	14.61	38.30
64.52	11.33	24.16
73.61	10.02	16.37

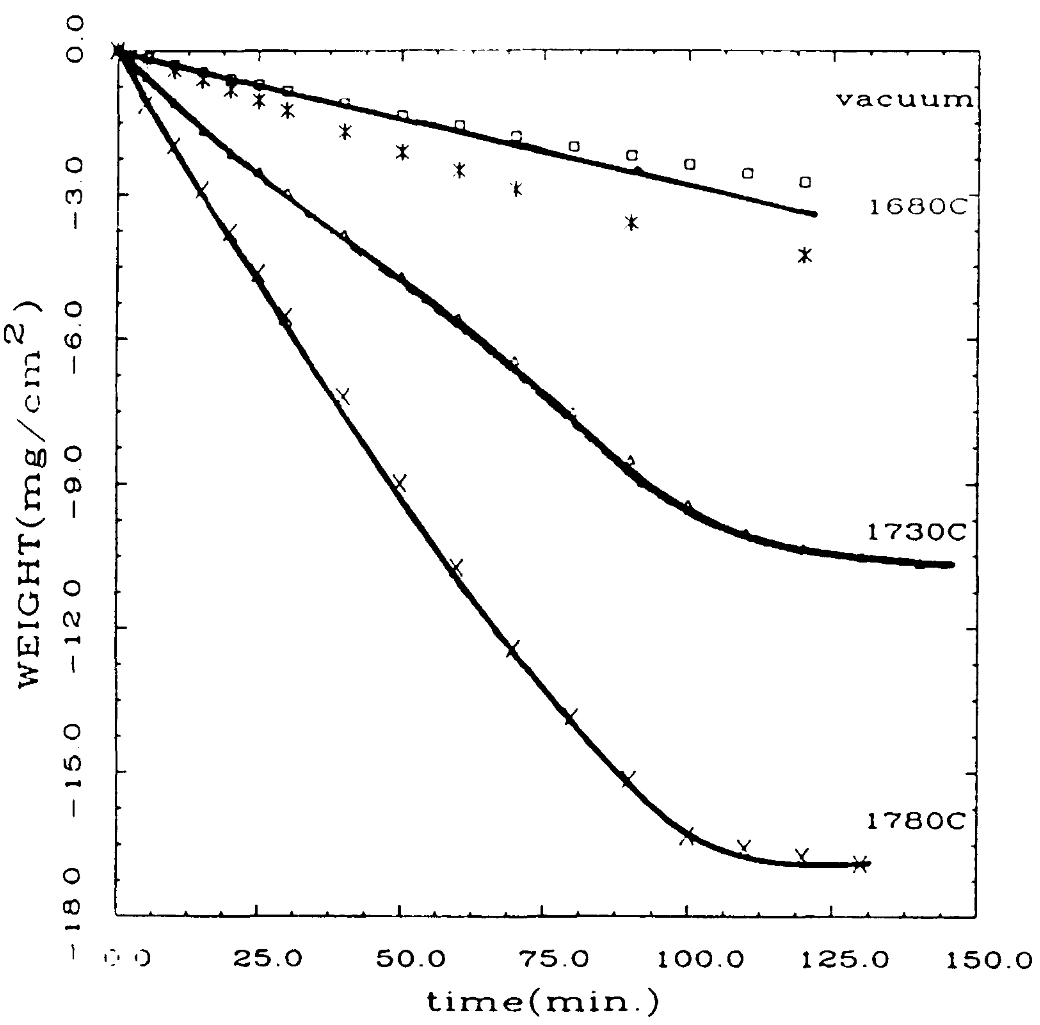

Figure 42. A plot showing the measured weight loss per unit apparent projected surface area vs. time for hot-pressed $BaZrO_3$, held at three different temperatures.

The kinetics appear fairly linear in nature although at the two higher temperatures there is a sudden change in the slope of the curve after a long time which tends to flatten out the curve. This is as yet unexplained.

The X-ray diffraction pattern of the surface of the $BaZrO_3$ samples tested at 1730°C and 1780°C are both identical and appear to contain peaks corresponding to the cubic and monoclinic phases of ZrO_2 as well as the cubic phase of $BaZrO_3$. These are shown in Figures 43a and 43b. The SEM micrograph of the fracture surface of the hot-pressed $BaZrO_3$ sample tested at 1780°C is shown in Figure 44.

From Figures 30 and 42, the logarithm of intial slopes versus the inverse of temperature (1/T) is plotted in Figure 45 for dry-pressed $CaZrO_3$ and hot-pressed $BaZrO_3$. Although the weight lost for a period of time at a given temperature cannot be predicted right away, the initial slope of the weight loss plot at any given temperature can be estimated. For instance, at 2000°C, the initial slope of the weight loss plot is 3.38 $mg/cm^2/hr$ for dry-pressed $CaZrO_3$. The recession rates for dry-pressed $CaZrO_3$ and hot-pressed $BaZrO_3$ in μ/hr are shown in Tables 4a and 4b respectively. These have been computed from the initial slopes of the weight loss curves assuming a 90% theoretical density for the dry-pressed $CaZrO_3$ and using the measured 95.8% theoretical density value for the hot-pressed $BaZrO_3$.

3.3 NRA Analysis and Tracer Profile Concentrations

The non-resonant NRA technique was used to measure diffusion coefficients for two reasons: (1) the large nuclear cross-section provided short experimental run times and (2) carbon build-up on the target was minimized with the short experimental run times. Although energy straggling of the out-going alpha particles within the material limited the depth probed using this method, the longer run times necessary for the resonant nuclear reaction technique coupled with the problem of carbon build-up made the non-resonant nuclear reaction technique more useful.

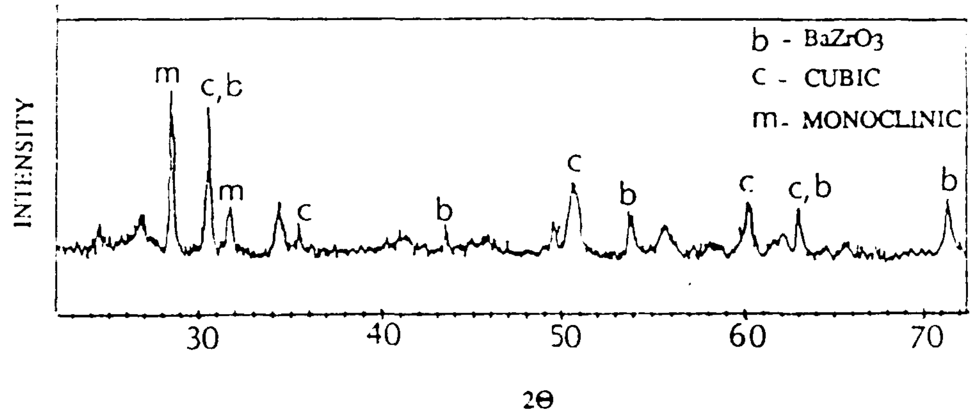

Figure 43a. X-ray diffraction pattern for the outer surface of hot-pressed $BaZrO_3$ after evaporation at 1730°C showing peaks corresponding to cubic zirconia, monoclinic zirconia and cubic $BaZrO_3$.

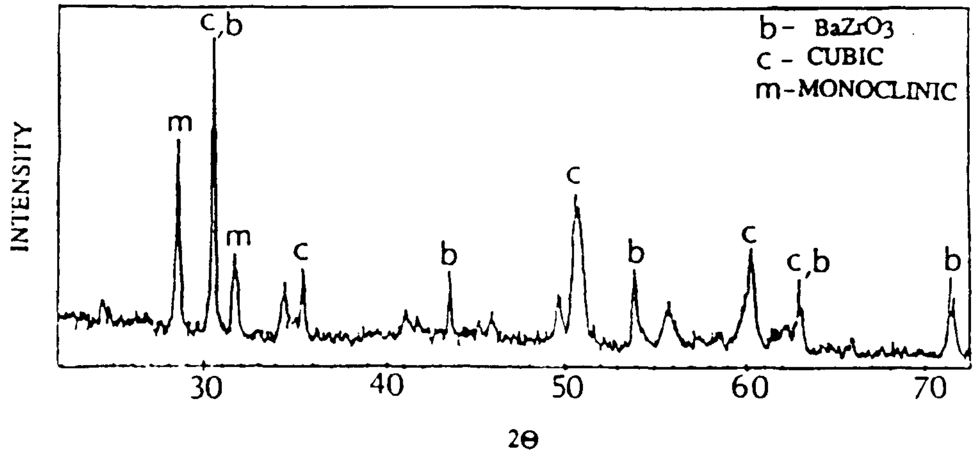

Figure 43b. X ray diffraction pattern for the outer surface of hot-pressed $BaZrO_3$ after evaporation at 1780°C showing peaks corresponding to cubic zirconia, monoclinic zirconia and cubic $BaZrO_3$.

Figure 44. A SEM image, using secondary electrons, of the fracture surface of hot-pressed $BaZrO_3$ after vaporization at 1780°C for about 2 hours, at a magnification of 2000x.

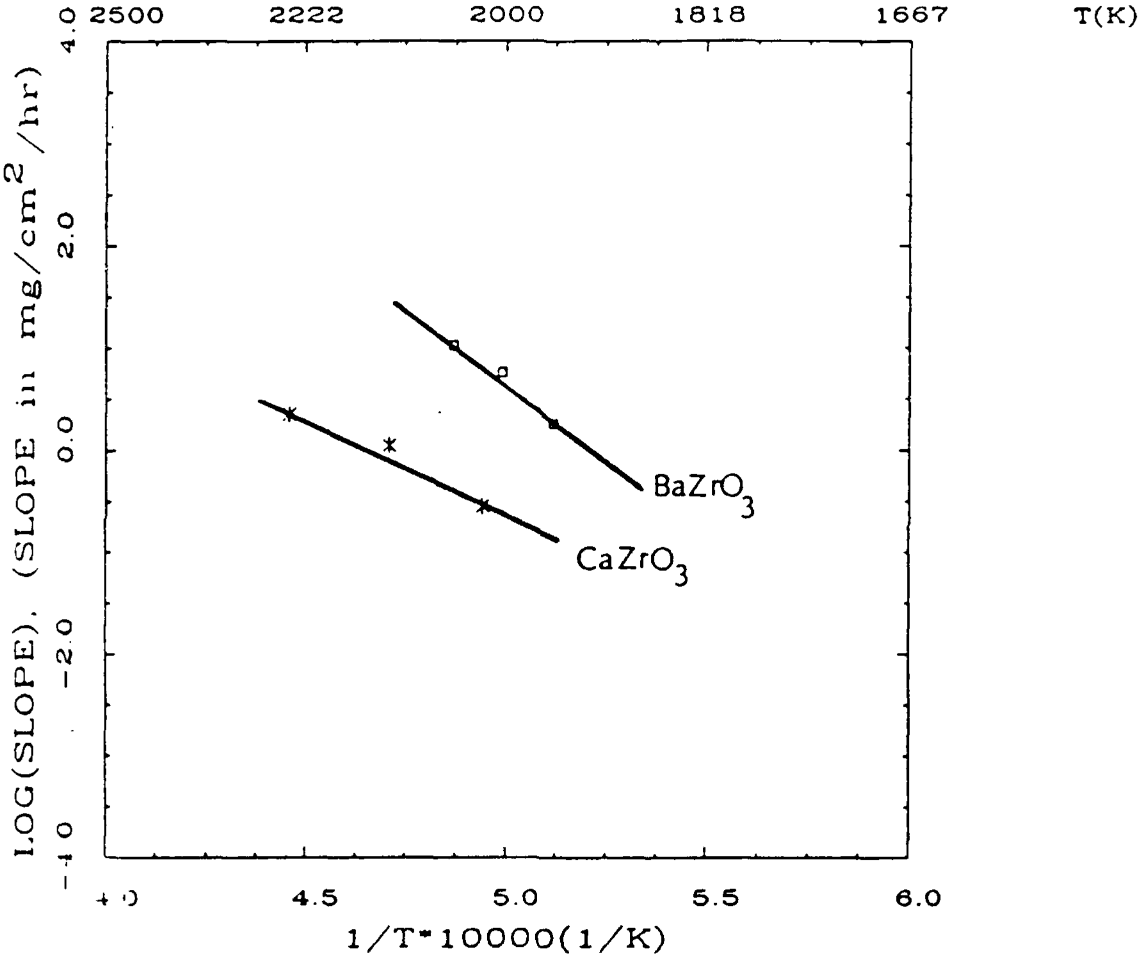

Figure 45. A plot of the logarithm of the slope of the weight loss curves for dry-pressed $CaZrO_3$ and hot-pressed $BaZrO_3$ as a function of temperature.

Table 4a. Recession rate in μ/hr for dry-pressed $CaZrO_3$.

Temperature(°C)	Recession rate (μ/hr)
1750	0.67
1850	2.65
1970	5.35

Table 4b. Recession rate in μ/hr for hot-pressed $BaZrO_3$.

Temperature(°C)	Recession rate (μ/hr)
1680	3.0
1730	9.5
1780	17.7

The theoretical tracer concentration profiles depend on the time and temperature of the anneal. Comparison of non-resonant $^{18}O(p,\alpha)^{15}N$ nuclear reactions on SiO_2 annealed at various times of 4, 16, and 24 hours in ^{18}O at 1100°C [23] after charge normalization is performed (Figure 46) shows graphically the increased tracer concentrations as the annealing time increases.

A similar comparison is shown for $CaZrO_3$ annealed at 1000°C for 12 minutes and 24 hours in Figure 47. These profiles were fitted using a sum of the solution to the diffusion equation for surface evaporation boundary condition [25] and an exponential term to account a fast diffusion path which produces a tail in the depth profiles:

$$(C-C_b)/(C_g-C_b) = \mathrm{erfc}[x/2(Dt)^{1/2}] - \exp(Kx/D + K^2t/D)\,\mathrm{erfc}[x/2(Dt)^{1/2} + K(t/D)^{1/2}] + Q\exp\text{-}(Zx^{6/5}) \qquad (3)$$

where

C = concentration of ^{18}O at depth x

C_g = concentration of ^{18}O in the gas phase

C_b = background concentration of ^{18}O in the solid phase

D = diffusion coefficient

t = time of the diffusion anneal

K = first order surface exchange coefficient

and Q, Z = fitting parameters.

If the fast-diffusion paths are grain boundaries, the product of the grain boundary diffusion coefficient, D_{gb}, and the grain boundary width, δ, is given by [26]

$$D_{gb}\,\delta = 0.66Z^{-5/3}(4/Dt)^{1/2} \qquad (4)$$

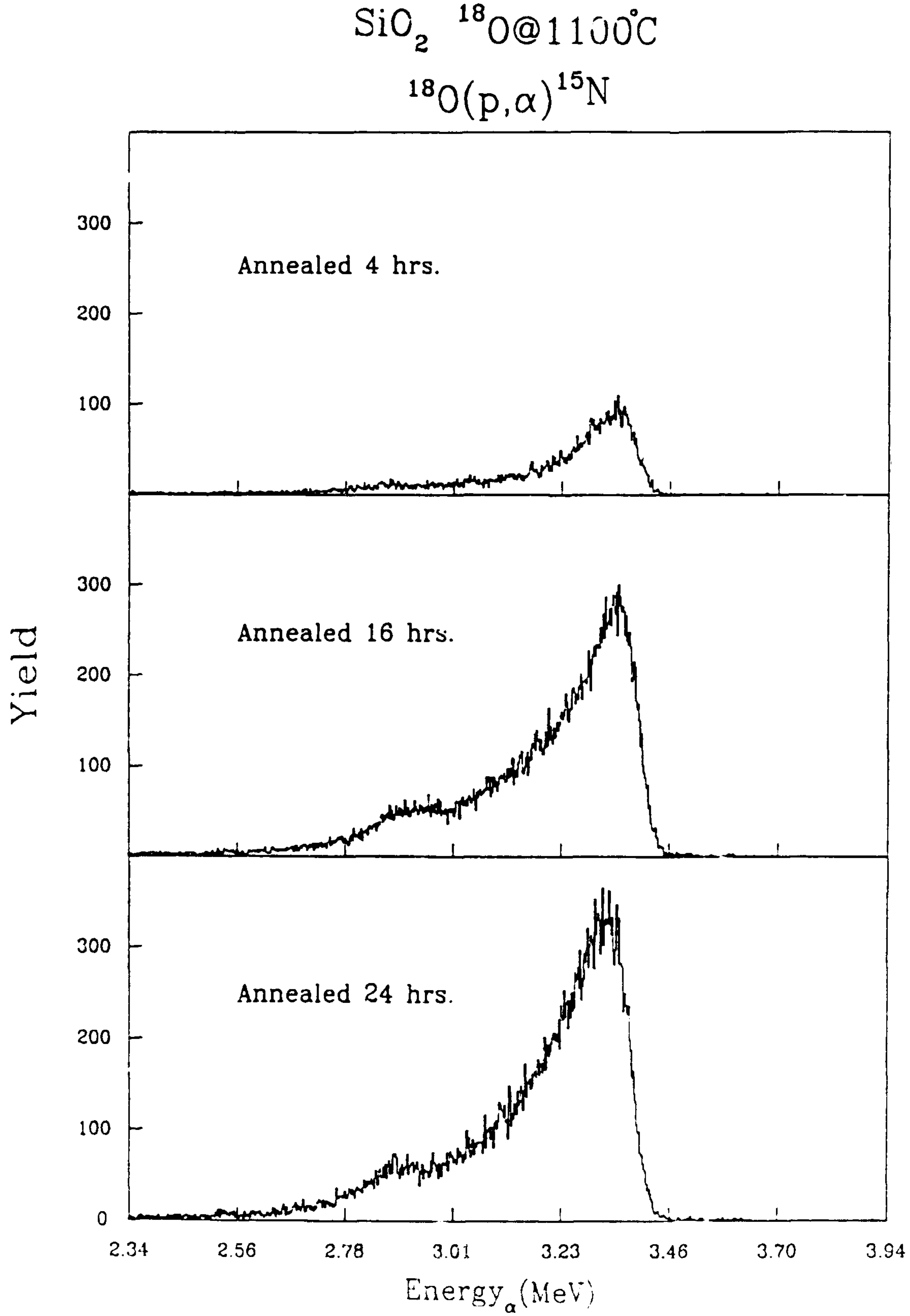

Figure 46. Effect of increased annealing times on the depth profile.

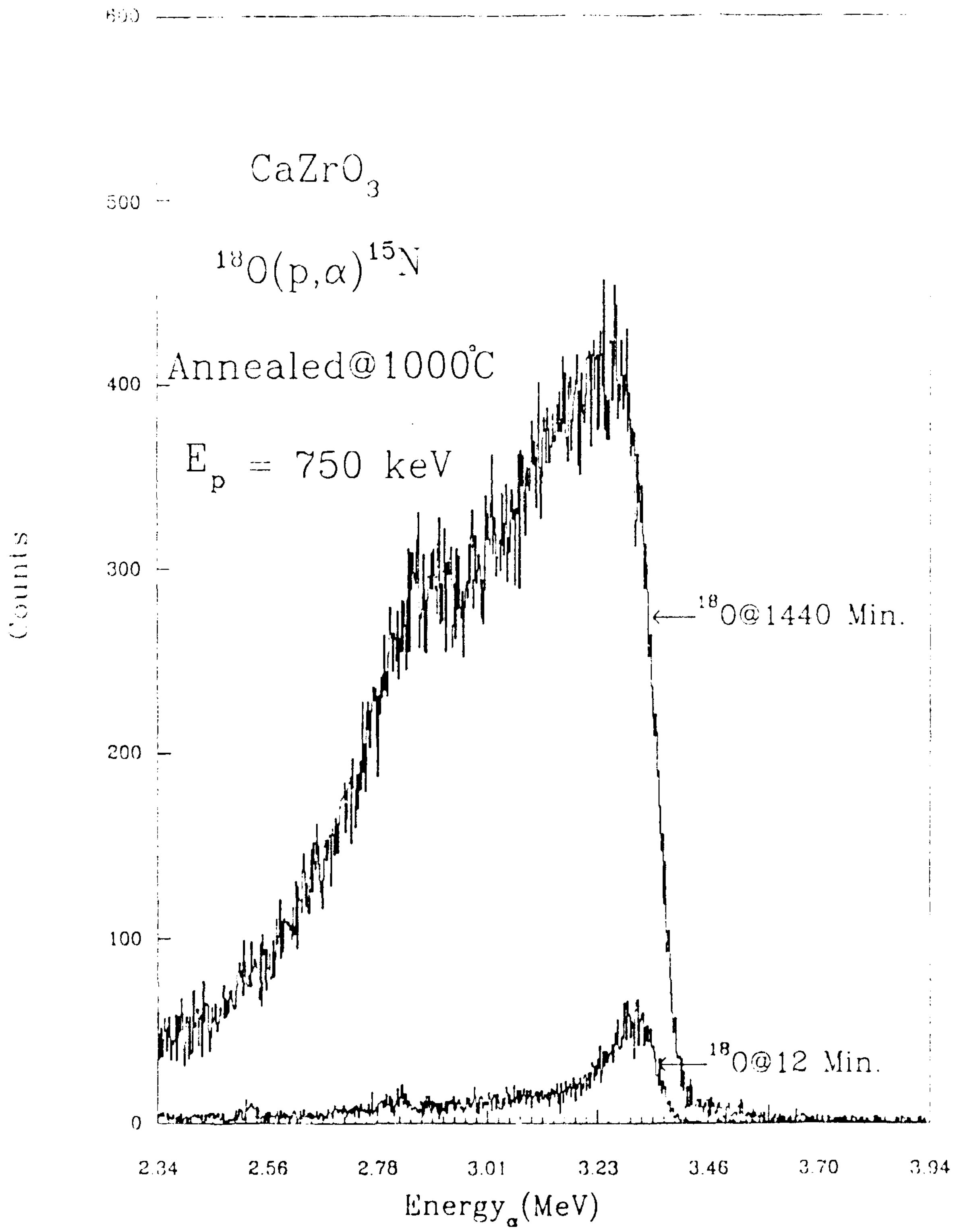

Figure 17. Normalized spectra of CaZrO$_3$ annealed at 12 minutes and 24 hours (1440 minutes) at 1000°C.

Because of the small tracer penetration in the $CaZrO_3$ sample annealed for 12 minutes relative to the spreading coefficients inherent in this technique, the NRA spectra could be fitted equally well with two sets of diffusion constants: $D = 5.2\times10^{-13}$ cm^2/sec and $K = 2.0\times10^{-9}$ cm/sec; or $D = 3.7\times10^{-15}$ cm^2/sec and $K = \infty$. Note that in the second case the second term in Equation (3) which accounts for the surface exchange reaction is equal to zero. For the first case, finite K, the normalized surface concentration is calculated to be 0.12, while it must be equal to 1 if K is regarded as infinite.

These values represent the upper and lower limits of the diffusion coefficient at 1000°C. One would therefore expect the diffusion coefficient obtained from fitting the spectra obtained from a longer diffusion anneal to be within this range. For the $CaZrO_3$ sample exchanged for 24 hours at 1000°C, a diffusion coefficient of 2.7×10^{-12} cm^2/sec was obtained which is about six times higher than the D value obtained for the 12-minute depth profile using a surface exchange term. Observation of the microstructure, however, reveal the presence of a large number of pores in the sample exchanged for 24 hours which was not seen in the sample exchanged for 12 minutes. This microstructural difference could account for the higher D obtained for the sample which was annealed longer.

Figure 48 shows differences in tracer concentration for $BaZrO_3$, $CaZrO_3$, and $SrZrO_3$ samples, all annealed at 1000°C for 24 hours. This graphically indicates that the penetration depth is largest for $CaZrO_3$ and smallest for $BaZrO_3$.

A plot of the concentration profiles using apparent tracer diffusion coefficients obtained by fitting the above experimental depth profiles is shown in Figure 49. The concentration profile for $BaZrO_3$ goes down to the background within 5 microns whereas those of $CaZrO_3$ and $SrZrO_3$ do not indicating deep diffusion into the material. Both spectra for $CaZrO_3$ and $SrZrO_3$ could be fit with Equation (3) which is the sum of a distance dependent term representing bulk diffusion and an invariant term representing grain boundary diffusion. The $BaZrO_3$ spectra, however, could be fit with only the

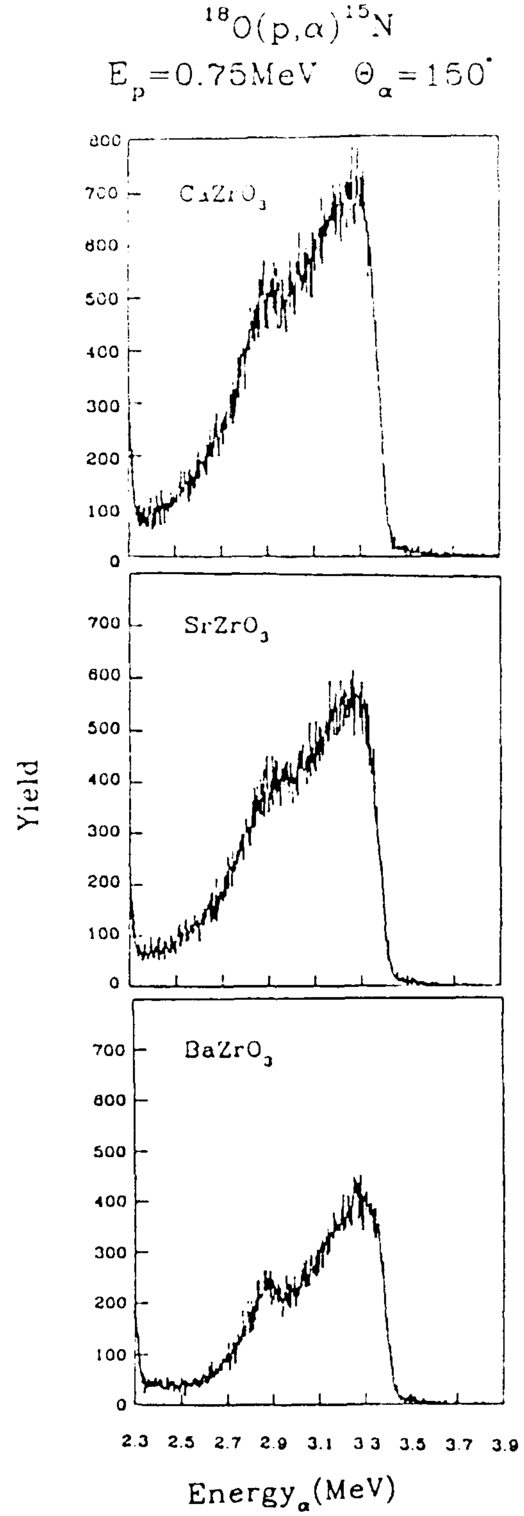

Figure 48. Non-resonant experimental spectra, after charge normalization, of the alkaline-earth zirconates diffusion-annealed at 1000°C for 24 hours.

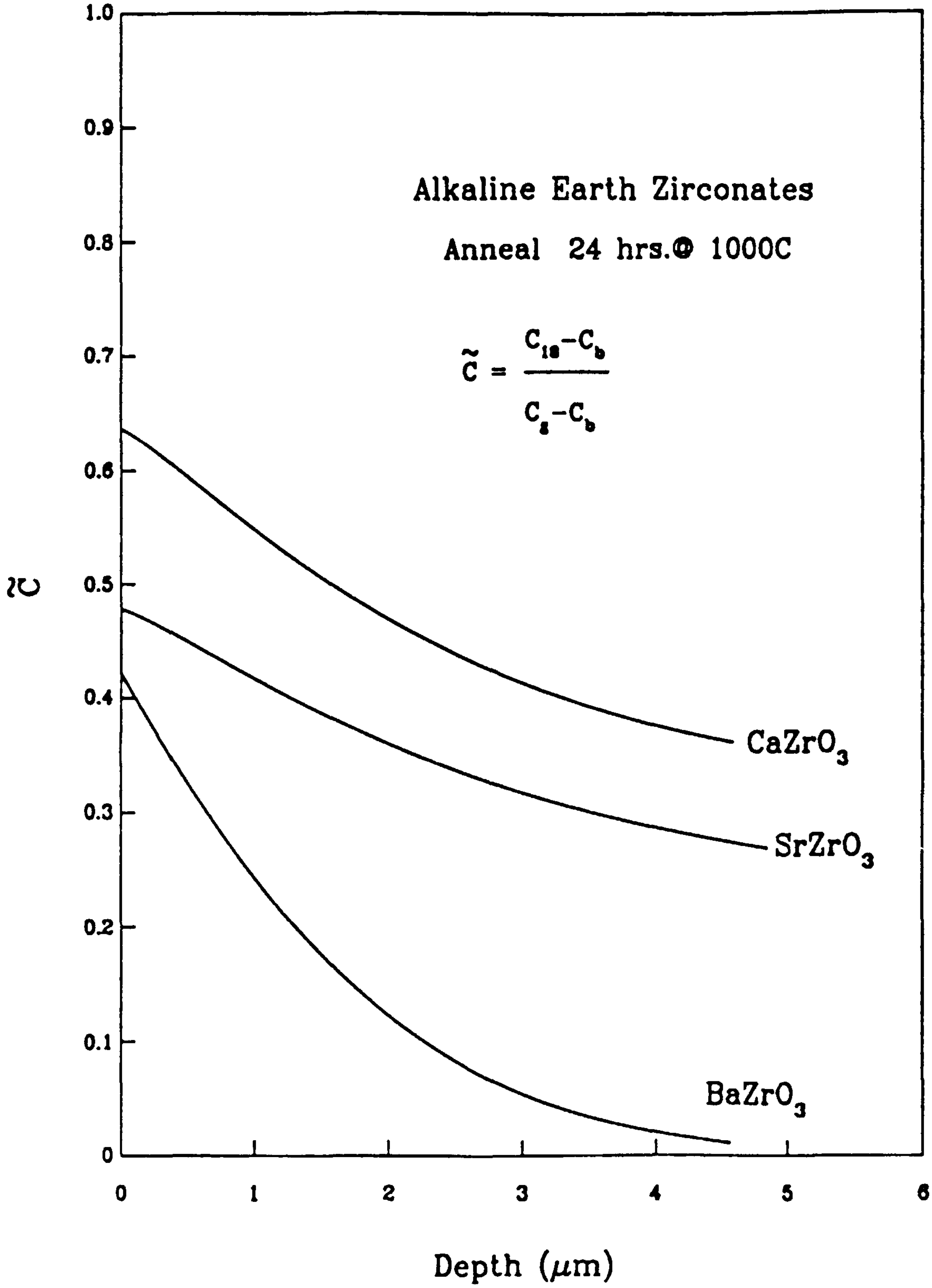

Figure 49. A plot of the concentration profiles using apparent tracer diffusion coefficients obtained by fitting the experimental spectra shown in Figure 48.

bulk diffusion term. This cannot be explained considering that the average grain size of 0.6 microns for $BaZrO_3$ is much less than the average grain size of 12 microns for $CaZrO_3$ and 5 microns for $SrZrO_3$. The only other microstructural difference is the presence of porosity in the $CaZrO_3$ and $SrZrO_3$ samples and its absence in the $BaZrO_3$ samples. This difference could account for the deeper penetration in $CaZrO_3$ and $SrZrO_3$ than in $BaZrO_3$ by (a) providing short circuit diffusion paths or (b) creating a rough surface which would result in an apparent deep profile.

Figure 50 shows an Arrhenius plot of the results obtained for the alkaline-earth zirconates together with literature values of the oxygen diffusion coefficients for other oxides. The apparent oxygen diffusivity for $CaZrO_3$ is about 5 orders of magnitude lower than in calcia stabilized zirconia at 1000°C. A linear fit of the experimental points for $BaZrO_3$ gives an apparent oxygen tracer diffusion coefficient of

$$D = 5.0 \times 10^{-3}\ \mathrm{cm^2/sec}\ \exp(-247\ \mathrm{KJ/mole} / RT)$$

in the temperature range of 900° - 1100°C. Using this equation, the extrapolated diffusion coefficient for $BaZrO_3$ is 3.0×10^{-9} $\mathrm{cm^2/sec}$ at 1800°C and 3.0×10^{-8} $\mathrm{cm^2/sec}$ at 2200°C. These values are within an order of magnitude of the oxygen tracer diffusion coefficients for the isostructural $SrHfO_3$ determined at the temperature range of 1800° - 2200°C [27]. The apparent oxygen tracer diffusion coefficients for the alkaline-earth zirconates are summarized in Table 5.

4. CONCLUSION

In summary, dry-pressed $CaZrO_3$ and hot-pressed $BaZrO_3$ have been tested at three different temperatures each to study their vaporization characteristics. The materials have been characterized using the SEM, EDS and X-ray diffraction techniques.

Both $CaZrO_3$ and $BaZrO_3$ appear to have a fairly high rate of evaporation at high temperatures. However, dry-pressed $CaZrO_3$ shows a smaller rate of evaporation than

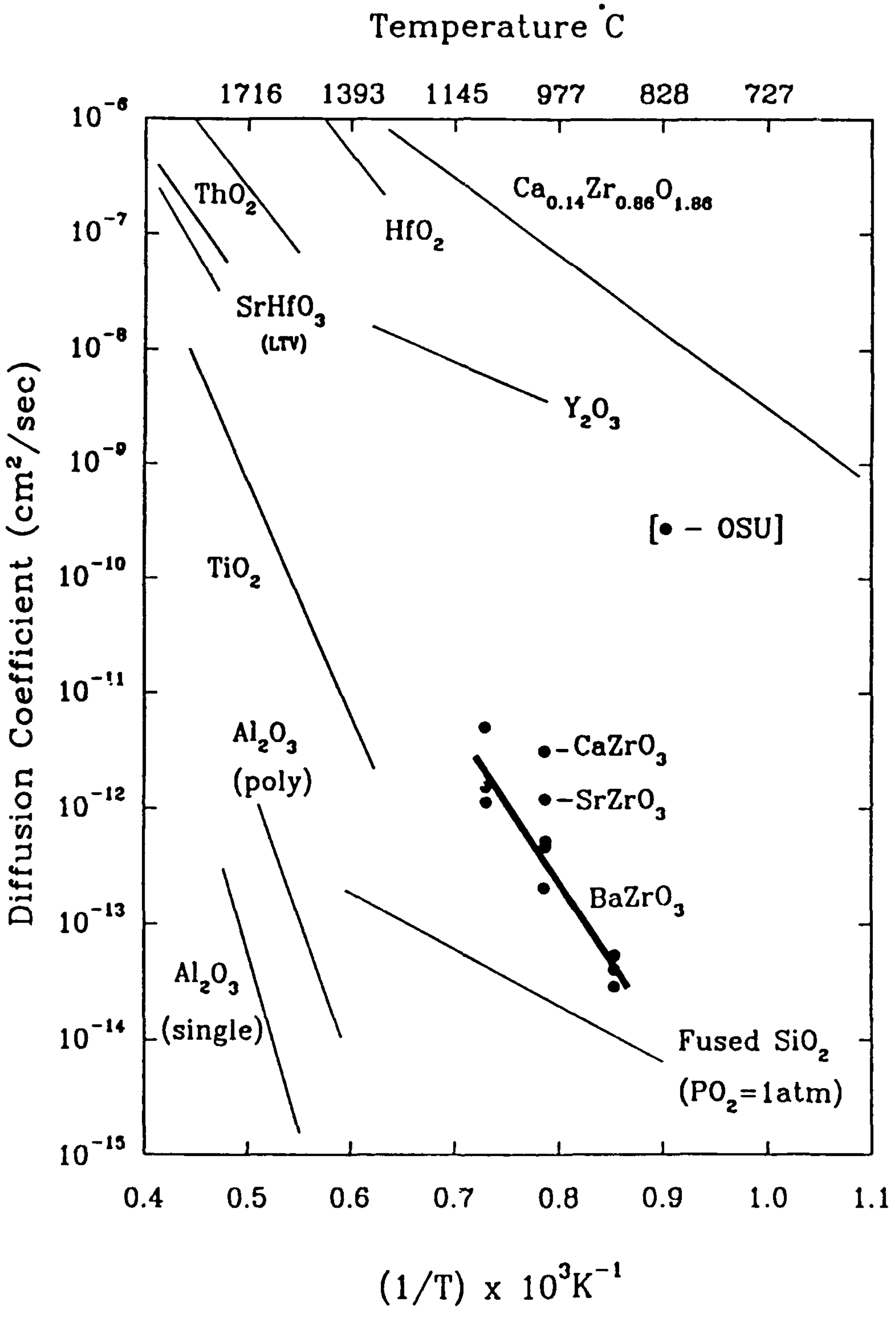

Figure 50. Arrhenius plot of the apparent tracer diffusion coefficients for the alkaline-earth zirconates together with literature values of oxygen diffusivities in other oxides.

Table 5. Apparent oxygen tracer diffusion coefficients measured for the alkaline-earth zirconates.

Material	Temperature (°C)	Time (hrs)	D (cm^2/sec)
$CaZrO_3$	1000	24	2.7×10^{-12}
$SrZrO_3$	1000	24	1.1×10^{-12}
$BaZrO_3$	900	24	3.7×10^{-14}
$BaZrO_3$	900	48	5.0×10^{-14}
$BaZrO_3$	900	72	2.6×10^{-14}
$BaZrO_3$	1000	8	4.4×10^{-13}
$BaZrO_3$	1000	16	4.8×10^{-13}
$BaZrO_3$	1000	24	3.0×10^{-13}
$BaZrO_3$	1100	2	4.6×10^{-12}
$BaZrO_3$	1100	4	1.5×10^{-12}
$BaZrO_3$	1100	8	1.0×10^{-12}

hot-pressed $BaZrO_3$. In both the materials, solid state diffusion appears to play a key role in the kinetics of vaporization.

Results of the diffusion experiments indicate that $CaZrO_3$ exhibits the largest penetration with $BaZrO_3$ showing the smallest. Apparent oxygen tracer diffusion coefficients were measured for $CaZrO_3$ and $SrZrO_3$ at 1000°C and for $BaZrO_3$ the apparent oxygen tracer diffusion coefficient is calculated to be

$$D = 5.0 \times 10^{-3}\ \mathrm{cm^2/sec}\ \exp(-247\ \mathrm{KJ/mole} / RT)$$

in the temperature range of 900° - 1100°C.

REFERENCES

1. J. L. Margrave, ed., "The Characterization of High Temperature Vapors" (John Wiley and Sons Inc., 1967).

2. D. S. Rutman, I. L. Shchetnikova, T. S. Ignatova and G.A. Semenov, "Volatilization of Components from Zirconia Ceramics," Refractories, 1, 52-54 (1968).

3. W. D. Kingery et. al.,"Oxygen Ion Mobility in Cubic $Zr_{0.85}Ca_{0.15}O_{1.85}$," Journal of the American Ceramic, 42, 393 (1959).

4. R. Freer, "Bibliography, Self-Diffusion and Impurity Diffusion in Oxides," J. Mat. Sci., 13, 803-824 (1980).

5. J. Doskocil and Z. Pospicil, Silikaty, 16 [2], 113-123 (1972).

6. A. Yamaji, "Oxygen-Ion Diffusion in Single-Crystal and Polycrystalline $SrTiO_3$," J. Amer. Cer. Soc., 58, 152-153 (1975).

7. J. D. Cawley, "Oxygen Diffusion in Alpha Alumina" Ph.D Thesis, Case Western Reserve University (1984).

8. T. Okubo et al, "Synthesis of $SrZrO_3$, $CaZrO_3$, $BaZrO_3$ from Powders," Nagoya Kogyo Gijutsu Shikensho Hokoku, 24, 271-277 (1975).

9. John. F. Elliott, "Radiation Pyrometry," Thermochemistry for Steelmaking, 2, 721-722 (1980).

10. F. Turner, "Cryosorption Pumping," Varian Vacuum Division 11th Annual Vacuum Technology Seminar, 9 (1973).

11. R. S. Boyce, "The Mechanisms Of Oxygen Transport In Vitreous Silica" M.S Thesis, Ohio State University (1986).

12. J. F. Cummings, "Depth Profiling Of Oxygen In Silicon Using Ion Beams" M.S Thesis, Ohio State University (1986).

13. T. Rinckel, "Acquisition Code For Research On Nuclei," program developed at Ohio State University (1985).

14. G. Amsel and D. Samuel, Anal. Chem. 39, 1689 (1967).

15. H. H. Anderson and J. F. Ziegler, "Proton: Stopping Powers and Ranges in All Elements" (Pergamon Press, New York, 1977).

16. J. F. Ziegler, "Helium: Stopping Powers and Ranges in All Elements" (Pergamon Press, New York, 1977).

17. A. Abduljalil and J. D. Kalen, "LINE," program developed at Ohio State University (1988).

18. J. D. Kalen, "DC," program developed at Ohio State University (1988).

19. G. Deconninck and B. Van Oystaeyen, "High Resolution Depth Profiling of F, Ne, and Na in Materials," Nucl. Instr. and Meths., 218, 165-170 (1983).

20. T. Rinckel, "ERRFIT," program developed at Ohio State University (1986).

21. G. Amsel and B. Maurel, "High Resolution Techniques for Nuclear Reaction Narrow Resonance Width Measurements and for Shallow Depth Profiling," Nucl. Instr. and Meths., 218, 183-196 (1983).

22. M. Wiescher et al, "Nuclear and Astrophysical Aspects of $^{18}O(p, \gamma)^{19}F$," Nuclear Physics, A349, 165-216 (1980).

23. I. Glatter, M.S. Thesis, Ohio State University (1988).

24. J. Tanabe, K. Nagata and K. S. Goto, private communications, July 1989.

25. J. Crank, "The Mathematics of Diffusion," (Clarendon Press, 1975).

26. A. D. Le Claire, "The Analysis of Grain Boundary Diffusion Measurements," Brit. J. Appl. Phys., 14, 351-356 (1963).

27. D. Freitag, "Oxygen Diffusion in $SrHfO_3$ for Use in Ceramic Matrix Composites at Ultrahigh Temperatures," Materials Laboratory Report WRDC-TR-89-4029, Wright-Patterson Air Force Base, Ohio, May 1989.

APPENDIX A
POWDER PREPARATION FOR DIFFUSION SAMPLES

Because of the impurities present in the commercial zirconate powders, solid state synthesis was used to prepare powders for diffusion samples. The starting powders used were ultrapure alkaline-earth carbonates from Johnson Matthey Chemicals Limited and zirconia from Toyo Soda. The chemical analyses of the powders used are shown below:

Material	Supplier	Major Impurities (ppm) *
$BaCO_3$	Johnson Matthey	Ca(5), Fe(1), Sr(1), Cu(<1), Mg(<1) Mn(<1), Ag(<1), Na(<1)
$CaCO_3$	Johnson Matthey	Sr(20), Mg(5), Fe(3), Na(1)
$SrCO_3$	Johnson Matthey	Ba(20), Fe(2), Na(2), Ca(<1), Mg(<1), Mn(<1)
ZrO_2	Toyo Soda	Al(30), Si(10), Fe(30), Na(50).

*supplied by Manufacturer

The alkaline earth carbonates were characterized using thermal gravimetric analysis (TGA), X-ray diffraction (XRD), and scanning electon microscopy (SEM). The TGA weight vs. temperature plots showed no water of hydration present in the samples, i.e., the only weight loss observed was due to CO_2 evolution. No second phases were detected using X-ray diffraction analysis and SEM micrographs showed that, with the exception of $CaCO_3$, the carbonates and zirconia have grain sizes less than 2 microns. The grain size of $CaCO_3$ was about 20 microns. This was reduced to less than 5 micorns by milling for 8 hours in acetone using zirconia grinding media.

Preliminary samples of $SrZrO_3$ and $BaZrO_3$ powders were made by ball milling equimolar mixtures of the carbonate and zirconia in acetone for 8 hours. Samples dry-pressed at 1 MPa were then calcined at 1200°C for 5 hours in a platinum crucible. X-ray diffraction analyses of these calcined powders showed single phase $SrZrO_3$ and $BaZrO_3$.

The resulting zirconate powders were ball milled for 5 hours to break up agglomerates. These powders were hot pressed for 1 hour at 1400°C and 3000 psi and then reoxidized in air for 24 hours at 1000°C.

Both the $SrZrO_3$ and $BaZrO_3$ samples were mechanical weak, i.e., both the hot-pressed zirconates could be easily broken by hand. In preparing bigger batches of the alkaline-earth zirconates, several measures were taken to increase the mechanical strength of the samples as discussed below.

Approximately 200 grams each of $BaZrO_3$, $CaZrO_3$ and $SrZrO_3$ were prepared in one batch. Stoichiometric amounts of the alkaline-earth carbonates and zirconia were ball milled in ethyl alcohol for 24 hours, dried, and then compacted in a platinum crucible. The $BaCO_3$ and ZrO_2 powder mixture as well as that of the $CaCO_3$ and ZrO_2 was calcined at 1400°C for 1 hour. For the $SrCO_3$ and ZrO_2 powder mixture, calcination was performed at a lower temperature of 1200°C but for a longer time of 5 hours. The calcined powders were then ball milled in ethyl alcohol for 48 hours using zirconia grinding media. Calcination of the powders followed by ball milling was done twice to ensure complete reaction of the starting powders. X-ray diffraction analyses of the calcined powders showed single phase zirconates.

The zirconate powders obtained were examined under the SEM and showed submicron-sized particles except for a few particles and hard agglomerates which were about 5 microns in size. Because of the possible deleterious effects of these 5-micron agglomerates during sintering, sedimentation was done for 70 hours after which the top 2 liters was decanted off and then dried. SEM micrographs of these powders showed that all particles were less than 1 micron in size.

Hotpressing:

1. $BaZrO_3$

The $BaZrO_3$ powder obtained was hot pressed at 1400°C and 3000 psi for 1 hour and at 1500°C and 5000 psi for 1-1/2 hours. The higher temperature, 1500°C, was used for part of the powder obtained because the 1400°C sample was weaker than samples hot pressed at the same temperature but using a less pure commercial (TAM) powder. The sintering time at 1500°C was determined from the LVDT reading which showed no change in displacement after 1-1/2 hours.

Although the 1400°C sample was mechanically weaker than the hot-pressed commercial powder, this sample was mechanically stronger than the preliminary sample prepared from powders which were not separated by sedimentation. However, the 1400°C and 1500°C samples still were both weaker than the sample using the commercial powder.

The hot-pressed $BaZrO_3$ was reoxidized in air and then cut into 1/4 inch x1/4 inch square samples. These samples were polished with 6, 3, 1 and 1/4 micron diamond pastes from which one sample was thermaly etched at 1400°C for 1 hour. SEM analysis of the thermally etched sample showed porosity. Since the sample was not dense enough for diffusion studies, no diffusion anneals were made on these samples.

2. $CaZrO_3$

As for the $CaZrO_3$ sample, two samples were hot pressed both at 1500°C and 5000 psi for 1 hour. A SEM micrograph of the $CaZrO_3$ sample etched at 1200°C for 5 hours was taken and showed that the grain size is in the order of 10 microns with porosity present within the grains and in the grain boundaries. This sample was also

AD-A256 191 THERMODYNAMIC AND DIFFUSIVITY MEASUREMENTS IN POTENTIAL 2/2
ULTRA HIGH TEMPERATURE COMPOSITE MATERIALS(U) OHIO
STATE UNIV RESEARCH FOUNDATION COLUMBUS
UNCLASSIFIED J D CAWLEY ET AL. AUG 90 WRDC-TR-90-4058 NL

END
FILMED
DTIC

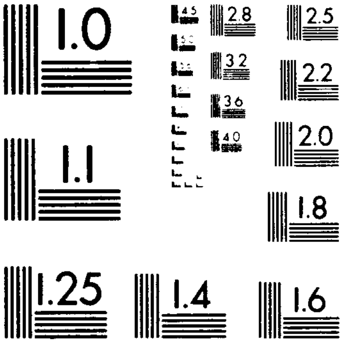
1.0
4.5
2.8
2.5
3.2
2.2
3.6
4.0
2.0
1.1
1.8
1.25
1.4
1.6

mechanically weaker than the sample prepared form the commercial powder. A higher hotpressing temperature is probably needed to fully densify the $CaZrO_3$ powders obtained by solid state reaction. Again, no diffusion anneals were made on these samples.

3. $SrZrO_3$

The $SrZrO_3$ powder was hot pressed at 1500°C and 5000 psi using a 25 gram sample for 1 hour and a 20 gram sample for 1 hour 20 minutes. The hot pressing time was determined from the LVDT reading; when no change in displacement was observed for 10 minutes, hot pressing was stopped.

The hot-pressed $SrZrO_3$ samples were cut and reoxidized in air at 1000°C for 24 hours. The sample turned out reddish and translucent after reoxidizing in air indicating very little porosity in the sample. A micrograph of an etched sample was taken which showed a grain size in the order of half a micron. Density measurements using the multivolume pycnometer showed 100% theoretical density.

A sample of the translucent strontium zirconate was sent to Coors Analytical Laboratory for spectrographic analysis. The major impurity content of the synthesized sample is compared below with sol-gel derived powder from Universal Energy Systems (UES):

Impurities	UES (ppm)	Synthesized (ppm)
Fe	200	50
Al	200	300
Si	500	50
Ti	50	<10
Mg	3000	100
Ba	100	100
Mn	3000	<10
Ga	1000	<50
Na	300	50
Ca	500	300

Except for aluminum, the impurity level in the solid state synthesized powder is lower than the sol-gel derived powder. Because the $SrZrO_3$ samples were fully densified, diffusion anneal will be performed on these samples.

APPENDIX B

COMPUTER PROGRAM dE/dX USED FOR FITTING ALPHA AND PROTON STOPPING POWERS

```
        INCLUDE 'STEPTCOM.FOR'
        COMMON Y(500),E(500),DY(500),NPTS,FUNKY(500)
        COMMON NQ(500)
        DIMENSION XINITIAL(20)
        CHARACTER*60 NAME, S,TITLE,XTITLE,YTITLE

        KW = 13
        WRITE (*,770)
770     FORMAT( ' ENTER DATA FILE NAME: ',$)
        READ (*,780) NAME
780     FORMAT (A)
        OPEN (UNIT=12, FILE=NAME, STATUS='OLD')
        TYPE *,' READING INPUT FILE'
        READ (12,*) NV
        READ (12,5) S
        DO 102 I=1,NV
        READ  (12,*) X(I),XMAX(I),XMIN(I),DLMIN(I),DLTAX(I),MASK(I)
102     CONTINUE
        READ (12,*) ACK
        READ (12,*) COLIN
        READ (12,*) MATRIX
        READ (12,*) MAXR
        READ (12,*) MOSQU
        READ (12,*) NTRAC
        READ (12,*) RATIO
        READ (12,*) NTICKX, NTICKY
        READ (12,5) XTITLE
        READ (12,5) YTITLE
        READ (12,5) TITLE
        READ (12,*) X1,X2,Y1,Y2                 !GRAPH LIMITS
        READ (12,*) X3,X4,NFIT                  !CURVE LIMITS

        READ (12,*) NPTS
        READ (12,5) S
5       FORMAT (A)
        DO 101 I=1,NPTS
        READ (12,*) E(I),Y(I),DY(I)
C       write (*,*) E(I),Y(I),DY(I)
101     CONTINUE

C                                   END OF INPUT FILE
        DO 10 I = NV+1,20
                DLMIN(I) = 0.
                MASK(I) = 1.0
                X(I) = 0.
                XMAX(I) = 0.
                XMIN(I) = 0.
10      CONTINUE
        DO 103 I=1,NV
        XINITIAL(I) = X(I)
103     CONTINUE
        OPEN (UNIT=13, FILE='RESULT.OUT', STATUS='NEW',CARRIAGECONTROL='LIST')
        CALL FUNK
        TYPE *,' INITIAL CHISQ =',CHISQ
        CALL STEPT
        TYPE *
        TYPE *,'    INITIAL        FINAL'
        TYPE *,'    VALUES         VALUES'
        TYPE *
        DO 104 I=1,NV
        WRITE (*,21) XINITIAL(I),X(I)
        WRITE (13,*) I,'Xinitial= ',XINITIAL(I),'    Xfinal= ',X(I)
104     CONTINUE
21      FORMAT (F12.5,5X,F12.5)
        WRITE (*,30) NF
        WRITE (13,30) NF
30      FORMAT (' ', / I6,'    FUNCTION COMPUTATIONS' )
        WRITE (*,40) CHISQ
        WRITE (13,40) CHISQ
```

```
40      FORMAT (' FINAL  CHISQ =',E10.5)
        WRITE (13,*)
        WRITE (13,41)
41      FORMAT('            Energy       Y     EXP     Y     CALC
        1        '    Error%      Error*100')

        DO 100 I = 1,NPTS
        NERR = INT((Y(I)-FUNKY(I))*100)
        ERROR = 100.*(Y(I)-FUNKY(I))/Y(I)
        WRITE (13,90) I,E(I),Y(I),FUNKY(I),ERROR,NERR
90      FORMAT (' ',I7,5X,F8.3,5X,F9.2,5X,F9.3,5X,F9.2,5X,I8,4X,I8)
100     CONTINUE
        TYPE *,' The output is in "RESULT.OUT".'
        CALL ART(E,Y,DY,E,FUNKY,NPTS,NFIT,X1,X2,Y1,Y2,X3,X4,
        1       NTICKX,NTICKY,XTITLE,YTITLE,TITLE)
        CLOSE (12)
        CLOSE (13)

        END

        SUBROUTINE FUNK
        INCLUDE 'STEPTCOM.FOR'
        COMMON Y(500),E(500),DY(500),NPTS,FUNKY(500)
        COMMON NQ(500)

        CHISQ=0.

        DO 100 I=1,NPTS
        V = E(I)
        FUNKY(I) = FUNC(V)
        CHISQ = CHISQ +(FUNKY(I) - Y(I))*(FUNKY(I) - Y(I))/(DY(I))
100     CONTINUE
        CHISQ = CHISQ / (NPTS - NV)
        RETURN
        END

        FUNCTION FUNC(V)
        INCLUDE 'STEPTCOM.FOR'
*       FUNC = X(1)*EXP(-X(2)*V)
        FUNC = X(1)*V+X(2)
        RETURN
        END



        SUBROUTINE ART(XPOINT,YPOINT,YERR,XFIT,YFIT,NPOINT,NFIT,
        1       X1,X2,Y1,Y2,X3,X4,
        1       NTICKX,NTICKY,XTITLE,YTITLE,TITLE)
        DIMENSION XPOINT(200),YPOINT(200),YERR(200),XFIT(200),YFIT(200)
        CHARACTER*60 TITLE,XTITLE,YTITLE

        OPEN (UNIT=15, FILE = 'ART.DAT', STATUS = 'NEW',CARRIAGECONTROL='LIST')
        WRITE (15,100) '25      18      .1      .02'
100     FORMAT (A)
        WRITE (15,100)
        WRITE (15,100) 'BOX'
        WRITE (15,100) '4.99    3.99    18      12'
        WRITE (15,100)  ' '
        WRITE (15,100)  'XAXIS'
        WRITE (15,110)  '5.     4.      18      ',NTICKX,'      0.      .2'
        WRITE (15,100)  ' '
        WRITE (15,100)  'XAXIS'
        WRITE (15,110)  '5.     16.     18      ',NTICKX,'      .2      0.'
        WRITE (15,100)  ' '
        WRITE (15,100)  'YAXIS'
        WRITE (15,110)  '5.     4.      12      ',NTICKY,'      0.      .2'
        WRITE (15,100)  ' '
        WRITE (15,100)  'YAXIS'
        WRITE (15,110)  '23.    4.      12      ',NTICKY,'      .2      0.'
        WRITE (15,100)  ' '
110     FORMAT (A,I5,A)
```

```

        DX = (X2 - X1)/NTICKX
        FX = 5.
        D = 18./NTICKX
        DO 300 I=0,NTICKX
        WRITE (15,100)  'PW'
        WRITE (15,150)  FX,'    3       .3      0       0'
150     FORMAT (F7.3,A)
        FX = FX + D
        XLABLE = X1 + I * DX
        WRITE (15,200)  XLABLE
200     FORMAT (F7.1)
        WRITE (15,100)  ' '
300     CONTINUE

        DY = (Y2 - Y1)/NTICKY
        FY = 4.
        D = 12./NTICKY
        DO 400 I=0,NTICKY
        WRITE (15,100)  'PW'
        WRITE (15,350)  '4      ',FY,'  .3      0       0'
350     FORMAT (A,F7.3,A)
        FY = FY + D
        YLABLE = Y1 + I * DY
        WRITE (15,202)  YLABLE
202     FORMAT (F7.3)
        WRITE (15,100)  ' '
400     CONTINUE

        WRITE (15,100)  'PW'
        WRITE (15,100)  '14     2       .3      0       0'
        WRITE (15,100)  XTITLE
        WRITE (15,100)  ' '
        WRITE (15,100)  'PW'
        WRITE (15,100)  '2      10      .3      0       90'
        WRITE (15,100)  YTITLE
        WRITE (15,100)  ' '
        WRITE (15,100)  'PW'
        WRITE (15,100)  '14     17      .3      0       0'
        WRITE (15,100)  TITLE
        WRITE (15,100)  ' '

        WRITE (15,100)  'PPLOT'
        WRITE (15,100)  '5      4       18      12      .3      0       0'
        WRITE (15,500)  X1,X2,Y1,Y2
500     FORMAT(4F12.4)
        WRITE (15,100)  ''GKT1'/'RPT1''
        WRITE (15,600)  NPOINT
600     FORMAT (2I10)
        DO 800 I=1,NPOINT
        WRITE (15,700)  XPOINT(I),YPOINT(I),YERR(I)
700     FORMAT(3F12.4,'     0     0')
800     CONTINUE
        WRITE (15,100)  ' '

        WRITE (15,100)  'CURVE'
        WRITE (15,100)  '5      4       18      12'
        WRITE (15,500) X1,X2,Y1,Y2
        WRITE (15,600)  NFIT,NFIT
        DV = (X4 - X3)/(NFIT-1)
        V = X3
        DO 1000 I=1,NFIT
        WRITE (15,900) V,FUNC(V)
        V = V + DV
900     FORMAT (2F12.4)
1000    CONTINUE
        WRITE (15,100)

        CLOSE (15)
        RETURN
        END

```

☆ U.S. GOVERNMENT PRINTING OFFICE 1992 — 648-127 62607